Axisymmetric MHD Modes in Twisted Magnetic Fields

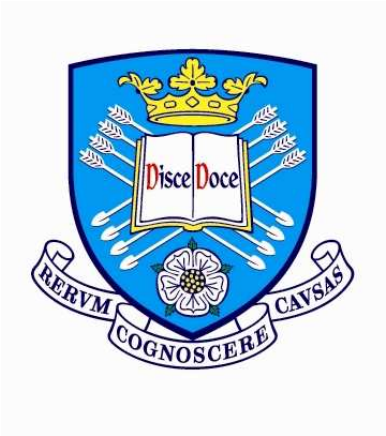

Ioannis Giagkiozis

School of Mathematics and Statistics

The University of Sheffield

A dissertation submitted in partial fulfilment of the requirements for the degree of

Doctor of Philosophy in Applied Mathematics

September 2017

Executive Summary

Vortex flows in the solar atmosphere may contribute significantly to the energy flux requirements for heating the quiet Sun atmosphere. This thesis presents evidence that the expected number of vortices in the solar photosphere is significantly larger than estimated and most importantly their lifetime is, in the mean, much shorter than previously believed. This suggests that vortex flows are highly dynamic and that their formation and dissolution is highly temporally localised. The measurements and statistics that support this evidence were made possible by use of an automated vortex identification approach which allowed for a much larger sample. In fact the number of identified vortices is several orders of magnitude larger compared with the latest research on the subject.

Given that vortices in the solar photosphere can introduce magnetic twist, a pertinent question then is: "How would that magnetic twist affect axisymmetric MHD modes?". Part of this thesis visits this question and the theoretical models used offer interesting answers. Firstly, even for weak magnetic twist the long wavelength cut-off for the sausage mode that is present in models without magnetic twist, is removed! It is shown that magnetic twist naturally couples axisymmetric Alfvén waves with sausage waves. A coupling that results, among other things, in sausage waves exhibiting Doppler signatures similar to these expected to be observed in Alfvén waves. These modes can also be excited by a larger variety of drivers compared to the *pure* sausage and axisymmetric Alfvén waves. Something that makes them more pertinent to the question of energy propagation than their *pure* cousins (sausage and Alfvén waves).

Lastly, a calculation is presented, for the first time, of a dispersion relation for resonantly damped axisymmetric modes, in the spectrum of the Alfvén continuum and also an approximation is presented of the damping time in the long wavelength limit. It is shown that the damping times can be comparable to that observed for the kink mode in the case that there is no magnetic twist.

Acknowledgements

I would like to thank my supervisor Gary Verth for the vigorous, and at times passionate, discussions on physics and mathematics. I would also like to thank Viktor Fedun for consistently offering a different perspective on things and Eamon Scullion for sharing his expertise on observations and providing me with the necessary data for part of this work (Chapter 3). My appreciation and thanks is also due to Tom Van Doorsselaere for inviting and supporting my visits to the Mathematics department in KU Leuven. Visits which I shall truly cherish as they afforded me the opportunity to collaborate with Tom and Marcel Goossens whose fervour for mathematical physics has not been dampened in the least by his long career in investigating resonant damping. I would like to extend my gratitude to my examiners Youra Taroyan and Istvan Ballai for their meticulous comments on this work. I am indebted to the Faculty of Science of the University of Sheffield for funding this work via the SHINE studentship. Lastly my thanks and love to my wife Meg, for her never ending support during the preparation of this thesis, the previous one and the one before!

This thesis has been written in LaTeX2e, a free document preparation system (see `www.latex-project.org`).

Statement of Originality

Unless otherwise stated in the text, the work described in this thesis was carried out solely by the candidate. None of this work has already been accepted for any other degree, nor is it being concurrently submitted in candidature for any degree.

Candidate: _____

Ioannis Giagkiozis

Supervisor: _____

Gary Verth

Contents

List of Figures

List of Tables

Chapter 1

Introduction

1.1 The Sun

The Sun is about 5 billion years old and it will remain in its present phase of evolution for approximately another 5 billion years. Then, its core hydrogen will be exhausted, our Sun will expand significantly and will be transformed into a red giant. This red giant will eventually collapse to a white dwarf whose size will be comparable to today's Earth size.

The Sun has been studied for thousands of years. Mankind's fascination with the *bright object* in the sky is arguably as long as history. Perhaps people always understood, even on an intuitive level, that their lives where intricately linked with this magnificent object. The first recorded study of the Sun dates as far back as 2000 BC by the Chinese and 600 BC by the Greeks. Notably, in 280 BC Aristarchus of Samos suggested correctly that the Earth is travelling around the Sun. He even estimated the Earth-Sun distance to 8 million kilometres. Although this estimate was off by a factor of approximately 20 it is by no means a small feat, especially when we consider that it took more than 2 millennia to get the correct estimate of 149.6 million kilometres by Euler in 1770. Unfortunately Aristarchus' theory was supplanted by Ptolemy who argued for an Earth-centric Universe[1], a theory that was not challenged for 1400 years! We have come a long way in our understanding of the Universe and our nearest star since the Chinese first recorded solar eclipses, however, we should not rest on our laurels as it was *only* 200 years ago that we thought that the Sun's surface was actually inhabited (Priest, 2014, pp. 2)!

[1] Note that for the purposes of this thesis, it is assumed that there is one unique universe, our own. Hence it will be referred to as *the Universe*.

1.1.1 Characteristics of the Sun

The most commonly accepted distinction of solar phenomena separates regions on the surface of the Sun labelling them as quiet and active. The quiet Sun regions are, in relative terms, less dynamic and have a weaker magnetic field that is almost negligible in comparison to active regions. The active regions of the Sun are more dynamic thus supporting a greater number of transient phenomena. The transient phenomena in active regions range from sunspots, prominences, flares and coronal mass ejections. The primary drivers of these phenomena are strong magnetic fields; up to approximately two orders of magnitude compared to the quiet sun regions. A large body of recent research suggests that this distinction in quiet and active regions is perhaps too simplistic and although there are indeed differences there exists significant evidence to suggest that the quiet Sun regions may not be as *quiet* as we thought in the past; a multi-scale view would be more appropriate (e.g. (Hansteen et al., 2005; Hansteen et al., 2014; McIntosh et al., 2011; Klimchuk, 2015) and Chapter 1 by (Priest, 2014)). The quiet atmosphere is influenced significantly by the magnetic field, which is influenced by the granule cells whose nature is highly dynamic (see Chapter 5). Additionally, the idea that the Sun's atmosphere is static and that adheres to spherical symmetry is in stark contradiction with what is observed.

For a well rounded account of Sun's properties and the associated physical processes see, e.g. Stix (2012) which is an excellent introduction. Other textbooks on the subject are: Priest (2014) with a clear focus on magnetic reconnection, and of course Aschwanden (2005) is also an invaluable reference with a focus on the corona.

Most of our information about distant stars comes from spectroscopy and the photospheric light that reaches us from these stars. The spectral signatures of this light are determined by the temperature (T in degrees Kelvin K) and the relative abundance of chemical elements in the star. Another important measure in the classification of stars, that quantifies their relative brightness, is the apparent magnitude, m:

$$m \equiv m_0 - 2.5 \cdot \log\left(\frac{l}{l_0}\right), \tag{1.1}$$

where, l is the flux, that is the amount of electromagnetic radiation energy passing per unit time through a unit area. Here, l_0 and m_0 refer to the flux and apparent magnitude of a reference star and are fixed by convention.

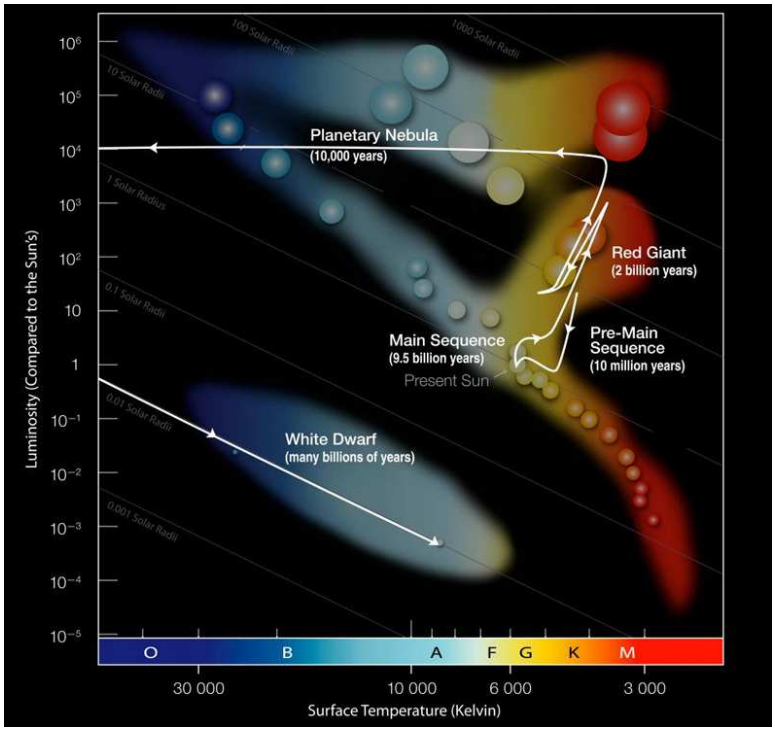

Figure 1.1: Hertzsprung-Russell diagram. Credit: Chandra X-Ray observatory, diagram downloaded from `http://chandra.harvard.edu/edu/formal/variable_stars/bg_info.html`.

The problem with Equation (1.1) is that two stars that have the same apparent magnitude may, and indeed chances are they will, have different luminosity, L, which is the total radiative energy output per unit time of the star. Now, given that the flux, l, depends both on the distance, d, from the star and its luminosity as

$$l = \frac{L}{4\pi d^2}, \tag{1.2}$$

it becomes evident that the apparent magnitude does not uniquely characterise a star.

To overcome this indeterminacy the absolute magnitude, M, is used. The absolute magnitude is calculated using the expected flux $\hat{l}$ that would be observed if the star in question was at a distance $\hat{d} = 10\text{pc}$ (parsec $1\text{pc} = 3.09 \cdot 10^{16}\text{m}$) from Earth. Therefore, with the help of Equation (1.1) and Equation (1.2) the expression for the absolute magnitude is:

$$M \equiv m_0 - 2.5 \cdot \log\left(\frac{\hat{l}}{l_0}\right). \tag{1.3}$$

Given this definition the absolute magnitude of the Sun is 4.7.

A systematic way to represent the pair (T, M) for stars is the Hertzsprung-Russell diagram that plots the absolute magnitude, M, versus the effective surface temperature T, see Figure 1.1. From this diagram we can see that our Sun is of just an ordinary main sequence star. Notwithstanding this fact, our Sun holds the key to furthering our understanding of other stars and plasma physics in general. Some of the physical properties of the Sun can be seen in Table 1.1.

The magnitude of the numbers in Table 1.1 is quite removed from our daily experience and so a comparison with more familiar measures can aid comprehension. According to the *International Energy Association* the world energy production in 2015 was approximately $1.6 \cdot 10^{17}$W h. If we could capture Sun's Luminosity for only a second, that would provide sufficient energy to power our civilisation for more than $274,000$ years at the present rate of consumption. Furthermore, Earth's mass and radius are approximately $6 \cdot 10^{24}$kg and $6 \cdot 10^{6}$km respectively. This means that the Sun's mass is $330,000$ times larger than the Earth's mass and its radius is 109 times larger. The mean Sun-Earth distance is $149.6 \cdot 10^{9}$m (1 astronomical unit AU); a distance that light covers in about $8'20''$.

1.2 Solar Anatomy

1.2.1 Interior

Our Sun is in essence a large ball of plasma. It is mainly composed of ionised hydrogen H ($\approx$ 92 per cent) and helium He ($\approx$ 8 per cent). Other elements that account for approximately 0.1 per cent are carbon C, nitrogen N and oxygen O and their proportions are similar with those found on Earth, which would suggest a common origin. The

Property	Value
Age	$4.6 \cdot 10^{9}$yr
Mass	$1.99 \cdot 10^{30}$kg
Radius	$6.955 \cdot 10^{8}$m
Mean density	$1.4 \cdot 10^{3}$kg m^{-3}
Mean distance from Earth	$1.496 \cdot 10^{11}$m
Surface gravity	274m s^{-2}
Luminosity (L)	$3.86 \cdot 10^{26}$W
Effective temperature	5785K

Table 1.1: Physical properties of the Sun.

internal structure of the Sun in not visible however the field of helioseismology, mainly with the help of waves, has been used to estimate the properties of the solar interior, see Figure 1.2. The interior is primarily divided into three regions: i) solar core, ii) radiative zone and, iii) the convection zone, with a thin separation layer between the radiative zone and the convection zone, the tachocline.

1.2.2 Solar Core

The solar core is a nuclear reactor that consumes $5 \cdot 10^9$kg of hydrogen per second converting it to helium primarily via the proton-proton cycle. It is estimated that its temperature is about 15 million degrees Kelvin, has a mass density of $1.5 \cdot 10^5 \mathrm{kg\,m^{-3}}$ and its radius is approximately 0.25 solar radii. The solar core is responsible for 99% of the Sun's energy generation.

1.2.3 Radiative Zone

Beyond the core and within $[0.25, 0.713]$ solar radii is the radiative zone. This zone is in approximate radiative equilibrium as the main energy flux transport mechanism is radiation via photon emission, absorption and re-emission. The standard model for the solar interior assumes that the pressure, p, temperature, T, and density, ρ, are functions only of the radial distance from the centre. An additional assumption is that spherical shells at a given radius, r, are in hydrostatic and thermal equilibrium. With these assumptions using the perfect gas law and the diffusion approximation for radiative flux

$$F \equiv \frac{L}{4\pi r^2}, \tag{1.4}$$

we obtain the temperature gradient:

$$\frac{dT}{dr} = -\frac{3\kappa_R \rho}{16\sigma_{SB} T^3} \frac{L}{4\pi r^2}, \tag{1.5}$$

here κ_R is the Rosseland mean opacity, σ_{SB} the Stefan-Boltzmann constant and L the luminosity.

1.2.4 Convection Zone

Moving away from the radiative zone the mean opacity κ_R rises quickly which in turn increases the temperature gradient and at approximately 0.7 solar radii the convective instability appears. Plasma rises and expands in its journey toward the photosphere

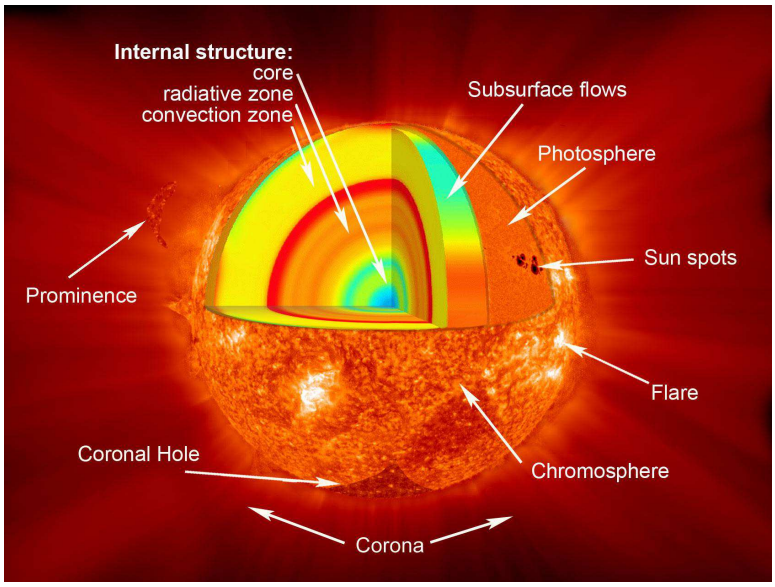

Figure 1.2: Solar anatomy. Credit: NASA/Goddard, diagram downloaded from `https://www.nasa.gov/mission_pages/sunearth/science/Sunlayers.html`

until the point where its opacity is sufficiently low to radiate energy away; cooling down and then descending. This process of the convection zone is manifested in the photosphere by granulation, see Figure 1.3.

1.2.5 Atmosphere

The solar atmosphere is the part of the Sun that we can *see*. This is defined by the optical thickness τ:

$$I = I_0 e^{-\tau} \tag{1.6}$$

where I_0 is the radiation intensity at the source and I is the observed intensity. A medium is optically *thick* (or opaque) when $\tau \geq 1$, that is when the initial radiation intensity I_0 drops off by more than a factor of e until it reaches its destination I.

The atmosphere is divided into three regions: i) photosphere, ii) chromosphere and, iii) corona. The photosphere is relatively dense, opaque and is the source of the majority of Sun's radiation; hence its name ($\phi\omega\varsigma$ means light in Greek). The photosphere's optical thickness is below unity in part of the ultraviolet, visible and part of the infrared light.

Above the photosphere is the chromosphere which is tenuous and optically thin, which is followed by the corona that is separated from the chromosphere by a thin layer called the transition region. The temperature levels along with the density in

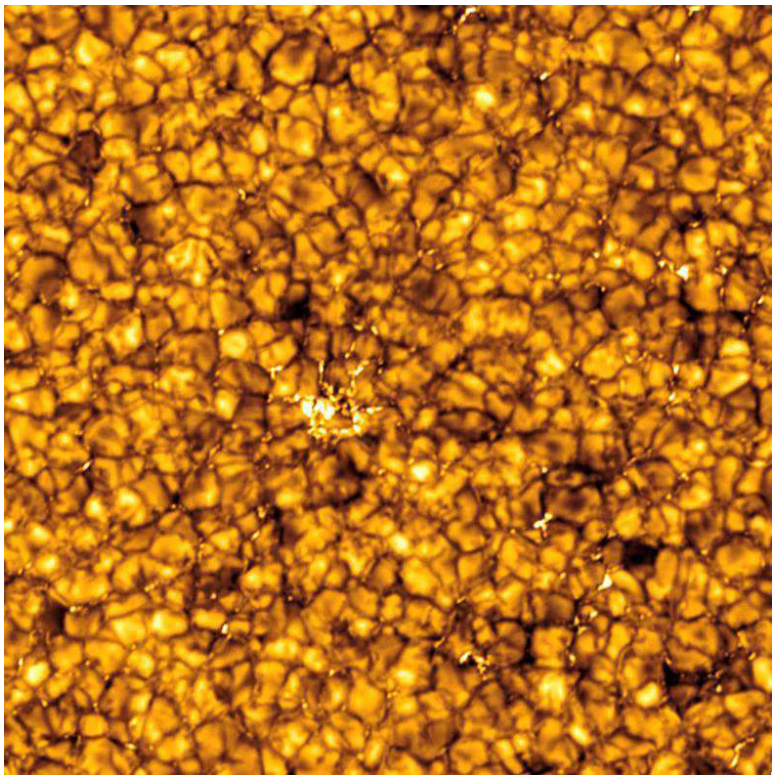

Figure 1.3: Granulation on the photosphere.

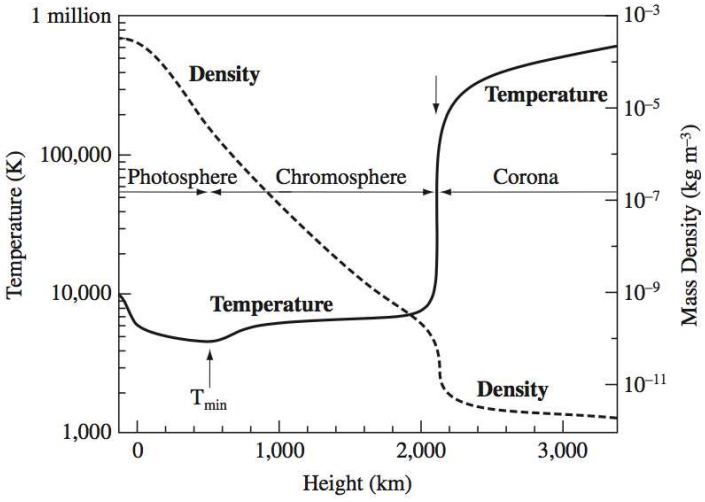

Figure 1.4: Mean variation of temperature and density as a function of height in the solar atmosphere according the the VAL model (Vernazza et al., 1981).

each of these regions according to the VAL model by (Vernazza et al., 1981) can be seen in Figure 1.4. The VAL model is a one-dimensional model that correctly fits a number of spectral lines in different regions of the atmosphere. Despite its simplicity, it has proven to be very useful.

1.2.6 Photosphere

The photosphere is dominated by granulation. Granules have irregular highly dynamic shapes and they form and disappear constantly. Their centre is bright since it is comprised of hot plasma that *bubbles* upward and out, much like a fountain. As the plasma cools, it falls down at the boundaries of granules, the intergranular lanes. This explains why these appear darker in images, see Figure 1.3. Granule sizes vary approximately in the range $[0.3, 2.0]$Mm; have a typical size of about 1Mm and their lifetime is in the range of 1 to 20 minutes. There is a correlation between granule size and their lifetime with larger granules tending to have longer lifetimes along with smaller horizontal plasma flow velocities. Granules are formed by two or more other granules or the fragmentation of a large granule.

Apart from these granulation patterns that are considered to be *small* scale, there are mesogranules (Shine et al., 2000) and supergranules (Hagenaar et al., 1997). Supergranules have a mean size of about 30Mm with typical sizes within the $[20, 70]$Mm range (Roudier and Muller, 1986). Mesogranules bridge the scale gap between granules and supergranules and have lifetimes between 3 to 6 hours.

Photospheric vortices are often present in magneto-convection simulations (Nordlund et al., 2009). Similar structures have been discovered by Steiner et al. (2010); Bonet et al. (2010, 2008) and others. These typically have lifetimes between 5 to 10 minutes. In Chapter 5 of this thesis is is shown that there is another type of vortices on the solar photosphere that have significantly smaller lifetimes and are ubiquitous.

The magnetic field on the photosphere is highly variable and dependent on location. In active regions the mean flux density is approximately within 100G to 500G.

1.3 Thesis Outline

The focus of this thesis is the study of axisymmetric MHD modes in the presence of magnetic twist in solar atmospheric conditions. Vortex flows in the photosphere can

excite these MHD modes and, as such, the statistical properties of these flows are an important factor in estimating whether the conditions for the excitation of these modes are commonly met in the photosphere.

The two main threads of research explored in this thesis are, i) the identification and statistical analysis of vortex flows in the solar atmosphere and ii) the mathematical analysis of axisymmetric MHD modes as well as their resonant absorption.

Chapter 2 lays the theoretical foundation for the following chapters. The linearised ideal MHD equations are presented along with the analytical tools used for the study of wave modes in a uniform unbounded magnetized plasma. This fundamental case is then contrasted with the wave modes in a magnetic flux tube.

Chapter 3 presents an analytical study of axisymmetric modes in magnetically twisted flux tubes using a set of physically plausible assumptions and simplifications to proceed with the analysis. A dispersion equation is derived which is subsequently solved numerically to study various tube configurations, e.g. warm dense tube, weak cool tube and others. One of the interesting findings of this work is that axisymmetric modes in magnetically twisted flux tubes can readily be confused with pure Alfvén waves and given the prevalence of magnetic twist in the solar photosphere it is possible that reports of Alfvén wave observations may in fact be of axisymmetric modes.

Chapter 4 is a study of resonant absorption in axisymmetric modes using the conservation laws developed by Sakurai et al. (1991a). A dispersion relation is derived in the Alfvén continuum and a simplified approximation is presented. Using these relations, a probabilistic study is conducted with the aim to aid observers identify regions that are likely to be viable conduits of axisymmetric waves based on a set of parameters. The theoretical predictions of the damping times calculated in this chapter are in good agreement with observed damping times reported by Van Doorsselaere et al. (2011) and Morton et al. (2012) and also quasi-periodic pulsations (Kolotkov et al., 2015) that are believed to be fast sausage waves.

Chapter 5 presents a study on the automated identification of photospheric intensity vortices using observations from the Swedish 1-m Solar Telescope (SST) on La Palma. After an introduction, the method used in the identification process is elaborated and subsequently a statistical analysis of the properties of these vortices, such as lifetime, radius, expected number of vertices, expected area and their proportion to the total

area of the photosphere is presented. Lastly, the potential implications of these results are elaborated upon.

In Chapter 6 future research, interesting new open avenues of research inquiry and insight gained from this work are presented. The main results and conclusions of this work are summarised and the thesis concluded.

1.4 Contributions

The main contributions of this work are:

- *Vortex Flows in the Solar Atmosphere: Automated Identification and Statistical Analysis*, submitted currently in review. Chapter 5 of this thesis is based on this work.

- *Resonant Absorption of Axisymmetric Modes in Twisted Magnetic Flux Tubes* (Giagkiozis et al., 2016) published in The Astrophysical Journal. Chapter 4 is based on this publication.

- *Axisymmetric Modes in Magnetic Flux Tubes with Internal and External Magnetic Twist* Giagkiozis et al. (2015) published in The Astrophysical Journal. Chapter 3 is based on this publication.

- *Multiwavelength Studies of MHD Waves in the Solar Chromosphere* Jess et al. (2015) publised in Space Science Reviews. The author's contribution to this work is section 3 and several figures that appear in this survey publication. Chapter 2 in this thesis is based on the aforementioned section of this paper.

- *Wave Damping Observed in Upwardly Propagating Sausage-Mode Oscillations Contained Within a Magnetic Pore* Grant et al. (2015) published in The Astrophysical Journal. The author's contribution to this work was the solution of dispersion equations and discussion of the findings. No text from this publication appears in this thesis.

Chapter 2

Theoretical Foundations

2.1 Introduction to MHD Waves

2.1.1 Linearised Ideal MHD

In the absence of a magnetic field in a plasma, the supported eigenmodes are sound waves which are isotropic, that is, their speed is independent on the direction of propagation and also these waves are non-dispersive. However, in the presence of a magnetic field the number of supported waves is increased. Importantly, although some of these waves have similarities with sound waves, they can be highly anisotropic. This is because their character depends on the degree of alignment of the wavevector ($\boldsymbol{k}$) with the direction of the background magnetic field ($\boldsymbol{B}$) and the ratio of the kinetic pressure (p) versus the magnetic pressure ($\boldsymbol{B}^2/2\mu_0$). This ratio is the plasma-β, defined as $\beta = 2\mu_0 p/\boldsymbol{B}^2$, where μ_0 is the magnetic permeability of free space. A commonly used method to explore the properties of waves in magnetised plasmas is to consider the linearised ideal MHD equations. As a first step let us consider small perturbations about a static equilibrium, i.e. no background flow, $\boldsymbol{v}_0 = \boldsymbol{0}$

$$\frac{\partial}{\partial t}\rho' = -\nabla \cdot (\rho \boldsymbol{v}'), \tag{2.1a}$$

$$\rho_0 \frac{\partial}{\partial t}\boldsymbol{v}' = -\nabla p' + \frac{1}{\mu_0}\left[(\nabla \times \boldsymbol{B}) \times \boldsymbol{B}' + (\nabla \times \boldsymbol{B}') \times \boldsymbol{B}\right], \tag{2.1b}$$

$$\frac{\partial p'}{\partial t} = v_S^2 \frac{\partial \rho'}{\partial t}, \tag{2.1c}$$

$$\frac{\partial}{\partial t}\boldsymbol{B}' = \nabla \times (\boldsymbol{v}' \times \boldsymbol{B}), \tag{2.1d}$$

where ρ, p and $\boldsymbol{B}$ are the density, kinetic pressure and magnetic field at equilibrium and are all functions of spatial coordinates ($\boldsymbol{x}$). Furthermore, ρ', p' and $\boldsymbol{B}'$ are the cor-

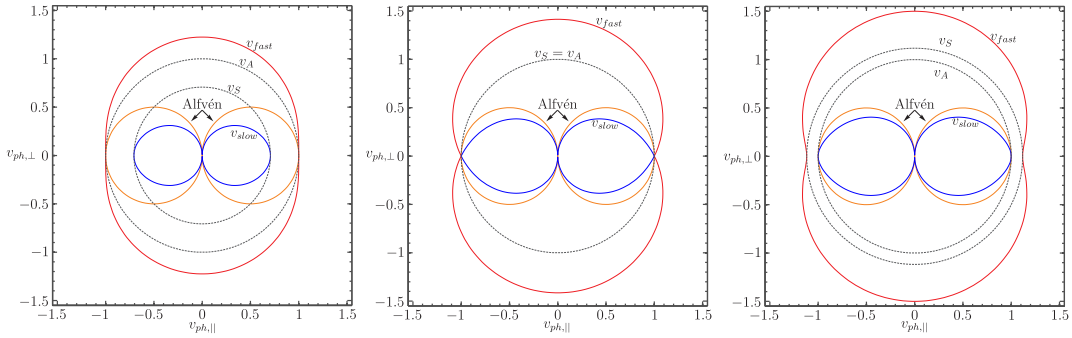

Figure 2.1: Friedrichs diagrams for $v_S < v_A$ with $\beta = 1/\gamma$ (left), $v_S = v_A$ and $\beta = 2/\gamma$ (middle) and $v_S > v_A$ with $\beta = 2.5/\gamma$ (right). The phase speed perturbation of the slow magneto-acoustic wave is illustrated in blue, the Alfvén wave in orange and the fast magneto-acoustic wave in red. The dotted lines correspond to the sound and Alfvén speed. The horizontal and vertical axes labelled as $v_{ph,||}$ and $v_{ph,\perp}$ respectively represent the velocity perturbation components along and perpendicular to the equilibrium magnetic field, $\boldsymbol{B}$.

responding perturbed quantities, while $\boldsymbol{v}'$, is the velocity perturbation. The quantity, v_S is the adiabatic sound speed.

2.1.2 Wave Modes in a Uniform Unbounded Magnetized Plasma

Now let us explore Equation (2.1) in a very simple setting illustrating the wave modes, that are supported in the MHD description of plasmas, and their identifying characteristics. For an unbounded homogeneous magnetized plasma, namely p, ρ and $\boldsymbol{B}$ are constant, Equation (2.1) can be rewritten (Priest, 2014) as,

$$\frac{\partial}{\partial t}\rho' = -\rho\nabla\cdot(\boldsymbol{v}'), \tag{2.2a}$$

$$\rho_0\frac{\partial}{\partial t}\boldsymbol{v}' = -\nabla\left(p' + \frac{\boldsymbol{B}\cdot\boldsymbol{B}'}{\mu_0}\right) + \frac{1}{\mu_0}\nabla\cdot\left(\boldsymbol{B}\boldsymbol{B}'\right), \tag{2.2b}$$

$$\frac{\partial p'}{\partial t} = v_S^2\frac{\partial \rho'}{\partial t}, \tag{2.2c}$$

$$\frac{\partial}{\partial t}\boldsymbol{B}' = (\boldsymbol{B}\cdot\nabla)\boldsymbol{v}' - \boldsymbol{B}(\nabla\cdot\boldsymbol{v}'), \tag{2.2d}$$

the two terms in the right hand side of the momentum Equation (2.2b) are the total pressure perturbation,

$$p'_T = p' + \boldsymbol{B}\cdot\boldsymbol{B}'/\mu_0, \tag{2.3}$$

comprised of the perturbation of the kinetic pressure, p', and the magnetic pressure perturbation, $\boldsymbol{B}\cdot\boldsymbol{B}'/\mu_0$. The second term in right hand side of Equation (2.2b) is the

magnetic tension. Let us consider plane wave solutions for the perturbed quantities,

$$\boldsymbol{v}', \boldsymbol{B}', p', \rho' \propto e^{i(\boldsymbol{k}\cdot\boldsymbol{x}-\omega t)}, \tag{2.4}$$

where $\boldsymbol{x}$ is the position vector and $\boldsymbol{k}$ is the wavevector. The equations in the system (2.2) can be combined to produce the dispersion relation. Specifically, there are two possibilities, (i) $\boldsymbol{k}\cdot\boldsymbol{v}' = 0$ which corresponds to the incompressible case, and, (ii) $\boldsymbol{k}\cdot\boldsymbol{v}' \neq 0$ that corresponds to the compressible case. Using the system (2.2) for the case $\boldsymbol{k}\cdot\boldsymbol{v}' = 0$ results in the following dispersion relation in terms of the phase speed $v_{ph} = \omega/k$ (where $k = |\boldsymbol{k}|$)

$$v_{ph}^2 = \frac{\boldsymbol{B}^2}{\mu_0\rho}\cos^2\theta \tag{2.5}$$

$$= v_A^2\cos^2\theta, \tag{2.6}$$

where θ is the angle between the wavevector, $\boldsymbol{k}$, and the background magnetic field, $\boldsymbol{B}$. Equation (2.5) describes an anisotropic, non-dispersive wave whose only restoring force is the magnetic tension. The phase speed in Equation (2.5) corresponds to phase speed of the Alfvén wave (Alfvén, 1942), where $v_A = |\boldsymbol{B}|/\sqrt{\mu_0\rho}$. In the compressible case ($\boldsymbol{k}\cdot\boldsymbol{v}' \neq 0$) the system of equations (Equations 2.2) can be combined producing the following dispersion equation,

$$v_{ph}^4 - (v_S^2 + v_A^2)v_{ph}^2 + v_S^2 v_A^2\cos^2\theta = 0, \tag{2.7}$$

Equation (2.7) has two roots in terms of the square of the phase speed, i.e.

$$v_{ph}^2 = \frac{1}{2}\left(v_S^2 + v_A^2\right) + \frac{1}{2}\left(v_S^4 + v_A^4 - 2v_S^2 v_A^2\cos 2\theta\right)^{1/2}, \tag{2.8a}$$

$$v_{ph}^2 = \frac{1}{2}\left(v_S^2 + v_A^2\right) - \frac{1}{2}\left(v_S^4 + v_A^4 - 2v_S^2 v_A^2\cos 2\theta\right)^{1/2}. \tag{2.8b}$$

The solutions in Equation (2.8) correspond to the two magneto-acoustic modes: the slow mode, has a phase speed given by Equation (2.8b), and the fast mode, whose phase speed is given by Equation (2.8a). In summary, there are three MHD modes, the Alfvén mode (Equation 2.5) whose restoring force is only magnetic tension and the two magneto-acoustic modes whose restoring force is a combination of magnetic tension and total pressure force. The phase speed in Equation (2.7) depends on the angle, θ, and the ratio of the sound speed versus the Alfvén speed, which is proportional to the plasma-β, i.e. $\beta = (2/\gamma)v_S^2/v_A^2$. First let us explore the two extremes for the plasma

β, namely $\beta \gg 1$ and $\beta \ll 1$. Note the $\beta \gg 1$ limit means that $v_S \gg v_A$ and similarly, $\beta \ll 1$ is equivalent to $v_A \gg v_S$. In the limit where $\beta \gg 1$, Equation (2.8) is reduced to

$$v_{ph}^2 \sim \begin{cases} v_S^2 & \text{for } \textit{Equation } (2.8a), \\ v_A^2 \cos^2\theta & \text{for } \textit{Equation } (2.8b), \end{cases} \tag{2.9}$$

where the solution corresponding to Equation (2.8a) is the dominant mode and the solution corresponding to Equation (2.8b) is a second order correction. This means that for $\beta \gg 1$, the Alfvén and slow modes vanish and the fast mode, now the only mode, converges to the sound speed. This result is quite intuitive considering that a high plasma-β, in the $\beta \gg 1$ limit, the kinetic pressure dominates the magnetic pressure thus the magnetic pressure and tension in Equation (2.2b) can be neglected, reducing Equation (2.2b) to the linearised Navier-Stokes equation. For the low plasma-β case (i.e. $\beta \ll 1$), Equation (2.8) reduces to

$$v_{ph}^2 \sim \begin{cases} v_A^2 & \text{for } \textit{Equation } (2.8a), \\ v_S^2 \cos^2\theta & \text{for } \textit{Equation } (2.8b), \end{cases} \tag{2.10}$$

which means that the fast magneto-acoustic wave in this case converges in magnitude to the Alfvén speed and is isotropic. Additionally, it is interesting to note that the fast magneto-acoustic mode is very weakly dependent on kinetic pressure and the main restoring forces are the magnetic pressure gradient and magnetic tension. Furthermore, for a wavevector $\boldsymbol{k}$ parallel to $\boldsymbol{B}$ the restoring force of the fast magneto-acoustic mode is solely the magnetic tension while for increasing θ the magnetic pressure gradient becomes increasingly more important until $\theta = \pi/2$ where the restoring force is only the magnetic pressure gradient. In contrast, the slow magneto-acoustic mode is highly dependent on θ and admits no waves for $\theta = \pi/2$.

Next, the cases $\boldsymbol{k} \parallel \boldsymbol{B}$ and $\boldsymbol{k} \perp \boldsymbol{B}$ are considered. The first case naturally corresponds the $\theta = 0$, and so Equation (2.8) is reduced to

$$v_{ph}^2 \sim \begin{cases} v_A^2 & \text{for } \textit{Equation } (2.8a), \\ v_S^2 & \text{for } \textit{Equation } (2.8b), \end{cases} \tag{2.11}$$

while for $\boldsymbol{k} \perp \boldsymbol{B}$ ($\theta = \pi/2$), (2.8) reduces to

$$v_{ph}^2 \sim \begin{cases} v_A^2 + v_S^2 & \text{for } \textit{Equation } (2.8a), \\ 0 & \text{for } \textit{Equation } (2.8b). \end{cases} \tag{2.12}$$

The first observation in this case is that the fast magneto-acoustic mode is no longer isotropic since its phase speed varies from v_A to $\sqrt{v_A^2 + v_S^2}$. Note that in the limit

$v_A \gg v_S$, the phase speed of the fast mode becomes $v_{ph} \sim v_A$, which is in agreement with Equation (2.10). In this case the fast mode can be considered to be approximately isotropic.

An interesting relation between the slow and fast magneto-acoustic modes is revealed when Equation (2.1), Equation (2.2c) and Equation (2.1d) are combined, obtaining the following relation between magnetic pressure and kinetic pressure,

$$\frac{1}{\mu_0}\boldsymbol{B}\cdot\boldsymbol{B}' = \frac{v_A^2}{v_S^2}\left(1 - \frac{v_S^2}{v_{ph}^2}\cos^2\theta\right)p'. \tag{2.13}$$

According to Equation (2.13), when $v_{ph} < v_S\cos\theta$ the kinetic and magnetic pressure are out of phase by π and so these restoring forces oppose each other. From Equation (2.8b) it follows immediately that this condition holds for slow magneto-acoustic waves, this is clearly illustrated in Figure 2.1.

In the case where $v_{ph} > v_S\cos\theta$, the magnetic and kinetic pressure perturbations are in phase and thus support each other. This condition holds for the fast magneto-acoustic wave, see Equation (2.8a) and Figure 2.1. In the case when $v_{ph} = v_S\cos\theta$, the magnetic pressure is zero. Apart from the trivial solution, this condition is satisfied when, i) $v_A > v_S$, for $\theta = 0, \pi$ corresponding to the slow magneto-acoustic wave at this points, ii) $v_A = v_S$, and is satisfied by the the Alfvén wave and lastly, iii) $v_S > v_A$, which is satisfied by the fast magneto-acoustic wave at $\theta = 0, \pi$. We also notice that for $v_A \gg v_S$ magnetic pressure is dominant while for $v_S \gg v_A$ the opposite is true.

In summary, in ideal linearised MHD for a homogeneous plasma there are three distinct waves, i.e. the slow and fast magneto-acoustic and the Alfvén waves. The phase speeds of these waves are well ordered: $0 \leq v_{slow} \leq v_A \leq v_{fast}$ and also their velocities are mutually perpendicular, $\boldsymbol{v}_{slow} \perp \boldsymbol{v}_A \perp \boldsymbol{v}_{fast}$ (Goedbloed and Poedts, 2004). The Alfvén mode is incompressible and is supported purely by the magnetic tension, while the restoring forces for the two magneto-acoustic modes is a combination of the total pressure gradient and magnetic tension. Table 2.1 presents a brief summary of the results in this section. For $\beta \ll 1$, which is often relevant in chromospheric conditions, the fast mode is approximately isotropic while the slow mode along with the Alfvén mode exhibit a strong anisotropy and both have a *preferred* propagation direction along the magnetic field while they do not propagate in directions perpendicular to the magnetic field.

Table 2.1: Phase speeds of the slow, fast magneto-acoustic and Alfvén waves for a uniform unbounded magnetised plasma.

		$\beta \gg 1$, $v_A \ll v_S$	$\beta \ll 1$, $v_A \gg v_S$
$\boldsymbol{k} \cdot \boldsymbol{v}' = 0$	$\boldsymbol{k} \| \boldsymbol{B}$	• Alfvén wave, $v_{ph}^2 \sim v_A^2$.	• Alfvén wave, $v_{ph}^2 \sim v_A^2$.
	$\boldsymbol{k} \perp \boldsymbol{B}$	• Alfvén wave, does not propagate.	• Alfvén wave, does not propagate.
$\boldsymbol{k} \cdot \boldsymbol{v}' \neq 0$	$\boldsymbol{k} \| \boldsymbol{B}$	• Fast wave, $v_{ph}^2 \sim v_S^2$, approximately isotropic, magnetic and kinetic pressure in phase. • Slow wave, $v_{ph}^2 \sim v_A^2$, magnetic and kinetic pressure out of phase.	• Fast wave, $v_{ph}^2 \sim v_A^2$, approximately isotropic, magnetic and kinetic pressure in phase. • Slow wave, $v_{ph}^2 \sim v_S^2$, magnetic and kinetic pressure out of phase.
	$\boldsymbol{k} \perp \boldsymbol{B}$	• Fast wave, $v_{ph}^2 \sim v_S^2$, approximately isotropic, magnetic and kinetic pressure in phase. • Slow wave, does not propagate.	• Fast wave, $v_{ph}^2 \sim v_A^2$, approximately isotropic, magnetic and kinetic pressure in phase. • Slow wave, does not propagate.

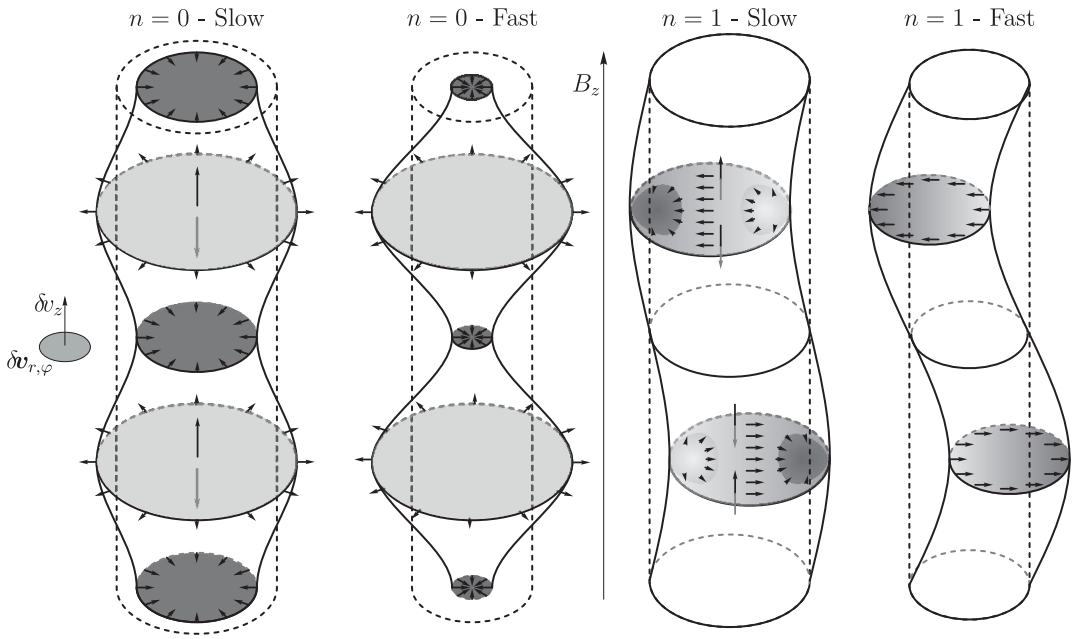

Figure 2.2: Schematic diagrams of MHD waves in synthetic cylindrical wave-guides. The velocity perturbations in the z direction, denoted by δv_z, are depicted with vertical arrows within the tube while the velocity perturbations in the (r, φ)-plane, $\delta \boldsymbol{v}_{r,\varphi}$, are illustrated with horizontal arrows. The horizontal plane cuts on the flux tubes illustrate the density perturbation with darker colours signifying a relatively higher density to the equilibrium density, the opposite is true for brighter colours. The two schematics to the left represent slow and fast sausage modes ($n = 0$), while the two figures to the right represent slow and fast kink modes ($n = 1$). Notice that for slow modes the main component of the velocity perturbation is in the z direction, which is associated with, relatively to the fast modes, stronger density perturbations.

2.1.3 Wave Modes in a Magnetic Flux Tube

Another geometric configuration of relevance in the solar atmosphere is a straight magnetic cylinder. Edwin and Roberts (1983) considered the case for constant magnetic field inside, $B_i\hat{\boldsymbol{z}}$, and outside, $B_e\hat{\boldsymbol{z}}$, the flux tube with a discontinuity at the tube boundary $r = r_a$, where r_a is the tube radius. Similarly the equilibrium density and pressure inside and outside the tube are taken to be ρ_i, p_i and ρ_e, p_e respectively. The resulting dispersion relations, assuming no energy propagation towards or away from the flux tube are the following (Edwin and Roberts (1983)),

$$m_i\rho_e(k_z^2v_{Ae}^2 - \omega^2)\frac{K_n(m_er_a)}{K_n'(m_er_a)} = m_e\rho_i(k_z^2v_{Ai}^2 - \omega^2)\frac{I_n(m_ir_a)}{I_n'(m_ir_a)}, \text{ for } m_i^2 > 0, \tag{2.14}$$

$$n_0\rho_e(k_z^2v_{Ae}^2 - \omega^2)\frac{K_n(m_er_a)}{K_n'(m_er_a)} = m_e\rho_i(k_z^2v_{Ai}^2 - \omega^2)\frac{J_n(n_0r_a)}{J_n'(n_0r_a)}, \text{ for } -m_i^2 = n_0^2 > 0, \tag{2.15}$$

where,

$$m_i^2 = \frac{(k_z^2 v_{si}^2 - \omega^2)(k_z^2 v_{Ai}^2 - \omega^2)}{(v_{Ai}^2 + v_{si}^2)(k_z^2 v_{Ti}^2 - \omega^2)}, \tag{2.16}$$

$$m_e^2 = \frac{(k_z^2 v_{se}^2 - \omega^2)(k_z^2 v_{Ae}^2 - \omega^2)}{(v_{Ae}^2 + v_{se}^2)(k_z^2 v_{Te}^2 - \omega^2)}, \tag{2.17}$$

are the internal and external radial wavenumbers, n is the azimuthal wavenumber and k_z is the longitudinal wavenumber which, in the present work, is along the $\hat{\boldsymbol{z}}$ direction. For the case where $m_i^2 > 0$ the amplitude of the resulting eigenmodes are heavily localised near the boundary of the flux tube (see Equation (2.14)) and so these are referred to as surface modes. When $m_i^2 < 0$ the behaviour of the solutions inside the flux tube is oscillatory and since only evanescent solutions are permitted outside the flux tube, i.e. $m_e^2 > 0$, the largest wave amplitudes are observed inside and in the vicinity of the flux tube, these modes are referred to as body waves. The schematic diagram in Figure 2.2 depicts velocity and density perturbations characteristic to the fast and slow magneto-acoustic modes for $n = 0$ (sausage mode) and $n = 1$ (kink mode).

Surface and body waves exhibit similar characteristics associated with the slow and fast magneto-acoustic and the Alfvén mode. However, these modes have a substantially different behaviour when compared with the eigenmodes studied in Section 2.1.2. The parallel component of the wavevector, $\boldsymbol{k}$, to the magnetic field $\boldsymbol{B}$ is here k_z. The azimuthal wavevector, n, and the radial wavevectors, m_i or m_e, form the perpendicular components to the equilibrium magnetic field. With that in mind let us explore the similarities and differences of the corresponding eigenmodes in Section 2.1.2 and the modes present in a magnetic flux tube. The fast magneto-acoustic mode in Section 2.1.2 for the case where $\beta \ll 1$ was approximately isotropic, the fast mode in the magnetic cylinder case is highly anisotropic and also does not exist for some azimuthal wavenumbers. The main restoring force for the fast sausage mode ($n = 0$) is the total pressure while magnetic tension has only a minor role, while the fast kink mode ($n = 1$) appears to be nearly incompressible and the main restoring force is magnetic tension (see Figure 2.8 and 2.2). Despite the differences between the eigenmodes for the uniform medium and the magnetic flux tube the velocities of the three modes present for the magnetic flux tube case are still mutually perpendicular to one another. The practical implication of this is that the slow and the Alfvén modes are incredibly difficult to detect in a flux

tube as there is heavy dependence on the spatial resolution of spectroscopic methods. The *fast magneto-acoustic* mode is most prominently detectable. However, even for this mode only the sausage mode has been successfully observed, corresponding to the azimuthal wavenumber $n = 0$ and the kink mode ($n = 1$), while modes with $n > 1$ are yet to be observed mainly due to limitations in the spatio-temporal resolution of the instruments used.

The Alfvén modes in Figures (2.3) and (2.4) were calculated using Equations (7)–(9) by Spruit (1982), i.e.

$$\nabla \cdot \mathbf{v} = 0, \tag{2.18a}$$
$$\mathbf{v}_z = 0, \tag{2.18b}$$
$$\mathbf{v} = \mathbf{0}, \text{ outside the tube.} \tag{2.18c}$$

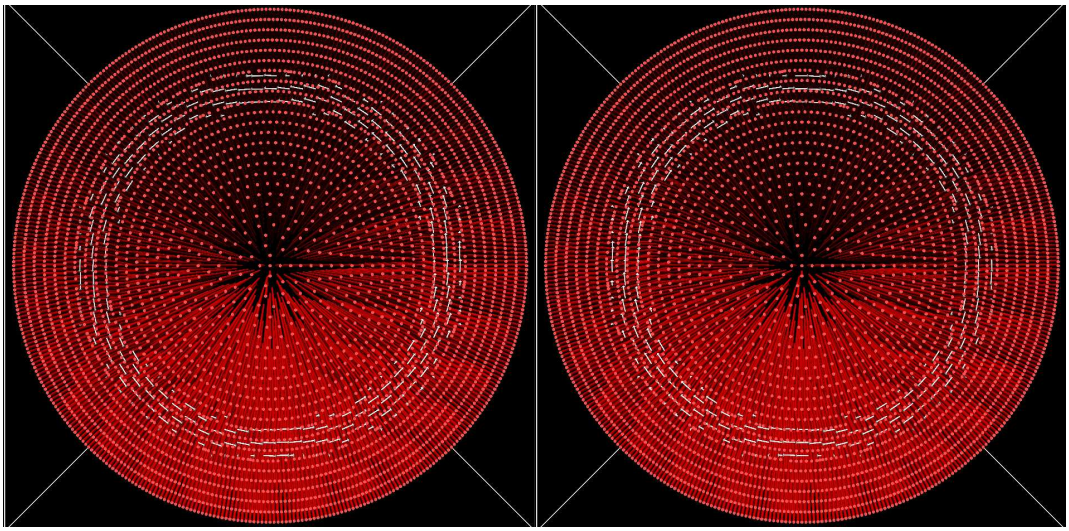

Figure 2.3: The two extrema of the Alfvén mode for $n = 0$. This mode is also referred to as torsional Alfvén mode. In this figure and in Figure 2.4-2.8, the red *ropes* represent the magnetic field lines, the white arrows the velocity field. A simulation of this mode is also available at a higher resolution at `http://swat.group.shef.ac.uk/fluxtubecontent/alfven/n0_eig.html`

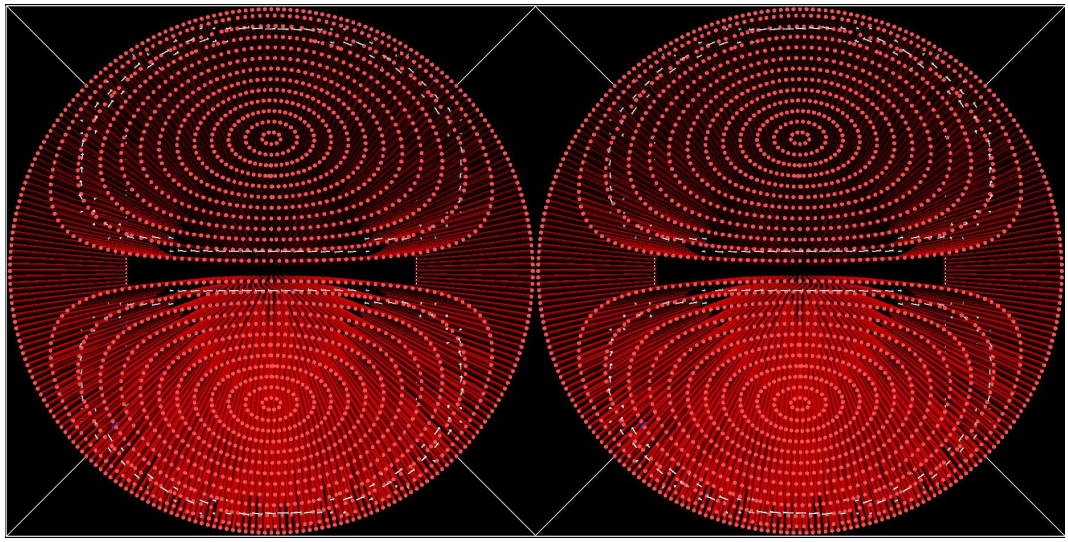

Figure 2.4: The Alfvén mode for $n = 1$. Notice that the magnetic surfaces are decoupled, but are more intricate compared with the torsional Alfvén mode (Figure 2.3). A simulation of this mode is also available at a higher resolution at `http://swat.group.shef.ac.uk/fluxtubecontent/alfven/n1_eig.html`

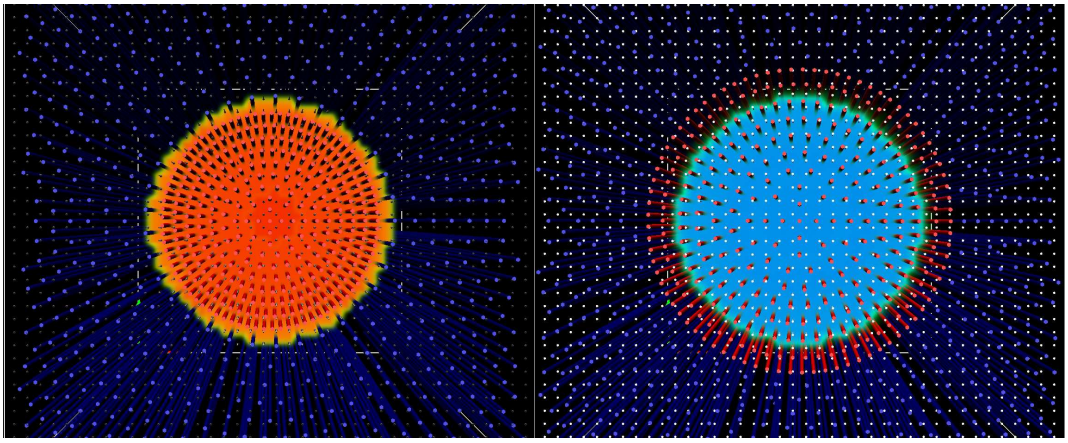

Figure 2.5: The slow sausage mode ($n = 0$). Notice that the dominant velocity component is in the direction along the flux tube. A positive density perturbation (ρ') is highlighted with warmer colours with *red* denoting the maximum and a negative density perturbation is illustrated with cooler colours with *blue* the minimum. Lastly the blue *ropes* represent the magnetic field outside the flux tube. The density perturbation and external magnetic field are represented in similar fashion in Figure 2.6-2.8. See `http://swat.group.shef.ac.uk/fluxtubecontent/sausage/n0slow1.html` for a higher resolution simulation.

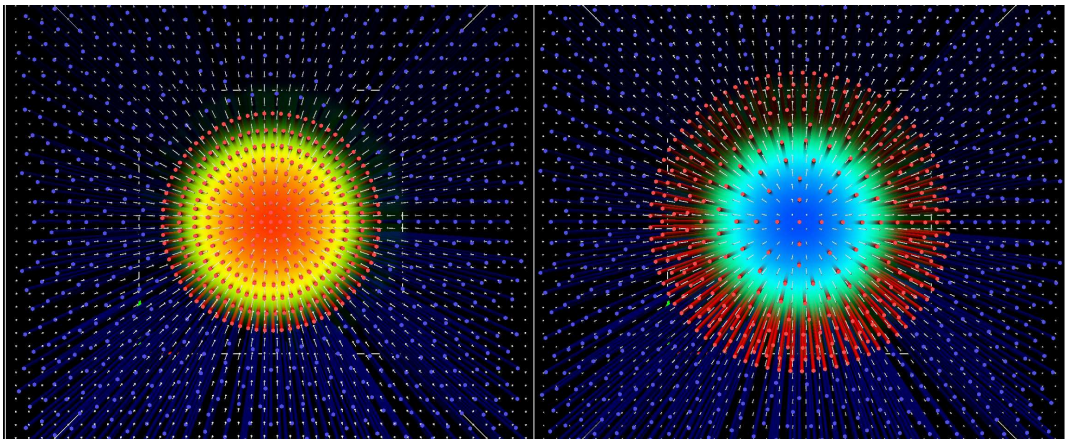

Figure 2.6: The fast sausage mode ($n = 0$). Note that the velocity component along the magnetic field is zero for this mode. See `http://swat.group.shef.ac.uk/fluxtubecontent/sausage/n0fast1.html` for a simulation of this mode.

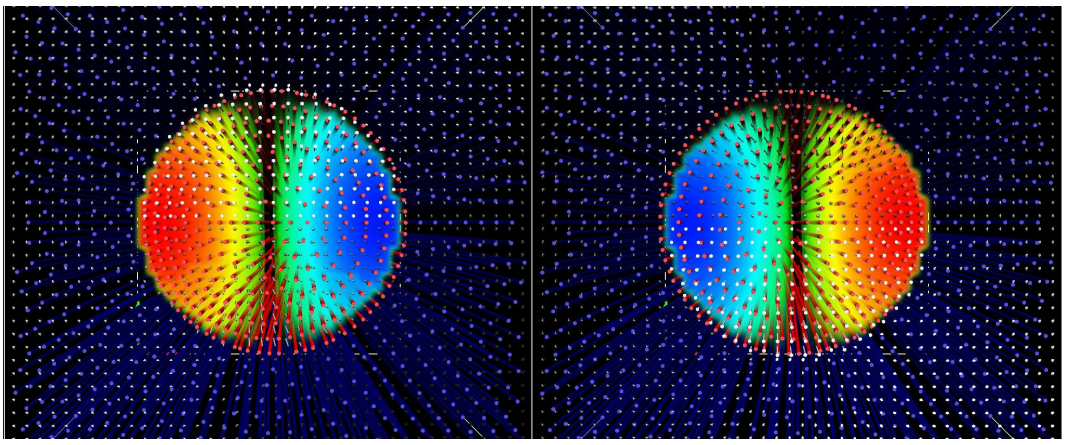

Figure 2.7: The slow kink mode ($n = 1$). As with the slow sausage mode, the dominant component of the velocity field is along the direction of the magnetic field. See `http://swat.group.shef.ac.uk/fluxtubecontent/kink/n1slow1.html` for a simulation of this mode.

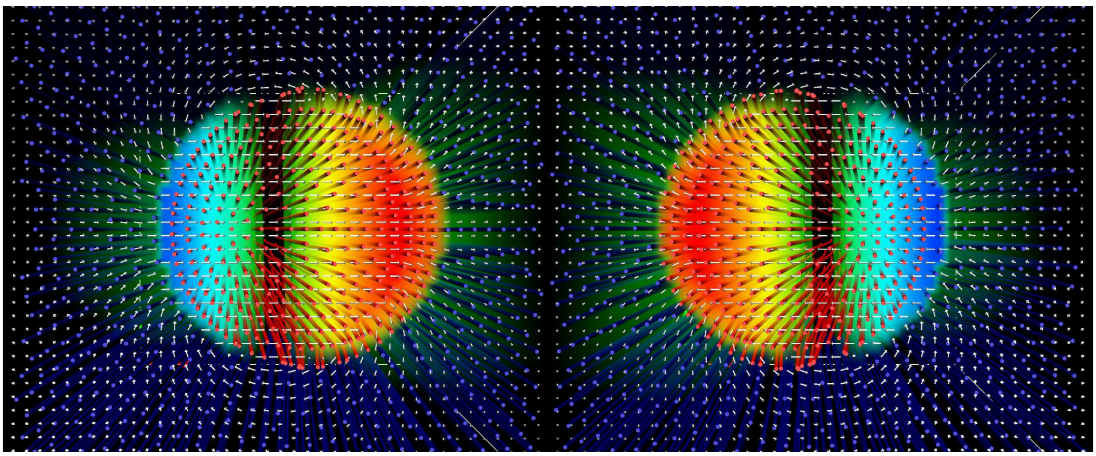

Figure 2.8: The fast kink mode ($n = 1$). Note that the velocity component along the magnetic field is zero for this mode as it is the case for the fast sausage mode Figure 2.6. Another notable feature of this mode is that the divergence of the velocity inside the flux tube is zero, which suggests that this mode is (nearly) incompressible. See `http://swat.group.shef.ac.uk/fluxtubecontent/kink/n1fast1.html` for a simulation of this mode.

Chapter 3

Axisymmetric Modes in Magnetically Twisted Flux Tubes

Observations suggest that twisted magnetic flux tubes are ubiquitous in the Sun's atmosphere, with the Chapter 5 suppliying reinforcing evidence towards that view. The main aim of this chapter is to advance the study of axisymmetric modes of magnetic flux tubes by modelling both twisted internal and external magnetic field, when the magnetic twist is weak. The focus of this chapter and Chapter 4 is on axisymmetric modes in twisted magnetic flux tubes. This focus stems from: i) the intuition that axisymmetric modes have the simplest symmetry, and therefore the conditions for exciting these modes should be abundant on the solar atmosphere, ii) these modes have been relatively neglected when compared with the number of studies considering the kink mode (starting with the works by Aschwanden et al., 1999; Nakariakov et al., 1999) and iii) in contrast to fluting modes, axisymmetric modes have been observed (e.g. Morton et al., 2012).

In this chapter the derived dispersion relations are solved numerically assuming that the twist outside the tube is inversely proportional to the distance from its boundary. The case of constant magnetic twist outside the tube is studied and an analytical solution is presented. It is shown that the solution for a constant twist outside the tube is a good approximation to the case where the magnetic twist is proportional to $1/r$, namely the error is in all cases less than 5.4%. The solution is in excellent agreement with solutions to simpler models of twisted magnetic flux tubes, i.e. without external magnetic twist. It is shown that axisymmetric Alfvén waves are naturally coupled with magnetic twist as the azimuthal component of the velocity perturbation is non-zero.

The theoretical results of this chapter are then compared with observations and insight is provided about the expected Doppler signature of these modes. Lastly, it is argued that the character of axisymmetric waves in twisted magnetic flux tubes can lead to false positives in identifying observations with axisymmetric Alfvén waves.

3.1 Introduction

There is ample evidence of twisted magnetic fields in the solar atmosphere and below the photosphere. It has been suggested that magnetic flux tubes are twisted whilst rising through the convection zone (see for example Murray and Hood, 2008; Hood et al., 2009; Luoni et al., 2011). Brown et al. (2003), Yan and Qu (2007) and Kazachenko et al. (2009) have shown that sunspots exhibit a relatively uniform rotation which, in turn, twists the magnetic field lines emerging from the umbra. Several studies argue that the chromosphere is also permeated by structures that appear to exhibit torsional motion (De Pontieu et al., 2012; Sekse et al., 2013). These structures, known as type II spicules, were initially identified by De Pontieu et al. (2007). De Pontieu et al. (2012) show that spicules exhibit a dynamical behaviour that has three characteristic components, i) flows aligned to the magnetic field, ii) torsional motion and iii) what the authors describe as swaying motion. Recent evidence shows that twist and Alfvén waves present an important mechanism of energy transport from the photosphere to the corona (Wedemeyer-Böhm et al., 2012). The increasing body of observational evidence of magnetic twist in the solar atmosphere, in combination with ubiquitous observations of sausage waves (Morton et al., 2012), reinforce the importance of refining our theoretical understanding of waves in twisted magnetic and especially axisymmetric modes as these could be easily perceived as torsional Alfvén waves.

Early studies of twisted magnetic flux tubes focused on stability analyses. For example, Shafranov (1957) investigated the stability of magnetic flux tubes with azimuthal component of magnetic field proportional to r inside the cylinder and no magnetic twist outside. Kruskal et al. (1958) derived approximate solutions for magnetic flux tubes with no internal twist embedded in an environment with $B_\varphi \propto 1/r$. Bennett et al. (1999) obtained solutions for the sausage mode for stable uniformly twisted magnetic flux tubes with no external twist while Erdélyi and Fedun (2006) extended the analysis for the incompressible case of constant twist outside the flux tube. The authors

also examined the impact of twist on the oscillation periods in comparison to earlier studies (e.g. Edwin and Roberts, 1983) considering magnetic flux tubes with no twist. In a subsequent work Erdélyi and Fedun (2007) extended their earlier study (Erdélyi and Fedun, 2006) to the compressible case for the sausage mode with no twist outside the tube. Karami and Bahari (2010) investigated kink and fluting modes in incompressible flux tubes. The twist was considered to be proportional to r for all r, which is unphysical as it grows to infinity as $r \to \infty$, while the density profile considered was piecewise constant with a linear function connecting the internal and external densities. The authors revealed that the wave frequencies for the kink and fluting modes are directly proportional to the magnetic twist. Terradas and Goossens (2012) investigated twisted flux tubes with magnetic twist localised within a toroidal region of the flux tube and zero everywhere else. Terradas and Goossens (2012) argue that for small twist the main effect of standing oscillations is the change in polarization of the velocity perturbation in the plane perpendicular to the longitudinal dimension (z-coordinate).

The aim of this chapter is the study of axisymmetric modes, namely eigenmodes corresponding to $k_\varphi = 0$, where k_φ is the azimuthal wavenumber in cylindrical geometry[1]. We focus on axisymmetric modes as they are relatively scarcely studied, compared with the kink mode, and intuitively, their close connection with Alfvén waves when twist is introduced. The azimuthal magnetic field inside the tube is $\propto r$, while the azimuthal field outside is constant. If there is a current along the tube, according to the Biot-Savart law, this current will give rise to a twist proportional to r inside the flux tube and a twist inversely proportional to r outside. For this reason the analysis is started with the assumption that the magnetic twist outside the tube is proportional to $1/r$. A perturbation parameter is inserted so as to revert to the case with constant twist. Subsequently, an exact solution is presented for the case with constant twist outside the tube and solved numerically for the case with magnetic twist proportional to $1/r$. Then, the numerical solution for $1/r$ is compared with the exact solution for constant twist. Based on the obtained estimated standard error, the solution corresponding to weak constant twist appears to be a good approximation to the solution with weak magnetic twist that is proportional to $1/r$. In the case where there is a pre-existing twist inside the cylinder, assuming this twist is uniform, this will give rise to a current

[1] k_φ is often denoted as m in a number of other studies.

which, in turn, will create the external twist that is again inversely proportional to the distance from the cylinder. The latter case may occur, for example, due to vortical foot-point motions on the photosphere (Ruderman et al., 1997) or indeed the intensity vortices studied in Chapter 5. Recent observational evidence (e.g. Morton et al., 2013) put the assumptions of Ruderman et al. (1997) on a good basis, however, the vortical motions in Morton et al. (2013) are not divergence free which means that the same mechanism can be responsible for the axisymmetric modes studied in this chapter.

The rest of this chapter is organised as follows. In Section 3.2 the model geometry and the employed MHD equations are described. In Section 3.3 a derivation of the dispersion relation for $k_\varphi = 0$ is presented, and, in Section 3.3.3 limiting cases connecting the results in this work with previous models are explored. Furthermore, in Section 3.4 a number of physically relevant cases are elaborated upon. In, Section 3.5 the applicability and potential limitations of the presented model are explored. In Section 3.6 we summarise the main results of this chapter.

3.2 Model Geometry and Basic Equations

The single-fluid linearised ideal MHD equations in the force formalism are (Kadomtsev, 1966),

$$\rho\frac{\partial^2\boldsymbol{\xi}}{\partial t^2} + \nabla p' + \frac{1}{\mu_0}\left(\boldsymbol{B}'\times(\nabla\times\boldsymbol{B}) + \boldsymbol{B}\times(\nabla\times\boldsymbol{B}')\right) = 0, \tag{3.1a}$$

$$p' + \boldsymbol{\xi}\cdot\nabla p + \gamma p\nabla\cdot\boldsymbol{\xi} = 0, \tag{3.1b}$$

$$\boldsymbol{B}' + \nabla\times(\boldsymbol{B}\times\boldsymbol{\xi}) = 0, \tag{3.1c}$$

where, ρ, p and $\boldsymbol{B}$ are the density, kinetic pressure and magnetic field, respectively, at equilibrium, $\boldsymbol{\xi}$ is the Lagrangian displacement vector, p' and $\boldsymbol{B}'$ are the pressure and magnetic field perturbation, respectively, γ is the ratio of specific heats (taken to be 5/3 in this work), and μ_0 is the permeability of free space. In this study we employ cylindrical coordinates (r, φ, z) and therefore $\boldsymbol{\xi} = (\xi_r, \xi_\varphi, \xi_z)$ and $\boldsymbol{B}' = (B'_r, B'_\varphi, B'_z)$. In what follows an index i indicates quantities inside the flux tube ($r < r_a$), while variables indexed by e refer to the environment outside the flux tube ($r > r_a$). The model geometry is illustrated in Figure 3.1 when $B_{\varphi e} \propto 1/r$. For static equilibrium,

$$\nabla\cdot\boldsymbol{B} = 0, \tag{3.2a}$$

$$\boldsymbol{J} = \frac{1}{\mu_0}\nabla\times\boldsymbol{B}, \tag{3.2b}$$

$$\nabla p = \boldsymbol{J}\times\boldsymbol{B}, \tag{3.2c}$$

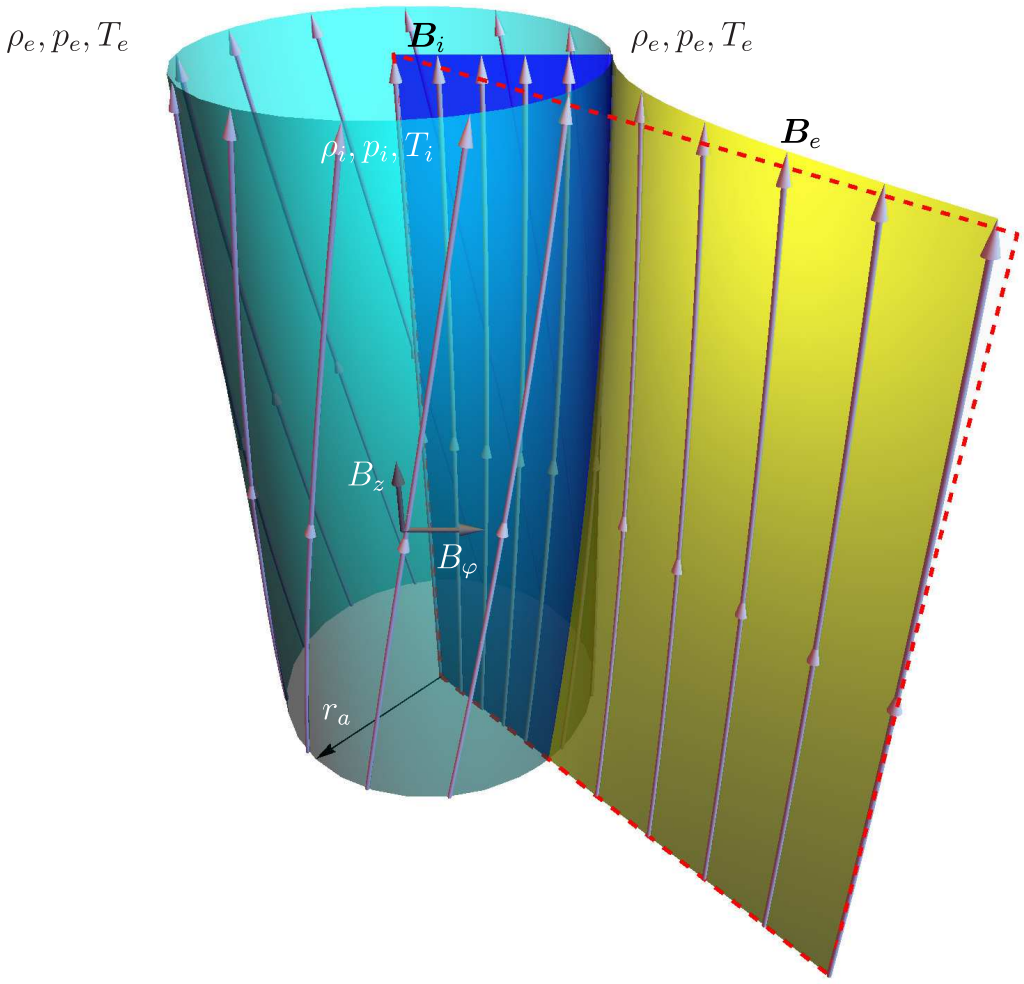

Figure 3.1: Model illustration. We consider a straight magnetic cylinder with variable twist inside ($r < r_a$) and outside ($r > r_a$), where r_a is the tube radius, ρ_i, p_i and T_i are the density, pressure and temperature at equilibrium inside the tube. The corresponding quantities outside the tube are denoted by a subscript e. B_φ is continuous across the tube boundary. The dark blue surface inside the magnetic cylinder represents the influence of $B_\varphi \propto r$. The yellow surface outside the cylinder illustrates the $B_\varphi \propto 1/r$ dependence. The dashed red rectangle represents a magnetic surface with only a longitudinal (z) magnetic field component.

where $\boldsymbol{J}$is the current density. It is assumed that, ρ, p and $\boldsymbol{B}$ have only an r-dependence. The magnetic field is considered to have the form,

$$\boldsymbol{B} = (0, B_\varphi(r), B_z(r)). \tag{3.3}$$

Notice that in cylindrical coordinates, Equation (3.2a) is identically satisfied. Then, Equation (3.2b) expands to

$$\mu_0 \boldsymbol{J} = \left(0, -\frac{dB_z}{dr}, \frac{1}{r}\frac{d(rB_\varphi)}{dr}\right). \tag{3.4}$$

Using Equation (3.4), Equation (3.2c) becomes

$$\nabla p = \left(-\frac{B_z}{\mu_0}\frac{\partial B_z}{\partial r} - \frac{B_\varphi}{\mu_0 r}\frac{d(rB_\varphi)}{dr}, 0, 0\right). \tag{3.5}$$

Therefore, the pressure force in the φ and z directions is constant and the magnetic field and the plasma pressure must satisfy the pressure balance equation in the r direction, i.e.

$$\frac{d}{dr}\left(p + \frac{B_\varphi^2 + B_z^2}{2\mu_0}\right) + \frac{B_\varphi^2}{\mu_0 r} = 0. \tag{3.6}$$

The φ component of the magnetic field outside the flux tube is assumed to be $\propto 1/r$. This assumption is motivated by the experiments conducted by Biot and Savart (1820) and Ampére (1820-1825) (pp. 175 Jackson, 1999) on current carrying wires. Their results are summarised by the following formulation (pp. 175-178 Jackson, 1999):

$$d\mathbf{B} = \frac{\mu_0 I}{4\pi}\frac{d\mathbf{l} \times \mathbf{x}}{|\mathbf{x}|^3}, \tag{3.7}$$

where, $d\mathbf{B}$ is the infinitesimal magnetic induction at a point P, I is the current along the wire, $d\mathbf{l}$ is the infinitesimal vector along the wire and $\mathbf{x}$ is the vector from $d\mathbf{l}$ to the point P. (3.7) describes an inverse square law and when integrated along a straight infinitely long wire results in the following for the magnitude of the φ component of the magnetic field:

$$\frac{\mu_0 I}{2\pi r}, \tag{3.8}$$

while the other components of the magnetic field due to the current are zero. Based on Equation (3.8) and for *thin* magnetic flux tubes according to the Biot-Savart law (for $\kappa = 1$ in Equation (3.9)) a reasonable assumption for the form of the magnetic field is,

$$\boldsymbol{B} = \begin{cases} (0, S_i r, B_{zi}) & \text{for } r \le r_a, \\ \left(0, r_a^{1+\kappa} S_e / r^\kappa, B_{ze}\right) & \text{for } r > r_a, \end{cases} \tag{3.9}$$

where, B_{zi}, B_{ze}, S_i and S_e are constants and κ is a perturbation parameter. The perturbation parameter has been inserted in Equation (3.9) in such a way so as to preserve dimensional consistency. The constant S_i can be determined by application of the Biot-Savart law and is therefore taken to be,

$$S_i = \frac{\mu_0 I}{2\pi r_a^{1+\kappa}}, \tag{3.10}$$

where I is the current. The assumption here is that the flux tube is *thin* (see Chapter 5.2, Equation 5.6 Classical Electrodynamics by Jackson (1999)). By substituting Equation (3.9) into Equation (3.6) we obtain:

$$p(r) = \begin{cases} \dfrac{S_i^2}{\mu_0}(r_a^2 - r^2) + p_a & \text{for } r \leq r_a, \\ \dfrac{r_a^{2(1+\kappa)} S_e^2 (1-2\kappa)}{2\mu_0 \kappa} \left(\dfrac{1}{r^{2\kappa}} - \dfrac{1}{r_a^{2\kappa}} \right) + p_a & \text{for } r > r_a, \end{cases} \tag{3.11}$$

where, p_a, is the pressure at the boundary of the magnetic flux tube. The constant, S_e, is equal to S_i, however notational distinction allows for the separation of the internal and external environments to the flux tube which helps with the validation these results with previous work (e.g. Erdélyi and Fedun, 2007).

3.2.1 Governing Equations

The solution of the system of equations shown in Equation (3.1), in cylindrical coordinates can be found by Fourier decomposition of the perturbed components, namely the perturbed quantities are taken to be,

$$\boldsymbol{\xi}, p_T' \propto e^{i(k_\varphi \varphi + k_z z - \omega t)}, \tag{3.12}$$

where, ω is the angular frequency, k_φ is the azimuthal wavenumber for which only integer values are allowed and, k_z is the longitudinal wavenumber in the z direction. The Eulerian total pressure perturbation is $p_T' = p' + \boldsymbol{B}\boldsymbol{B}'/\mu_0$, which is obtained by linearisation of the total pressure: $p_T = (p + p') + (\boldsymbol{B} + \boldsymbol{B}')^2/(2\mu_0)$ and p is the equilibrium kinetic pressure. Note that for the sausage mode, considered in this work, the azimuthal wavenumber is $k_\varphi = 0$. Combining Equation (3.1) with Equation (3.12) we obtain the equation initially derived by Hain and Lust (1958) and later by Goedbloed (1971); Sakurai et al. (1991a), to name but a few. This equation can be reformulated as two coupled first order differential equations,

$$D\frac{d(r\xi_r)}{dr} = C_1(r\xi_r) - rC_2p_T', \tag{3.13a}$$
$$D\frac{dp_T'}{dr} = \frac{1}{r}C_3(r\xi_r) - C_1p_T'. \tag{3.13b}$$

and the multiplicative factors are defined as:

$$D = \rho(\omega^2 - \omega_A^2)C_4, \tag{3.14a}$$
$$C_1 = \frac{2B_\varphi}{\mu_0 r}\left(\omega^4 B_\varphi - \frac{k_\varphi}{r}f_B C_4\right), \tag{3.14b}$$
$$C_2 = \omega^4 - \left(k_z^2 + \frac{k_\varphi^2}{r^2}\right)C_4, \tag{3.14c}$$
$$\begin{aligned} C_3 = \rho D\left[\omega^2 - \omega_A^2 + \frac{2B_\varphi}{\mu_0\rho}\frac{d}{dr}\left(\frac{B_\varphi}{r}\right)\right] \\ + 4\omega^4\frac{B_\varphi^4}{\mu_0^2 r^2} - \rho C_4\frac{4B_\varphi^2\omega_A^2}{\mu_0 r^2}, \end{aligned} \tag{3.14d}$$
$$C_4 = (v_s^2 + v_A^2)(\omega^2 - \omega_c^2), \tag{3.14e}$$

where,

$$\omega_c^2 = \frac{v_s^2}{v_A^2 + v_s^2}\omega_A^2, \qquad \omega_A^2 = \frac{f_B^2}{\mu_0\rho}, \qquad f_B = \frac{k_\varphi}{r}B_\varphi + k_z B_z.$$

Here, $v_s = \sqrt{\gamma p/\rho}$ is the sound speed, $v_A = |\boldsymbol{B}|/\sqrt{\mu_0\rho}$ is the Alfvén speed, ω_c is the cusp angular frequency and ω_A is the Alfvén angular frequency. The coupled first order ODEs in Equation (3.13) can be combined into a single second order ODE for, p_T' or ξ_r. In this work latter approach is selected, namely:

$$\frac{d}{dr}\left[\frac{D}{rC_2}\frac{d}{dr}(r\xi_r)\right] + \left[\frac{1}{D}\left(C_3 - \frac{C_1^2}{C_2}\right) - r\frac{d}{dr}\left(\frac{C_1}{rC_2}\right)\right]\xi_r = 0. \tag{3.15}$$

Using flux coordinates and assuming $k_\varphi = 0$, it can be shown that (Sakurai et al., 1991a),

$$\rho(\omega^2 - \omega_A^2)\xi_\perp = -ik_z B_\varphi\frac{1}{|\boldsymbol{B}|}\left(p_T' + 2\frac{B_z^2}{\mu_0 r}\xi_r\right), \tag{3.16a}$$
$$\rho(\omega^2 - \omega_c^2)\xi_\parallel = ik_z B_z\frac{v_s^2}{|\boldsymbol{B}|}\frac{1}{v_s^2 + v_A^2}\left(p_T' - 2\frac{B_\varphi^2}{\mu_0 r}\xi_r\right). \tag{3.16b}$$

Here $\xi_\parallel$ and $\xi_\perp$ are the Lagrangian displacement components parallel and perpendicular to the magnetic field lines respectively. The dominant component of the Lagrangian displacement vector $(\xi_r, \xi_\perp, \xi_\parallel)$ determines the character of the mode. For the Alfvén mode the $\xi_\perp$ component is dominant, while for the slow and fast magneto-acoustic

modes $\xi_\parallel$ and ξ_r is dominant respectively (Goossens et al., 2011). Equation (3.16) suggests that in the presence of magnetic twist the slow and fast magneto-acoustic modes are coupled to the Alfvén mode even when $k_\varphi = 0$, namely the slow and fast modes do not exist without the Alfvén mode and vice versa. This is because for the Alfvén mode to be decoupled from the slow and fast magneto-acoustic modes it is required that for $\xi_\perp \neq 0$, $\xi_r = 0$ and $\xi_\parallel = 0$. However, it follows trivially from Equation (3.13) that, if $\xi_r = 0$ then also $p_T' = 0$ and therefore from Equation (3.16) we have that $\xi_\perp = 0$. From this, it follows that the Alfvén mode cannot exist without the components corresponding to the slow and fast magneto-acoustic modes, hence the Alfvén mode is coupled with the slow and fast magneto-acoustic modes. Furthermore, from Equation (3.16) we can also see that for a solution, i.e. (ω, k_z) pair, as ω approaches ω_A, the $\xi_\perp$ component is amplified that leads to the azimuthal component of the displacement to be accentuated.

3.3 Dispersion Equation

In this section we follow a standard procedure in deriving a dispersion equation, namely we solve Equation (3.15) inside and outside the flux tube and match the two solutions using the boundary conditions. The boundary conditions that must be satisfied are:

$$\xi_{ri}|_{r=r_a} = \xi_{re}|_{r=r_a}\,, \tag{3.17a}$$

$$p_{Ti}' - \frac{B_{\varphi i}^2}{\mu_0 r}\xi_{ri}\bigg|_{r=r_a} = p_{Te}' - \frac{B_{\varphi e}^2}{\mu_0 r}\xi_{re}\bigg|_{r=r_a}\,, \tag{3.17b}$$

where, Equation (3.17a) and Equation (3.17b) are continuity conditions for the Lagrangian displacement and total pressure across the tube boundary respectively.

3.3.1 Solution Inside the Flux Tube

The parameters in Equation (3.14) for the case inside the flux tube for the sausage mode become,

$$D_i = \rho_i(\omega^2 - \omega_{Ai}^2), \tag{3.18a}$$

$$C_1 = \frac{2S_i^2 r}{\mu_0} n_i^2, \tag{3.18b}$$

$$C_2 = n_i^2 - k_z^2, \tag{3.18c}$$

$$C_3 = \rho_i \left[(\omega^2 - \omega_{Ai}^2)^2 + \frac{4S_i^2}{\mu_0\rho_i}\left(\frac{S_i^2 r^2}{\mu_0\rho_i} n_i^2 - \omega_{Ai}^2\right)\right], \tag{3.18d}$$

$$n_i^2 = \frac{\omega^4}{(v_{si}^2 + v_{Ai}^2)(\omega^2 - \omega_{ci}^2)}, \tag{3.18e}$$

where,

$$\omega_{ci}^2 = \frac{v_{si}^2}{v_{Ai}^2 + v_{si}^2}\omega_{Ai}^2, \qquad \omega_{Ai}^2 = k_z^2 \frac{B_{zi}^2}{\mu_0 \rho_i}.$$

The B_φ component is assumed small to avoid the kink instability, see for example (Gerrard et al., 2002; Török et al., 2004). This implies, $B_\varphi \ll B_z$ and since B_φ is a function of r inside (and outside) the tube we require $\sup(B_\varphi) \ll B_z \Rightarrow Sr_a \ll B_z$. This condition is satisfied in the solar atmosphere, so we can use the approximation: $v_{Ai}^2 = (B_{\varphi i}^2 + B_{zi}^2)/(\mu_0\rho_i) \sim B_{zi}^2/(\mu_0\rho_i)$. Notice that according to Equation (3.11) the pressure depends on r, however, in this chapter it is assumed that the sound speed is constant. This is because the term that depends on r in Equation (3.11) is assumed to be small when compared with p_a in solar atmospheric conditions. To see this, consider that $\sup(Sr_a) = 0.2B_z$ and[1] $B_z \sim (10^{-1} - 10^{-4})T$, $T \sim (10^4 - 10^6)K$ and the number density $n \sim (10^{23} - 10^{16})m^{-3}$. This means that[2] $p_a \sim (10^4 - 10^{-1})N \cdot m^{-2}$ and the term that depends on the radius is of the order $(Sr_a)^2/\mu_0 \sim (10^2 - 10^{-4})N \cdot m^{-2}$ and therefore the constant term p_a is $(10^2 - 10^3)$ times larger when compared with the term that has an r dependence. Hence, to a good approximation, the pressure can be assumed to be constant. Note, that the density is discontinuous across the tube boundary and therefore we avoid the Alfvén and slow continua that lead to resonant absorption.

Substitution of the parameters in Equation (3.18) into Equation (3.15), leads to the following second order differential equation (see for example Erdélyi and Fedun, 2007),

$$R^2 \frac{d^2\xi_r}{dR^2} + R\frac{d\xi_r}{dR} - \left(1 + \frac{k_{ri}^2}{k_z^2}R^2 + ER^4\right)\xi_r = 0, \tag{3.19}$$

where,

$$\begin{aligned} R &= k_\alpha r, \\ k_{ri}^2 &= \frac{(k_z^2 v_{si}^2 - \omega^2)(k_z^2 v_{Ai}^2 - \omega^2)}{(v_{Ai}^2 + v_{si}^2)(k_z^2 v_{Ti}^2 - \omega^2)}, \\ E &= \frac{4S_i^4 n_i^2}{\mu_0^2 D_i^2 k_z^2 (1-\alpha^2)^2}, \\ \alpha^2 &= \frac{4S_i^2 \omega_{Ai}^2}{\mu_0 \rho_i (\omega^2 - \omega_{Ai}^2)^2}, \end{aligned}$$

[1] In the following expressions the left number corresponds to typical values on the photosphere while the right number corresponds to typical values of the quantity in the corona.

[2] Here $p = nk_BT$.

$$v_{Ti}^2 = \frac{v_{Ai}^2 v_{si}^2}{v_{Ai}^2 + v_{si}^2}.$$

Here $k_\alpha = k_z(1-\alpha^2)^{1/2}$ is the effective longitudinal wavenumber and v_{Ti} is the internal tube speed. Equation (3.19) was derived and solved before by Erdélyi and Fedun (2007). The solution is expressed in terms of Kummer functions (Abramowitz and Stegun, 2012) as,

$$\xi_r(s) = A_{i1}\frac{s^{1/2}}{E^{1/4}}e^{-s/2}M(a,b;s) + A_{i2}\frac{s^{1/2}}{E^{1/4}}e^{-s/2}U(a,b;s)\,, \tag{3.20}$$

where the parameters, a, b and the variable s are defined as

$$\begin{aligned} a &= 1 + \frac{k_{ri}^2}{4k_z^2 E^{1/2}}, \\ b &= 2, \\ s &= R^2 E^{1/2} \\ &= k_\alpha^2 E^{1/2} r^2, \end{aligned}$$

and A_{i1} and A_{i2} are constants. Furthermore, the total pressure perturbation, p_T', is given by:

$$\begin{aligned} p_T'(s) = {} & A_{i1}\frac{k_a D_i}{n_i^2 - k_z^2}e^{-s/2}\left[\frac{n_i + k_z}{k_z}sM(a,b;s) - 2M(a,b-1;s)\right] \\ & + A_{i2}\frac{k_a D_i}{n_i^2 - k_z^2}e^{-s/2}\left[\frac{n_i + k_z}{k_z}sU(a,b;s) - 2(1-a)U(a,b-1;s)\right]. \end{aligned}$$

Now, considering that solutions at the axis of the flux tube, namely at $r = 0$, must be finite, we take $A_{i2} = 0$ and so

$$\xi_{ri}(s) = A_{i1}\frac{s^{1/2}}{E^{1/4}}e^{-s/2}M(a,b;s)\,, \tag{3.21a}$$

$$p_{Ti}'(s) = A_{i1}\frac{k_a D_i}{n_i^2 - k_z^2}e^{-s/2}\left[\frac{n_i + k_z}{k_z}sM(a,b;s) - 2M(a,b-1;s)\right]. \tag{3.21b}$$

Note that the corresponding equation to Equation (3.21b) had a typographical error in Erdélyi and Fedun (2007) (see Equation (13) in that study).

3.3.2 Solution Outside the Flux Tube

The multiplicative factors in Equation (3.14) outside of the flux tube for the sausage mode, $k_\varphi = 0$, become

$$D_e = \rho_e(\omega^2 - \omega_{Ae}^2), \tag{3.22a}$$

$$C_1 = \frac{2r_a^{2(1+\kappa)}S_e^2}{\mu_0 r^{1+2\kappa}}n_e^2, \tag{3.22b}$$

$$C_2 = n_e^2 - k_z^2, \tag{3.22c}$$

$$\begin{aligned} C_3 = {} & \rho_e^2(\omega^2 - \omega_{Ae}^2)^2 \\ & + \frac{4r_a^{2(1+\kappa)}S_e^2}{\mu_0 r^{2(1+\kappa)}}\left[\frac{r_a^{2(1+\kappa)}S_e^2}{\mu_0 r^{2\kappa}}n_e^2 - \rho_e\omega_{Ae}^2 - \rho_e\frac{(1+\kappa)}{2}(\omega^2 - \omega_{Ae}^2)\right], \end{aligned} \tag{3.22d}$$

$$n_e^2 = \frac{\omega^4}{(v_{se}^2 + v_{Ae}^2)(\omega^2 - \omega_{ce}^2)}, \tag{3.22e}$$

where,

$$\omega_{ce}^2 = \frac{v_{se}^2}{v_{Ae}^2 + v_{se}^2}\omega_{Ae}^2, \qquad \omega_{Ae}^2 = k_z^2\frac{B_{ze}^2}{\mu_0\rho_e}.$$

Equation (3.15) with Equation (3.22) for $\kappa = 1$ corresponds to $B_\varphi \sim 1/r$, however, the resulting ODE is difficult to solve. By setting $\kappa = 0$ we obtain the case for constant twist outside the tube, which is also a zeroth-order approximation to the problem with $\kappa = 1$ (Bender and Orszag, 1999). Note, that it is unconventional to use only the zeroth-order term in perturbative methods, and therefore, to establish the validity of the approximation we estimate the error by solving for $\kappa = 1$ numerically. The estimated error is quoted in the caption of the dispersion diagrams in this work and the process which we followed to obtain this is described in Appendix A.2. Substituting the parameters given in Equation (3.22) into Equation (3.15) we have

$$r^2\frac{d^2\xi_r}{dr^2} + r\frac{d\xi_r}{dr} - \left(k_{re}^2 r^2 + \nu^2(\kappa; r)\right)\xi_r = 0, \tag{3.23}$$

where, k_{re}^2 and ν^2:

$$k_{re}^2 = -(n_e^2 - k_z^2), \tag{3.24}$$

$$\begin{aligned} \nu^2(\kappa; r) = 1 + 2\frac{r_a^{2(1+\kappa)}S_e^2}{\mu_0^2 D_e^2 r^{2\kappa}}\Bigg\{ & 2\frac{r_a^{2(1+\kappa)}S_e^2 n_e^2 k_z^2}{r^{2\kappa}} + \mu_0\rho_e\left[\omega_{Ae}^2(n_e^2(3+\kappa)\right. \\ & \left. - k_z^2(1-\kappa)) - (n_e^2 + k_z^2)(1+\kappa)\omega^2\right]\Bigg\}. \end{aligned} \tag{3.25}$$

Notice that $\nu^2(0; r)$ is independent of r. Therefore, for $\kappa \to 0$, Equation (3.23) is transformed to either the Bessel equation for $k_{re}^2 < 0$ or the modified Bessel equation for $k_{re}^2 > 0$. It should also be noted that $n_e^2 = k_z^2$, namely $k_{re}^2 = 0$, is prohibited since

during the derivation of Equation (3.23) it was assumed that $n_e^2 \neq k_z^2$ to simplify the resulting equation. Therefore, the solution to Equation (3.23) for $\kappa \to 0$, and, assuming no energy propagation away from or towards the cylinder ($k_{re}^2 > 0$), is

$$\xi_r(r) = A_{e1} K_\nu \left(k_{re} r\right) + A_{e2} I_\nu \left(k_{re} r\right). \tag{3.26}$$

On physical grounds we require the solution to be evanescent, i.e. $\xi_r(r) \to 0$ as $r \to 0$, and therefore we must have $A_{e2} = 0$, therefore,

$$\xi_{re}(r) = A_{e1} K_\nu \left(k_{re} r\right). \tag{3.27}$$

From Equation (3.13a), the total pressure perturbation p'_{Te} is

$$p'_{Te} = A_{e1} \left(\frac{\mu_0 (1-\nu) D_e - 2 r_a^2 S_e^2 n_e^2}{\mu_0 r (k_z^2 - n_e^2)} K_\nu (k_{re} r) - \frac{D_e}{k_{re}} K_{\nu-1} (k_{re} r) \right). \tag{3.28}$$

Note that, for the case $k_{re}^2 > 0$ and $S_e \to 0$, namely zero twist outside the cylinder, $\nu^2 \to 1$, thus we recover the solution for ξ_r derived by Edwin and Roberts (1983). The limiting cases for Equations (3.21a) and (3.21b) have been verified to converge to the solutions with no twist inside the magnetic cylinder in Erdélyi and Fedun (2007) in Section 3.3.3.

3.3.3 Dispersion Relation and Limiting Cases

Application of the boundary conditions (see Equations 3.17a and 3.17b) in combination with the solutions for ξ_r and p'_T inside the magnetic flux tube (Equations 3.21a and 3.21b) as well as the solutions in the environment of the flux tube (Equations 3.27 and 3.28) respectively, leads to the following general dispersion equation for a compressible tube in the presence of internal and external magnetic twist,

$$\frac{r_a D_e}{k_{re}} \frac{K_{\nu-1}(k_{re} r_a)}{K_\nu (k_{re} r_a)} = \frac{r_a^2}{\mu_0} \left[\frac{S_i^2}{k_{ri}^2} (n_i + k_z)^2 - \frac{S_e^2}{k_{re}^2} (n_e^2 + k_z^2) \right] + \frac{(1-\nu) D_e}{k_{re}^2} - 2 \frac{D_i}{k_{ri}^2} \frac{M(a, b-1; s)}{M(a, b; s)}. \tag{3.29}$$

In order to validate Equation (3.29) we consider a number of limiting cases. First, in the case when there is no external magnetic twist. In this case $S_e = 0$, and from Equation (3.25) it follows trivially that, $\nu^2(\kappa; r) = 1$. Therefore, Equation (3.29) for no external twist becomes:

$$\frac{r_a D_e}{k_{re}} \frac{K_0(k_{re} r_a)}{K_1 (k_{re} r_a)} = \frac{S_i^2 r_a^2}{\mu_0 k_{ri}^2} (n_i + k_z)^2 - 2 \frac{D_i}{k_{ri}^2} \frac{M(a, b-1; s)}{M(a, b; s)}. \tag{3.30}$$

This equation is in agreement with the dispersion equation obtained by Erdélyi and Fedun (2007) and all the limiting cases therein also apply to Equation (3.29). However, there is one limiting case missing from the analysis by Erdélyi and Fedun (2007), namely for no twist inside and outside the tube with $k_{ri}^2 < 0$, which, in combination to $k_{re}^2 > 0$, corresponds to body wave modes. We complete this analysis here. Starting with the following Bessel function limiting cases: 13.3.1 and 13.3.2 in Abramowitz and Stegun (2012), in the limit of $S_i \to 0$ and $k_{ri}^2 > 0$ we have

$$\lim_{S_i \to 0} \left(M(a, b-1; s) \right) = I_0(k_{ri} r)\,, \tag{3.31a}$$

$$\lim_{S_i \to 0} \left(M(a, b; s) \right) = \frac{2}{k_{ri} r} I_1(k_{ri} r)\,, \tag{3.31b}$$

while for $k_{ri}^2 < 0$ we obtain:

$$\lim_{S_i \to 0} \left(M(a, b-1; s) \right) = J_0(k_{ri} r)\,, \tag{3.32a}$$

$$\lim_{S_i \to 0} \left(M(a, b; s) \right) = \frac{2}{k_{ri} r} J_1(k_{ri} r)\,. \tag{3.32b}$$

Therefore, Equation (3.30) in conjunction with the identities $J_0'(s) = -J_1(s)$, $I_0'(s) = I_1(s)$ and $K_0'(s) = -K_1(s)$ (9.1.28 and 9.6.27 in Abramowitz and Stegun, 2012) in the limit $S_i \to 0$ leads to

$$k_{ri} D_e \frac{K_0(k_{re} r_a)}{K_0'(k_{re} r_a)} = k_{re} D_i \frac{I_0(k_{ri} r_a)}{I_0'(k_{ri} r_a)}, \text{ for } k_{ri}^2 > 0, \tag{3.33}$$

$$|k_{ri}| D_e \frac{K_0(k_{re} r_a)}{K_0'(k_{re} r_a)} = k_{re} D_i \frac{J_0(|k_{ri}| r_a)}{J_0'(|k_{ri}| r_a)}, \text{ for } k_{ri}^2 < 0, \tag{3.34}$$

which are in agreement with the results by Edwin and Roberts (1983) and describe wave modes in the case with no magnetic twist.

3.4 Dispersion Equation Solutions

To explore the behaviour of the sausage mode Equation (3.29) was normalised and solved numerically for different solar atmospheric conditions, see Table 3.1. Normalised quantities are denoted with capitalised indices (see Appendix A.1). The solutions of the dispersion relation depend only on the relative ordering of the magnitudes of the characteristic velocities $(v_{AE}, v_{AI}, v_{SE}, v_{SI})$. The sign of k_{rI}^2 and k_{rE}^2 depends on this ordering and this, in turn, defines the three distinct regions in the dispersion plot, i) regions that contain surface modes (for $k_{rI}^2 > 0$ and $k_{rE}^2 > 0$), ii) regions that contain

Characteristic Speeds Ordering	Type	β_i	β_e
$v_{SE} > v_{SI} > v_{AE} > v_{AI}$	Warm dense tube	> 1	> 1
$v_{SE} > v_{AI} > v_{AE} > v_{SI}$	Cool evacuated tube	$\ll 1$	$\gg 1$
$v_{SE} > v_{SI} > v_{AI} > v_{AE}$	Weak cool tube	> 1	$\gg 1$
$v_{AE} > v_{SI} > v_{AI} > v_{SE}$	Intense warm tube	$\ll 1$	$\ll 1$
$v_{AE} > v_{AI} > v_{SE} > v_{SI}$	Intense cool tube	$\ll 1$	$\ll 1$

Table 3.1: Equilibrium cases considered in this analysis. The normalised characteristic speeds are defined in Appendix A.1.

body modes (for $k_{rI}^2 < 0$ and $k_{rE}^2 > 0$), and, iii) forbidden regions corresponding to $k_{rE}^2 < 0$. Additional comments on the selection of the characteristic speeds are made in Appendix A.3. The non-dimensional dispersion equation is given in Appendix A.1 finally, the solutions for the perturbed quantities in terms of ξ_r and p_T' are given in Appendix A.4.

3.4.1 High plasma-β regime

Based on the results by Vernazza et al. (1981) and the model for the plasma-β in the solar atmosphere introduced by Gary (2001), we anticipate that the results in this section are pertinent to conditions typically observed in the upper photosphere, lower chromosphere and mid-chromosphere. The solutions of the dispersion relation in Equation (3.29), in terms of the non-dimensional phase speed, $v_F = v_{ph}/v_{Ai} = \omega/k_z v_{Ai}$, and the non-dimensional longitudinal wave-vector, $\mathcal{K} = k_z r_a$, for a warm dense tube (see Table 3.1) are shown in Figure 3.2. For this case the ordering of the characteristic speeds is as follows: $v_{SE} > v_{SI} > v_{AE} > v_{AI}$. In this figure, and in the following, we over-plot two cases, i) $B_{\varphi i}/B_{zi} = 0.01$ and, ii) $B_{\varphi i}/B_{zi} = 0.2$, which correspond to (practically) no twist and small twist, respectively. The reason for using a small, but non-zero twist for the case corresponding to the dispersion relation with zero twist which we have shown to be equivalent to the result by Edwin and Roberts (1983), is that the limits of the Kummer functions in Equation (3.31) and Equation (3.32) require an increasing number of terms as $a_i \to 0$ and their calculation becomes inefficient by direct summation. However, $B_{\varphi i}/B_{zi} = 0.01$ is a good approximation to the case with zero azimuthal magnetic field component. Note that in the following we take the twist, namely $B_\varphi(r)$, to be continuous across the flux tube and thus set, $S_i = S_e$. The behaviour of the fast sausage body waves (FSBW) is very similar for both the case with

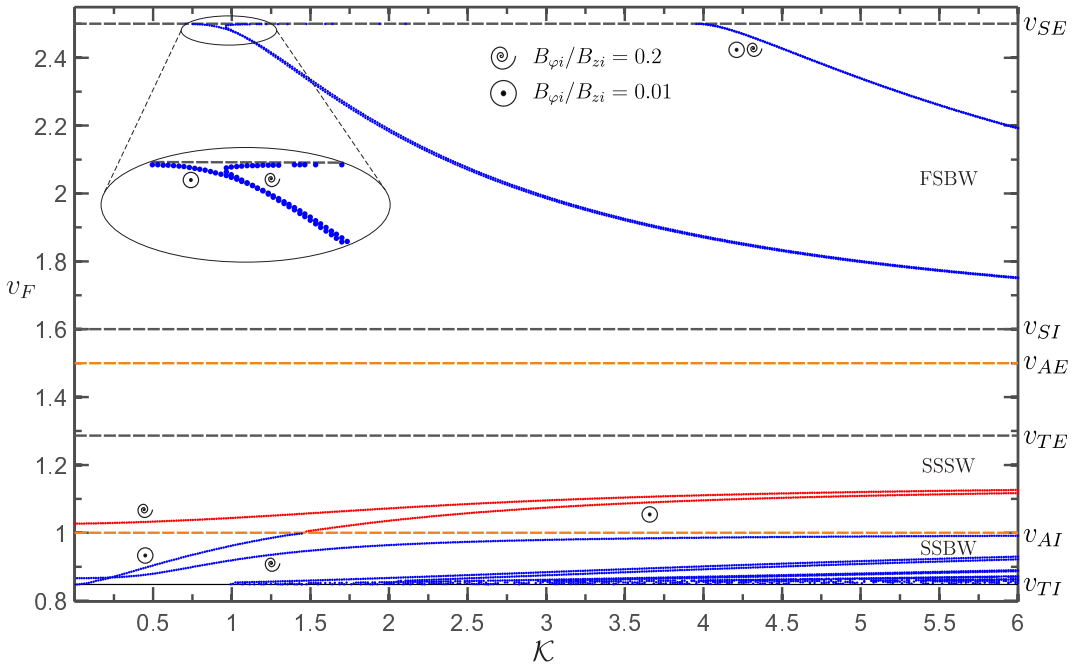

Figure 3.2: Solutions of the dispersion Equation (3.29) for a warm dense tube embedded in a dense environment ($\beta_i > 1, \beta_e > 1$) corresponding to a characteristic speed ordering $v_{SE} > v_{SI} > v_{AE} > v_{AI}$. The colour coding is as follows: blue indicates body waves, red corresponds to surface waves, orange corresponds to either the internal or external Alfvén speeds, note this convention is used consistently in this work. The circle with a dot corresponds to the case $B_{\varphi i}/B_{zi} = 0.01$ while the spiral corresponds to $B_{\varphi i}/B_{zi} = 0.2$. The mean root mean squared error (RMSE) for this speed ordering is 0.0328.

and without twist, and in extension it is very similar to the case with only internal twist studied by Erdélyi and Fedun (2007). It is worth noting that when internal and external twist is present, the different radial harmonics of the FSBW modes have two solutions, one dispersive and one approximately non-dispersive (see Figure 3.2). It is, however, unclear if the non-dispersive solution remains valid until the next radial harmonic. Nevertheless, it is clear that, in the neighbourhood of the v_{SE} *singularity* we obtain two solutions with comparable phase speeds (v_F) which opens the possibility for beat phenomena and thus widens the possibility of detection of these waves since the beat frequency will be smaller than both waves that produce it. This behaviour is not present when we consider twist only inside the flux tube. Otherwise, the overall behaviour of the solutions is virtually identical to those determined by Erdélyi and Fedun (2007).

In Figure 3.3 we present the solutions for the second case in Table 3.1. This scenario can occur when the internal plasma-β is very low, $\beta_i \ll 1$, while the external plasma-β is high, $\beta_e \gg 1$. At this point we would like to stress the fact that for a specific set of characteristic speeds the internal and external plasma-β values are uniquely defined (see Appendix A.3). We focus here only in the region of solutions in (v_{AE}, v_{SE}) since the infinite number of the slow sausage body waves (SSBW), present in the (v_{TI}, v_{SI}) interval are minimally affected by the twist and thus are almost identical when compared with the corresponding case with no twist. We plot solutions for $B_{\varphi i}/B_{zi} = \{0.01, 0.05, 0.1, 0.15, 0.175, 0.2\}$. The upper plot in Figure 3.3 represents the solutions only for internal twist. A feature for this set of solutions is that the FSBW which is transformed to the fast sausage surface (FSSW) for $\mathcal{K} \sim 2.7$, for increasing twist the transition becomes discontinuous and an interval, in $\mathcal{K}$, is created where there exist no solutions. For example, for $B_{\varphi i}/B_{zi} = 0.05$, this interval extends for $\mathcal{K} = (2.4, 3.1)$ where no fast body waves exist. This interval becomes larger with increasing twist. However, this is not the case in the presence of external twist, see lower figure in Figure 3.3. The FSBW and FSSW appear to behave similarly, however, in all cases except for $B_{\varphi i}/B_{zi} = 0.01$ there is a surface wave solution that is nearly non-dispersive for a wide range of $\mathcal{K}$. Another feature is the s-like set of surface wave solutions that are clearly visible for $B_{\varphi i}/B_{zi} = 0.175$ and $B_{\varphi i}/B_{zi} = 0.2$. Note, that this s-like set is also present for the other cases however the cusp is encountered for larger values of $\mathcal{K}$. This structure is quite interesting since in some interval of $\mathcal{K}$ there

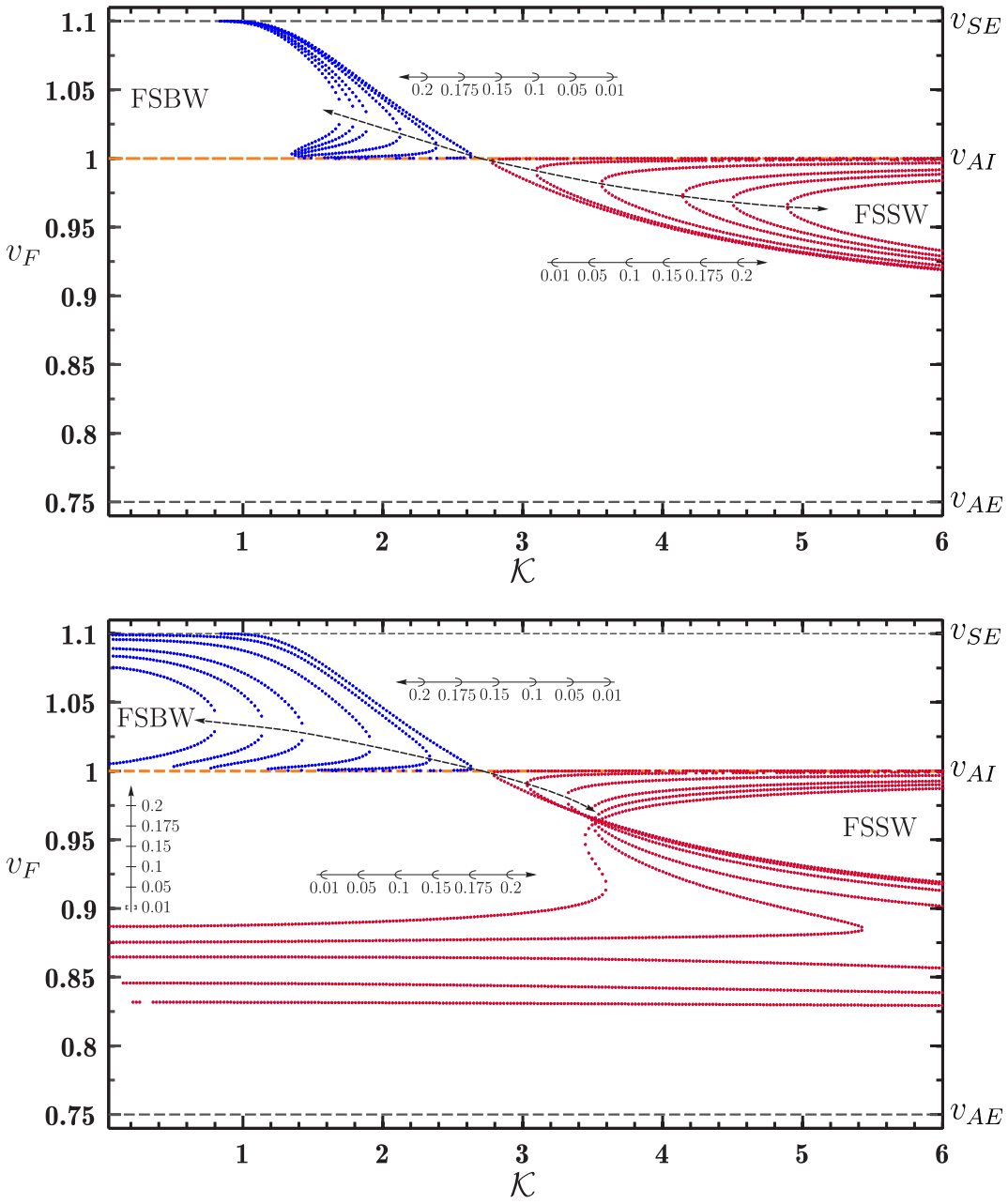

Figure 3.3: Solutions of the dispersion Equation (3.29) for a cool evacuated tube embedded in a dense environment ($\beta_i \ll 1, \beta_e \gg 1$) with speed ordering $v_{SE} > v_{AI} > v_{AE} > v_{SI}$. The top figure corresponds to no external twist for $r > r_a$, namely $S_e = 0$, while in the lower plot there is twist outside as well as inside the flux tube. Note that in both figures the solutions for $B_{\varphi i}/B_{zi} = \{0.01, 0.05, 0.1, 0.15, 0.175, 0.2\}$ have been over-plotted to conserve space and illustrate the effect of increasing the magnetic twist. The axes inside the figures match the progression of twist for the specific regions, for instance, in the top plot the axis with the arrow to the left indicates that the first FSBW from the right corresponds to magnetic twist of 0.01 the second to 0.05 etc. Note that the vertical axis, for $B_{\varphi i}/B_{zi} = 0.01$ has no non-dispersive FSSW (horizontal solutions marked in red) which is indicated by the empty parenthesis near the value 0.01. The mean RMSE is 0.021.

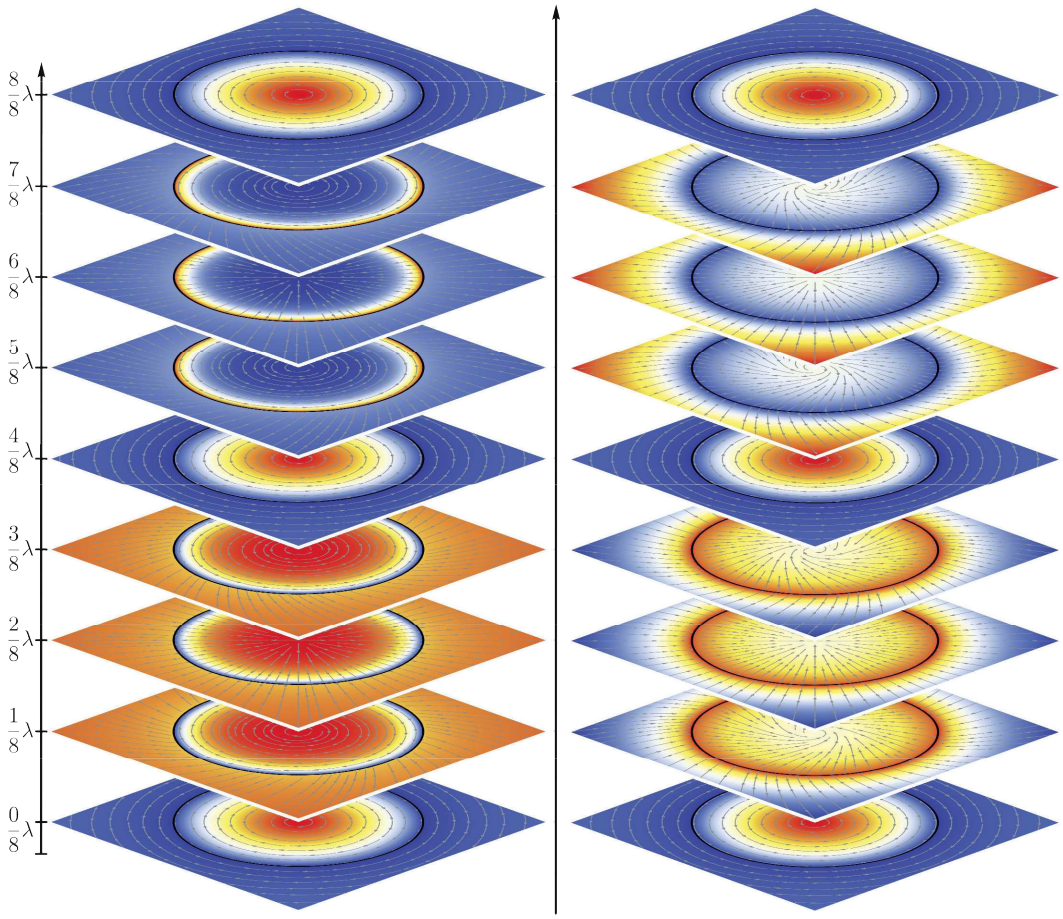

Figure 3.4: Plots of density perturbations superimposed on the background equilibrium density plots for the fast body and surface modes shown in Figure 3.3. The grey lines represent velocity perturbation streamlines on the xy-plane. Notice that for visualization purposes the streamlines contain no information on the magnitude of the perturbation, only direction information is conveyed. In the density plots red and blue correspond to high and low density respectively. The slices are snapshots at $t = 0$ at different positions for the wavelength λ of the oscillation. Note that this does not imply that the wavelength of the two oscillations is the same, rather, it is a fraction of the corresponding wavelength. (**Left**) Fast body mode for with magnetic twist for $\mathcal{K} = 0.3624$ and $v_F = 1.071$. (**Right**) Fast surface mode with magnetic twist for $\mathcal{K} = 3.494$ and $v_F = 0.9058$. Notice that in both cases the azimuthal component of the velocity perturbation at $0/8\lambda, 4/8\lambda$ and $8/8\lambda$ is non-zero.

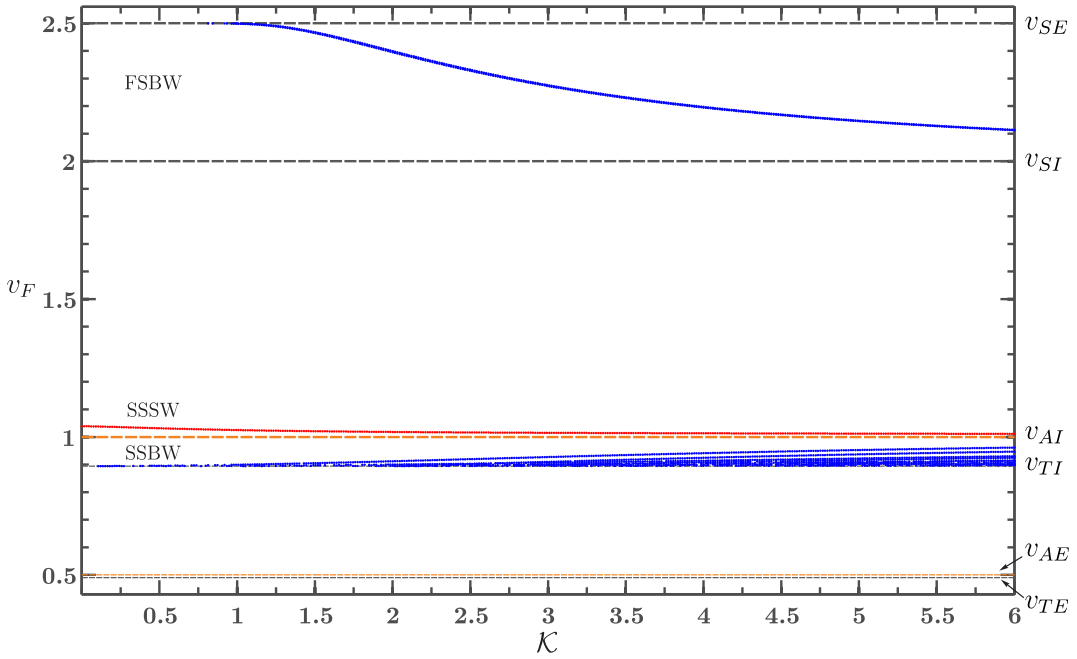

Figure 3.5: Solutions of the dispersion Equation (3.29) for a weak cool tube embedded in a dense environment ($\beta_i > 1, \beta_e \gg 1$) with speed ordering $v_{SE} > v_{SI} > v_{AI} > v_{AE}$. The mean RMSE is 0.0547.

exist 3 simultaneous solutions while outside of this interval exists only one. This means that within that interval, for a broadband excitation, the power of the driver will be distributed to more than one solution thus reducing the individual power spectrum signatures of the individual waves. In essence this will result in a interval of solutions that are much more difficult to detect. Another interesting point in respect to this s-like set of solutions is that it seems that a point may exist, for a certain value of $B_{\varphi i}/B_{zi}$ and a single $\mathcal{K}$ that there would be a continuum as the s-shape becomes vertical (see Figure 3.3). However, the existence or physical significance of this point is speculative since it does not appear to exist for small twist, namely the regime for which our approximation is valid. In Figure 3.4 we illustrate a FSBW (left panel) and a SSBW (right panel). In contrast to the kink mode in magnetic flux tubes with weak twist that exhibit a polarization (Terradas and Goossens, 2012), the sausage mode appears to be a superposition of an Alfvénic wave and a sausage wave leading by $\pi/2$.

The last plasma regime with high plasma-β considered in this work assumes that the characteristic speeds are ordered as: $v_{SE} > v_{SI} > v_{AI} > v_{AE}$. In Figure 3.5 we plot the solutions to Equation (3.29) for this case. The most notable feature, which seems to

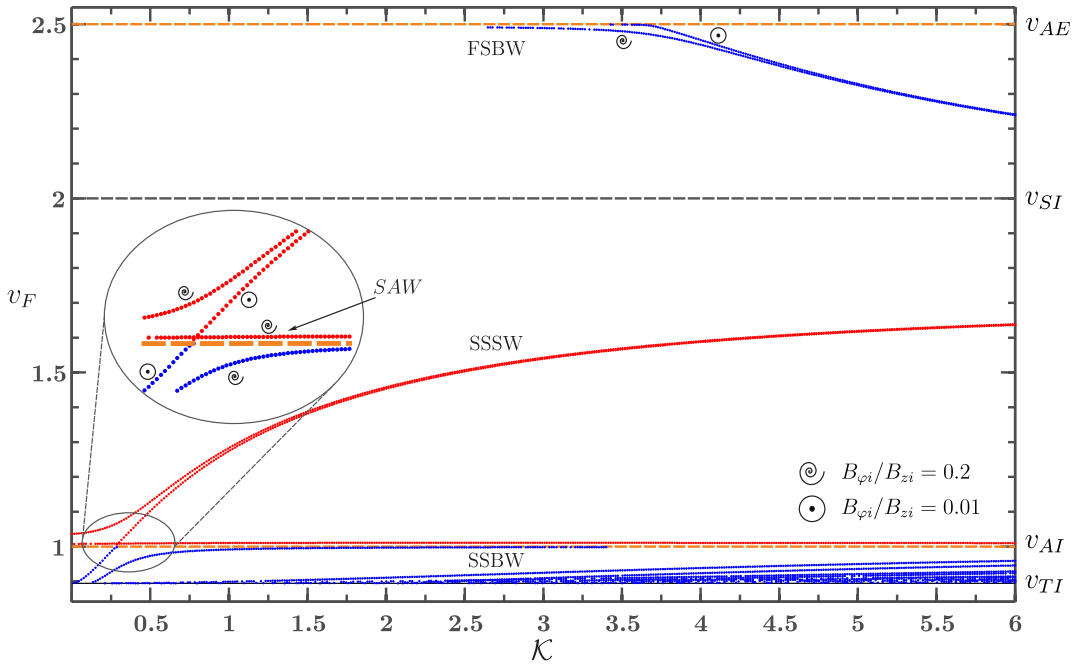

Figure 3.6: Solutions of the dispersion Equation (3.29) for an intense warm tube embedded in a rarefied environment ($\beta_i \ll 1, \beta_e \ll 1$) with the following speed ordering, $v_{AE} > v_{SI} > v_{AI} > v_{SE}$. The mean RMSE is 0.0291.

be consistent for alternative parameter sets corresponding to photospheric conditions, is that the magnetic twist appears to have only a small effect on the solutions to the dispersion equation. For example, we have also used: $v_{AI} > v_{SE} > v_{SI} > v_{AE}$ and there too (plot not shown as it is identical to the case with no twist) the deviation of the normalised phase speed was on the order of 0.5% or less for magnetic twist up to $B_{\varphi i}/B_{zi} = 0.2$.

3.4.2 Low plasma-β regime

In consultation with the results presented by Vernazza et al. (1981) and Gary (2001), we expect the results presented in this section to be most relevant to conditions that are typical of the upper chromosphere, the transition region, and corona. The remaining two cases that we consider in this work are for low plasma-β conditions (see Table 3.1).

In Figure 3.6 we consider an intense warm flux tube for which the characteristic speeds ordering is: $v_{AE} > v_{SI} > v_{AI} > v_{SE}$. This case was also considered by Erdélyi and Fedun (2007) under the assumption that there is only internal magnetic twist and zero twist in the environment surrounding the flux tube. In that work the influence of twist was under 1%, however, when the external twist is also considered,

interesting behaviour emerges. In this case, when there is zero twist, the first SSBW changes character to a slow sausage surface wave (SSSW) crossing v_{AI} at approximately $\mathcal{K} = 0.25$. When a small twist is introduced the first radial harmonic of the SSBW modes now becomes bounded by v_{AI} and a SSSW mode appears. A non-dispersive solution with a character similar to a surface wave emerges that closely follows v_{AI}. We have named this solution as surface-Alfvén wave (SAW) in Figure 3.6 and we have expanded the plot to make it visible since it is extremely close to the internal Alfvén speed. Interestingly the higher radial harmonics of the SSBW appear to be minimally affected when the magnetic twist is increased. The correction to the phase velocity for the FSBW with magnetic twist appears to be small compared with the case of no magnetic twist. For the first radial harmonic this correction is of the order of 0.4% while the correction is less than 0.1% for higher radial harmonics. However, this does not mean that the FSBW for the case with magnetic twist is identical to the case without twist as the azimuthal component of the velocity perturbation in the former case is non-zero altering the character of these waves significantly as compared with its counterpart in the case without magnetic twist.

Lastly we consider an intense cool tube, i.e. $v_{AE} > v_{AI} > v_{SE} > v_{SI}$, which corresponds to typical conditions in the solar corona. The solutions to the dispersion equation (i.e. Equation (3.29)) are shown in Figure 3.7. In this case, magnetic twist has more pronounced effect on the FSBWs, while the SSBW are virtually unaffected. In the long wavelength limit, $\mathcal{K} \ll 1$, the FSBWs become non-dispersive while for short wavelength limit, $\mathcal{K} \gg 1$, the solutions are identical to the case of a straight magnetic flux tube with vertical magnetic field only. It is important to note that, although the effect of magnetic twist appears to be subtle in this case, it has an significant difference compared with the case with no magnetic twist, e.g. Edwin and Roberts (1983), as well as the case considering only internal magnetic twist, e.g. Erdélyi and Fedun (2007). In both of these cases the sausage mode becomes leaky as $\mathcal{K} \to 0$. This however, is not the case when both internal and external twist are considered. Instead, as the magnetic twist increases so does the cut-off of the trapped fast sausage waves toward longer wavelengths. For example, for the particular characteristic speeds ordering considered in Figure 3.7, the first FSBW ceases to have a cut-off wavelength when $B_{\varphi i}/B_{zi} > 0.05$, approximately. Therefore, the FSBW for a twisted magnetic cylinder above a certain

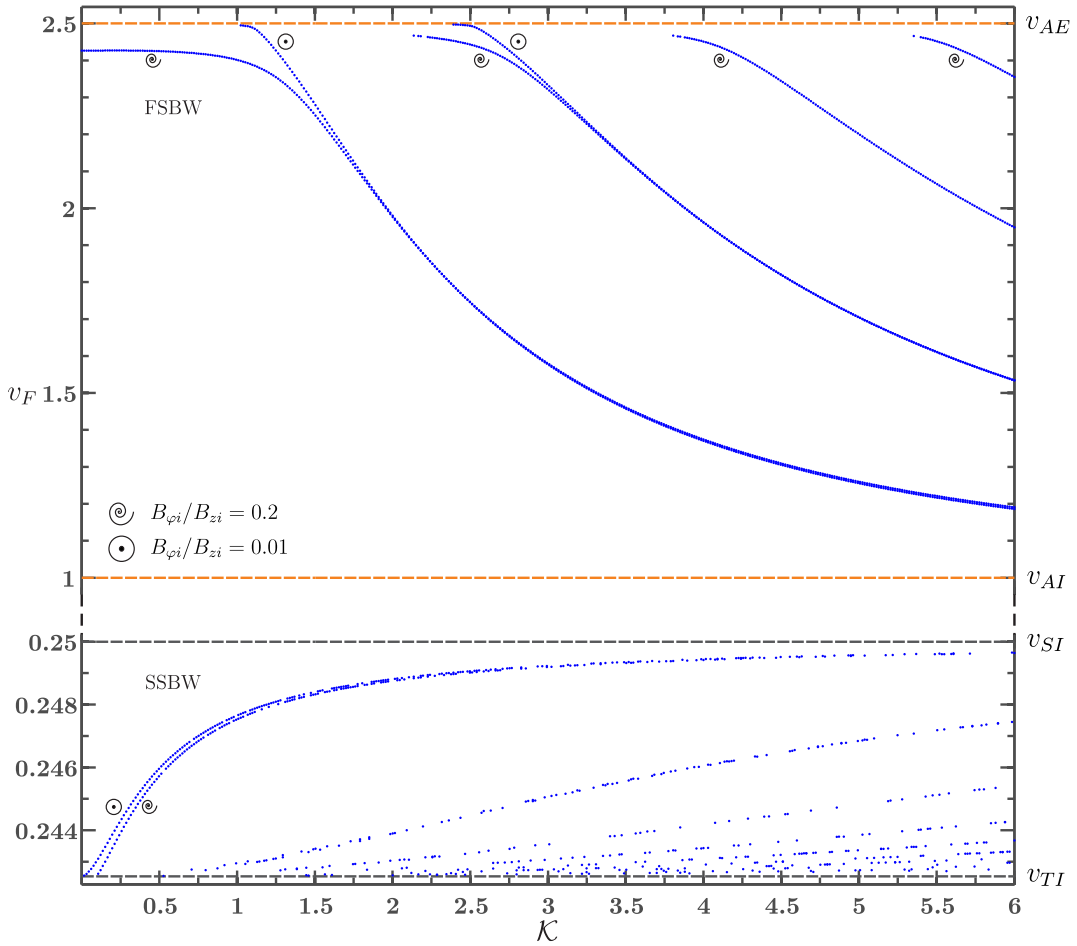

Figure 3.7: Solutions of the dispersion equation Equation (3.29) for an intense cool tube embedded in a rarefied environment ($\beta_i \ll 1, \beta_e \ll 1$) with speed ordering $v_{AE} > v_{AI} > v_{SE} > v_{SI}$. The mean RMSE is 0.0175.

threshold remains trapped for all wavelengths. A consequence of this is that FSBWs remain in the Alfvén continuum and therefore may be resonantly damped, see for example Sakurai et al. (1991a). This means that the sausage mode cannot be ruled out as a source of energy to the corona.

3.5 Discussion

Although the model we present in this work for a magnetic flux tube with internal and external twist is relatively advanced in comparison to recent theoretical models, it contains a number of simplifications and therefore we would be remiss not to discuss the potential caveats when used to interpret observations. Observations suggest that the cross-section of magnetic flux tubes is not circular. Although there are no theoretical studies of magnetic flux tubes with completely irregular cross-section, some steps towards this direction have been taken by considering flux tubes with elliptical cross-section, see for example Ruderman (2003) and Erdélyi and Morton (2009). The results for the sausage mode presented by Erdélyi and Morton (2009) show that, in comparison with the model of Edwin and Roberts (1983), i.e. circular cross-section, the ellipticity of the cross-section tends to increase the phase speed of the sausage mode for photospheric conditions by approximately 5% in the short wavelength limit, and, is negligible in the long wavelength limit. Conversely, in coronal conditions for increasing ellipticity the phase speed increase is more pronounced for a wide range of wavelengths and is shown to be as much as 20% higher of the predicted phase speed by the model with circular cross-section. This effect is quite important since, for sufficiently large ellipticity, it could counteract the effect that magnetic twist has on the cut-off frequency for the fast sausage body modes seen in Figure 3.7. Namely, as can be seen in Figure 3.7, the fast sausage mode remains trapped in the long wavelength limit, however, should the phase speed be increased, then a cut-off frequency for the fast sausage body modes may be reinstated.

Furthermore, although we have studied propagating waves in this work, the study of standing modes for $k_\varphi = 0$ is trivially extended. Namely, if the magnetic flux tube is line-tied on both foot-points, the longitudinal wavevector will be quantised according to $k_z = n\pi/L$, where n is an integer and L is the length of the magnetic flux tube. If the flux tube is assumed to be line-tied on one end and open on the other, then no

quantization takes place and there can be propagating and standing waves for all k_z. Here it should be mentioned that the effect of the magnetic flux tube curvature is of the order of $(r_a/L)^2$ and therefore has a small effect on the eigenfrequencies of magnetic flux tubes in the solar atmosphere (Van Doorsselaere et al., 2004, 2009).

Other effects that can alter the eigenfrequencies predicted using the model in this work are, density stratification, flux tube expansion and resonance phenomena due to neighbouring magnetic flux tubes, see Ruderman and Erdélyi (2009) for a more in depth discussion. Of course, more complicated magnetic field topologies can have other unforeseen effects. This can be seen in magneto-convection simulations, e.g. Wedemeyer-Böhm et al. (2012), Shelyag et al. (2013), Trampedach et al. (2014) as well as in simulations with predefined background magnetic fields, see Bogdan et al. (2003), Vigeesh et al. (2012), Fedun et al. (2011). However, the interpretation of the results from such simulations is a major challenge which is only increased by considering that the initial conditions, which are mostly unknown, play a very important role in their subsequent evolution.

3.6 Summary

In the presence of weak twist the sausage mode has mixed properties since it is unavoidably coupled to the axisymmetric Alfvén wave. This is apparent from the solutions (see for example Appendix A.4) where the azimuthal velocity perturbation component is non-zero and is also supported by the results presented in Section 3.2.1. The implications of this on the character of surface and body waves are seen clearly in Figure 3.4, where the relative magnitude of the radial and azimuthal components of the velocity perturbation alternate periodically and waves tend to exhibit Alfvénic character the closer their phase velocity is to one of the Alfvén speeds. The reason for this behaviour has been explained in Section 3.2.1.

In this chapter the effect of internal and external magnetic twist on a straight flux tube for the sausage mode was analytically investigated. We have shown that magnetic twist naturally couples axisymmetric Alfvén waves with sausage waves. Some of the main results of this coupling are:

- Sausage waves can exhibit Doppler signatures similar to these expected to be

observed for Alfvén waves.

- The phase difference between the radial and torsional velocity perturbations is $\pi/2$, which means that both effects can be simultaneously observed.
- Excitation of axisymmetric modes in twisted magnetic flux tubes can be accomplished by a larger variety of drivers compared to the *pure* sausage and axisymmetric Alfvén waves. Therefore, we speculate that these waves should be more likely to be observed compared with their decoupled counterparts.
- For coronal conditions the fast sausage body waves remain trapped for all wavelengths when the magnetic twist strength surpasses a certain threshold. This appears to be characteristic of magnetic twist and could potentially be used to identify the strength of the magnetic twist.

These findings suggest that axisymmetric modes with magnetic twist can be easily mistaken for pure Alfvén waves.

Chapter 4

Resonant Absorption of Axisymmetric Modes

Given the mounting evidence taht magnetic twist and axisymmetric MHD modes are ubiquitous in the solar atmosphere, the study of resonant absorption for these modes is a pressing issue as it can have important consequences for heating the solar atmosphere and the observed wave damping in waveguides. In this chapter, for the first time, the damping rate for axisymmetric MHD waves is calculated in weakly twisted magnetic flux tubes. The aim is to investigate the impact of resonant damping on these modes for solar atmospheric conditions. This analytical study is based on an idealised configuration of a straight magnetic flux tube with a weak magnetic twist inside as well as outside the tube. By implementing the conservation laws derived by Sakurai et al. (1991a), and the analytic solutions for weakly twisted flux tubes obtained in Chapter 3, a dispersion relation is derived for resonantly damped axisymmetric modes in the spectrum of the Alfvén continuum, and an insightful analytical expression for the damping rate in the long wavelength limit is calculated. Furthermore, it is shown that both the longitudinal magnetic field and the density, which are allowed to vary continuously in the inhomogeneous layer, have a significant impact on the damping time. Given the conditions in the solar atmosphere, resonantly damped axisymmetric modes are highly likely to be ubiquitous and play an important role in energy dissipation. It is also suggested that given the character of these waves, it is likely that they have already been observed in the guise of Alfvén waves.

4.1 Introduction

Inhomogeneities, such as a density variation across a magnetic flux tube, produce a continuous spectrum of eigenfrequencies. Consider for instance a straight magnetic flux tube of radius r_e and constant temperature, where the density varies smoothly from its center to its boundary, such that cylindrical surfaces have constant density. This means that also the sound and Alfvén speeds within every cylindrical surface are constant. These concentric cylindrical sheaths comprise the flux tube. Due to the difference in characteristic speeds, every surface will have its own eigenfrequency. This results in an infinite set of eigenfrequencies, a continuum. One of the consequences of this continuum in driven systems is resonant absorption, assuming the driving frequency is within the continuum.

Given that inhomogeneities are the rule rather than the exception in the solar atmosphere, resonant absorption is bound to occur there. This has long been recognised, from the first suggestion by Ionson (1978) to subsequent studies motivated by advances in solar observations, see for example the following studies by Poedts et al. (1989, 1990); Ruderman and Roberts (2002); Goossens et al. (2002); Andries et al. (2005); Goossens et al. (2009); Van Doorsselaere et al. (2009); Verth et al. (2010); Terradas et al. (2010); Antolin et al. (2015); Okamoto et al. (2015), to name but a few. In general, resonant absorption in magnetohydrodynamic (MHD) modes is important for the solar atmosphere. Resonant damping of Alfvén waves is a natural and efficient mechanism for energy dissipation of MHD waves in inhomogeneous plasmas (Ionson, 1978, 1985; Hollweg and Yang, 1988). It can also provide an explanation for the observed loss of power of acoustic modes in sunspots (Hollweg, 1988; Sakurai et al., 1991a,b; Goossens and Poedts, 1992; Keppens et al., 1994), and it has been shown that it is of importance in transverse oscillations (kink mode), see for example (Aschwanden et al., 1999; Nakariakov et al., 1999; Ruderman and Roberts, 2002; Goossens et al., 2002). Resonant Alfvén waves can be an energy conduit between photospheric motions at the footpoints of coronal loops (see for example De Groof and Goossens, 2000; De Groof et al., 2002; De Groof and Goossens, 2002), and, resonant dissipation plays an important role in the observed damped oscillations in prominences (see Terradas et al., 2008; Arregui et al., 2012). For an in depth review of resonant absorption in the solar atmo-

sphere see Goossens et al. (2011).

Since 1999, when the first post-flare standing mode transverse oscillations were detected using the Transition Region and Coronal Explorer (TRACE) (Aschwanden et al., 1999; Nakariakov et al., 1999) there has been a growth in studies of resonant absorption for the kink mode. Ruderman and Roberts (2002) derived relations describing the expected damping of kink waves in coronal loops using the long wavelength and pressure-less plasma[1] approximations, a result that was previously obtained by Goossens et al. (1992) using the connection formulae derived by Sakurai et al. (1991a,b) for the driven problem and by Tirry and Goossens (1996) for the eigenvalue problem. Later Goossens et al. (2002) and Aschwanden et al. (2003) used these results and calculated the expected damping times for a sequence of observed parameters for coronal flux tubes. Goossens et al. (2002) concluded that for the parameter sample used, resonant absorption can explain the observed damping times well, provided that the density contrast is allowed to vary from loop to loop. Another important result in this work is that the observed damping does not require modification of the order of magnitude estimates of the Reynolds number (10^{14}) as suggested by Nakariakov et al. (1999). Aschwanden et al. (2003) also arrived at the conclusion that, on average, the theoretical predictions of the damping rate derived by Goossens et al. (1992) and Ruderman and Roberts (2002), are consistent with observations and suggested that damping times of coronal loops can be used to infer their density contrast with the surrounding plasma. Coronal flux tubes tend to deform in their *middle* section due to buoyancy, effectively resulting in cross-sections that are approximately elliptical. Ruderman (2003) studied the damping of the kink mode in flux tubes with an elliptical cross-section and found that for moderate ratios of the minor to major semi-axis the difference of the damping rate for resonant absorption compared with flux tubes with circular cross-section is not very large. Another deviation from the ideal straight magnetic flux tube is axial curvature. Van Doorsselaere et al. (2004) studied the effect of this curvature and also found that the longitudinal curvature of flux tubes does not significantly alter the damping time of kink modes. Progressively the theoretical models for kink oscillations have become more elaborate, for example, Andries et al. (2005) considered longitudinal density stratification. Methods for kink wave excitation have

[1] Also referred to as *cold* plasma approximation.

been studied, see for example Terradas (2009). The increased body of observations of kink waves allowed Verwichte et al. (2013) to perform a statistical study to constrain the free parameters present in theoretical models of resonant absorption in kink modes.

In contrast to this avalanche of theoretical and observational advances related to the kink mode, resonant absorption for axisymmetric modes has not received much attention. One reason for this is that it was believed that the sausage mode had a long wavelength cutoff (e.g. Edwin and Roberts, 1983) which suggested that observation of the sausage mode would be challenging. Furthermore, it was correctly believed that for a straight magnetic field, axisymmetric modes could not be resonantly damped. However, it is apparent, even in early works in resonant absorption (see for example Sakurai et al., 1991a,b; Goossens et al., 1992), that for weakly twisted magnetic field axisymmetric modes can and are resonantly damped. What was not known until recently, however, was that the long wavelength cutoff for these modes is also removed in the presence of weak magnetic twist, see Chapter 3. Therefore, these modes can freely propagate for all wavelengths, and so, at least in principle, these modes should be observable. Additionally, recent studies suggest that magnetic twist and axisymmetric modes are ubiquitous throughout the solar atmosphere, a view that is reinforced by the results of Chapter 3. Therefore, the study of these modes has become quite relevant and important. Some examples of magnetic twist in the solar atmosphere are, flux tubes emerging from the convection zone (see for example Hood et al., 2009; Luoni et al., 2011), sunspot rotation can result in twisted magnetic fields (Brown et al., 2003; Yan and Qu, 2007; Kazachenko et al., 2009), spicules are observed to have twist (De Pontieu et al., 2012; Sekse et al., 2013), as well as solar tornadoes (Wedemeyer-Böhm et al., 2012). Lastly observations of axisymmetric modes have been recently reported by Morton et al. (2012) and Grant et al. (2015).

The present chapter focuses on the resonant absorption of axisymmetric MHD modes in weakly twisted magnetic flux tubes. Axisymmetric modes correspond to modes with azimuthal wavenumber $k_\varphi = 0$. First, the results of Chapter 3 are revisted. In that chapter the longitudinal component of the magnetic field, and the density were discontinuous across the flux tube boundary. This choice was intentional as it avoids the MHD continua and simplifies the analysis. However, this simplifications also left out relevant physics. Having as a starting point the setup in Chapter 3 an intermediate

layer is introduced in the neighbourhood of the flux tube boundary. Within this layer, the magnetic field and density are allowed to vary smoothly, resulting in an overall continuous profile for the longitudinal magnetic field and density. This, in turn, allows for the existence of the slow and Alfvén continua. Next, we assume that the layer that connects the internal and external quantities, is thin, namely $\ell \ll r_e$ where ℓ is the width of the layer. Using the conservation laws, and the resulting jump conditions for the Alfvén continuum by Sakurai et al. (1991a), the resulting complex dispersion relation is derived. This dispersion relation is then solved numerically. Lastly, to better understand the predicted damping times, the long wavelength limit approximation is applied to the resulting complex dispersion relation. These simpler relations allow the comparison of these results with the expected damping for the kink mode predicted using the results by Goossens et al. (1992) and Ruderman and Roberts (2002). This chapter is concluded with a statistical analysis of the resulting approximations to further understand the necessary conditions for the observation of resonantly damped axisymmetric modes. The main contributions of this chapter can be summarised as follows:

- For the first time, a dispersion relation is uncovered for axisymmetric modes in magnetic flux tubes with internal and external twist, including the resonance with the Alfvén continuum and the simplified expressions for the frequency and damping time in the long wavelength limit, for which the axisymmetric modes are no longer leaky.

- Given that there are four parameters required for the evaluation of the aforementioned relation, namely density contrast, magnetic field contrast, thickness of the inhomogeneous layer and magnetic twist, a statistical framework is presented to infer what can be drawn from observations.

- The statistical framework shows that the predictions of the present theoretical model are in agreement with observed damping times.

Since Alfvén, or Alfvén like waves in the presence of magnetic twist, have the potential to be long range and thus observable, our focus is only on the Alfvén continuum.

This chapter is organised as follows: in Section 4.2 we introduce the model along with prior theoretical results required for the derivation of the dispersion relation lead-

ing to resonant absorption. In Section 4.3, using the jump conditions derived by Sakurai et al. (1991a) we derive the dispersion equation for axisymmetric modes. This equation is then used in Section 4.4 to obtain an expression for the damping rate in the long wavelength limit and then in Section 4.5 the significance of the results in this work is investigated for the observation of axisymmetric modes in the solar atmosphere. Finally, in Section 4.6 the results of this chapter are summarised.

4.2 Model

Let us consider an idealised cylindrically symmetric magnetic flux tube in static equilibrium. We employ a cylindrical coordinate system (r, φ, z), with the z coordinate along the axis of symmetry of the flux tube. The linearised ideal MHD equations are,

$$\rho\frac{\partial^2\boldsymbol{\xi}}{\partial t^2} + \nabla p' + \frac{1}{\mu_0}\left[\boldsymbol{B}'\times(\nabla\times\boldsymbol{B}) + \boldsymbol{B}\times(\nabla\times\boldsymbol{B}')\right] = 0, \tag{4.1a}$$

$$p' + \boldsymbol{\xi}\cdot\nabla p + \gamma p\nabla\cdot\boldsymbol{\xi} = 0, \tag{4.1b}$$

$$\boldsymbol{B}' + \nabla\times(\boldsymbol{B}\times\boldsymbol{\xi}) = 0, \tag{4.1c}$$

where ρ, p and $\boldsymbol{B}$ are the equilibrium density, plasma kinetic pressure and magnetic field, respectively, $\boldsymbol{\xi}$ is the Lagrangian displacement, p' and $\boldsymbol{B}'$ are the Eulerian variations of the pressure and magnetic field, γ is the ratio of specific heats (taken to be 5/3 in this work), and μ_0 is the permeability of free space. In what follows an index, i, indicates quantities inside the flux tube ($r < r_i$) while variables indexed by, e, refer to the environment outside the flux tube ($r > r_e$). The inhomogeneous layer has a width equal to $\ell = r_e - r_i$ and it is assumed that $\ell \ll r_e$. Note that in Chapter 3, r_a, was used to denote the tube radius, this is equivalent to r_e in this work. The model configuration is illustrated in Figure 4.1 when $B_{\varphi e} \propto 1/r$. The quantities ρ, p and $\boldsymbol{B}$ are assumed to have only an r-dependence, therefore, the following balance equation must be satisfied when $\ell = 0$,

$$\frac{d}{dr}\left(p + \frac{B_\varphi^2 + B_z^2}{2\mu_0}\right) = -\frac{B_\varphi^2}{\mu_0 r}. \tag{4.2}$$

The equilibrium magnetic field is taken to be $\boldsymbol{B} = (0, B_\varphi, B_z)$, with $B_{\varphi i} = Sr$, $B_{\varphi e} = r_e^{1+\kappa}S/r^\kappa$ and B_{zi}, B_{ze} constant. By substituting $B_{\varphi i}$ and $B_{\varphi e}$ into Equation (4.2) and

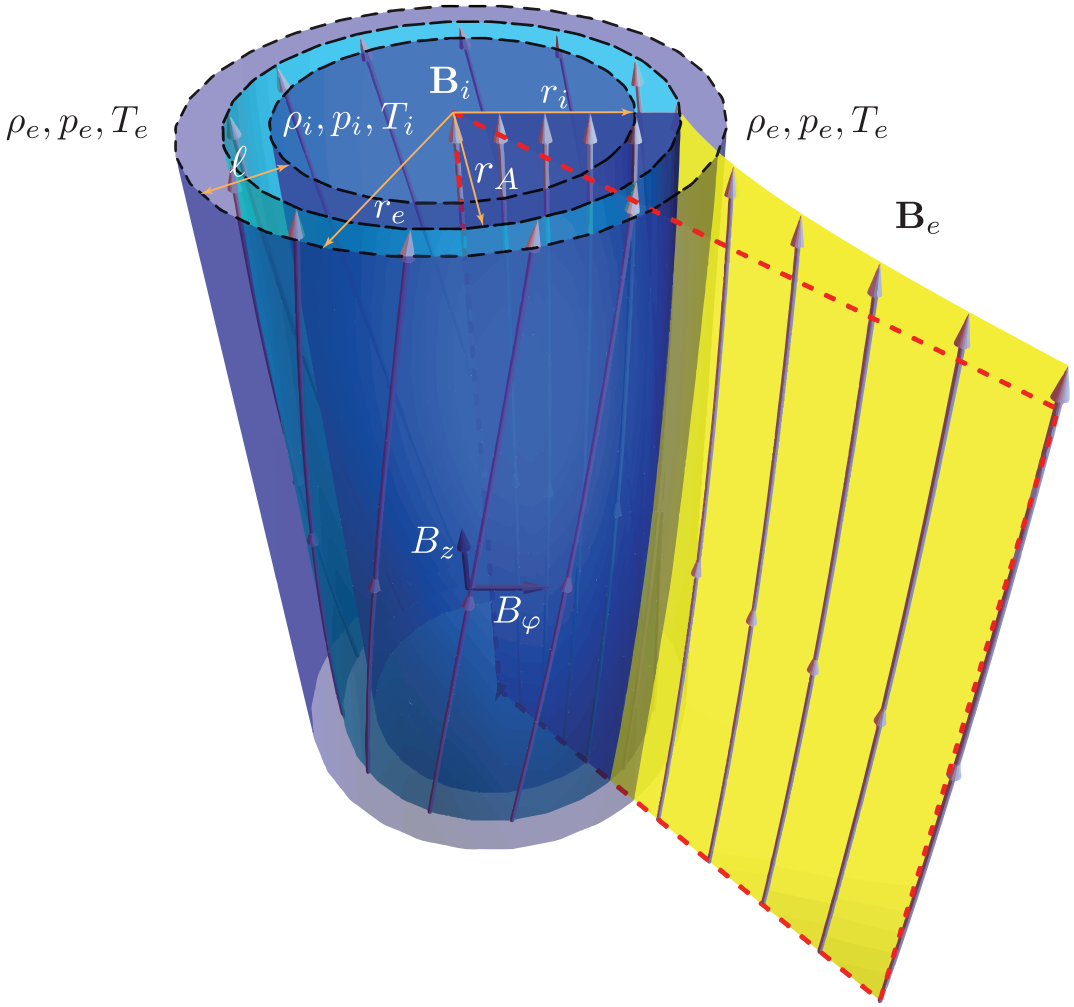

Figure 4.1: The model used in this chapter: a straight magnetic cylinder with variable twist inside ($r < r_i$) and outside ($r > r_e$) the tube. The region $r_i < r < r_e$ is the inhomogeneous layer, where the B_z component of the magnetic field and the density are varying continuously across this layer. The parameters ρ_i, p_i and T_i are the density, kinetic pressure and temperature at equilibrium inside the tube, i.e. for $r < r_i$. The corresponding quantities outside the tube ($r > r_e$) are denoted with a subscript e. The quantity r_A is the radius at the resonance. The dark blue surface emanating radially outwards inside the tube represents the influence of $B_\varphi \propto r$. The yellow surface outside the tube corresponds to $B_\varphi \propto 1/r$ dependence. The dashed red rectangle depicts a magnetic surface which would correspond to a magnetic field with only a longitudinal (z) magnetic field component. The inhomogeneous layer is bounded between r_i and r_e and is of width ℓ.

defining $B_{\varphi A} = B_\varphi(r_e) = Sr_e$, we obtain:

$$p(r) = \begin{cases} \dfrac{B_{\varphi A}^2}{\mu_0}\left(1 - \dfrac{r^2}{r_e^2}\right) + p_e & \text{for } r \leq r_e, \\ \dfrac{r_e^{2\kappa} B_{\varphi A}^2 (1-\kappa)}{2\mu_0 \kappa}\left(\dfrac{1}{r^{2\kappa}} - \dfrac{1}{r_e^{2\kappa}}\right) + p_e & \text{for } r > r_e, \end{cases} \tag{4.3}$$

where, p_e, is the pressure at the boundary of the magnetic flux tube and the parameter $\kappa \to 1$ corresponds to external twist proportional to $1/r$ while $\kappa \to 0$ to constant external twist. Note that although $p(r)$ is continuous, for solar atmospheric conditions and for weak magnetic twist ($\sup(B_\varphi^2/B_z^2) \ll 1$), its variation is much smaller than p_e and therefore can be assumed to be constant (Giagkiozis et al., 2015). However, in the model used in Chapter 3 the equilibrium density and the z component of the magnetic field are discontinuous, therefore the Alfvén continuum was avoided.

In the present chapter both the density and the magnetic field are continuous (see Figure 4.2) which introduces the slow and fast continua into our model. Specifically, the density is assumed to be a piecewise linear function of the form

$$\rho(r) = \begin{cases} \rho_i & \text{for } r < r_i, \\ \rho_i + \dfrac{r - r_i}{\ell}(\rho_e - \rho_i) & \text{for } r_i \leq r \leq r_e, \\ \rho_e & \text{for } r > r_e. \end{cases} \tag{4.4}$$

A similar form for the variation in the longitudinal component of the magnetic field is assumed, so,

$$B_z(r) = \begin{cases} B_{zi} & \text{for } r < r_i, \\ B_{zi} + \dfrac{r - r_i}{\ell}(B_{ze} - B_{zi}) & \text{for } r_i \leq r \leq r_e, \\ B_{ze} & \text{for } r > r_e. \end{cases} \tag{4.5}$$

Note that the assumption here is that $\ell \ll r_e$, so that pressure balance is maintained (see Equation (4.2)). Allowing both the density and the magnetic field to vary results in a non-monotonic variation in the Alfvén frequency across the inhomogeneous layer as seen in Figure 4.3.

The equilibrium quantities depend only on r and therefore the perturbed quantities can be Fourier analysed with respect to the φ and z coordinates, namely,

$$\boldsymbol{\xi}, p_T' \propto e^{i(k_\varphi \varphi + k_z z - \omega t)}. \tag{4.6}$$

Here, ω is the angular frequency, k_φ is the azimuthal wavenumber, k_z is the longitudinal wavenumber, and p_T' is the Eulerian total pressure perturbation defined as

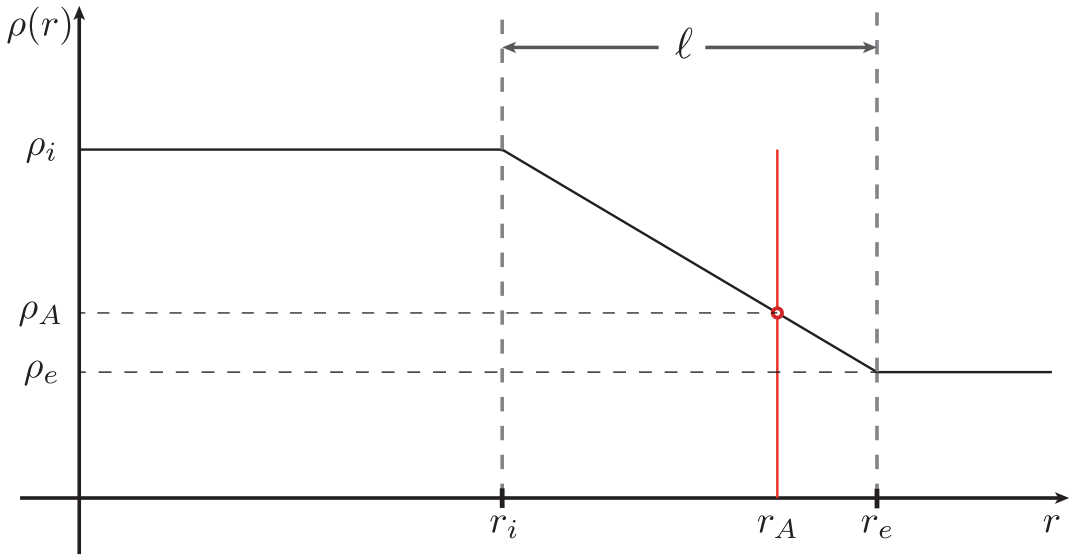

$$\rho_A = \rho_i + \frac{(\rho_e - \rho_i)}{\ell}(r_A - r_i)$$

Figure 4.2: Density profile as a function of r in the inhomogeneous layer of the magnetic flux tube. Here, r_i and r_e are the radius at which the inhomogeneous begins and ends respectively, r_e is the flux tube radius. The position $r = r_A$, is the radius at the resonance.

$p' + \boldsymbol{B}\boldsymbol{B}'/\mu_0$. Our focus is on axisymmetric modes (sausage waves) and therefore the azimuthal wavenumber is taken to be $k_\varphi = 0$. The Lagrangian displacement vector in flux coordinates is $\boldsymbol{\xi} = (\xi_r, \xi_\perp, \xi_\parallel)$ where,

$$\xi_\perp = \frac{B_z\xi_\varphi - B_\varphi\xi_z}{|\boldsymbol{B}|}, \qquad \xi_\parallel = \frac{B_\varphi\xi_\varphi + B_z\xi_z}{|\boldsymbol{B}|}, \tag{4.7}$$

assuming $B_r = 0$. Using Equation (4.6), Equation (4.1) can be transformed to the following two coupled first order differential equations,

$$D\frac{d(r\xi_r)}{dr} = C_1(r\xi_r) - rC_2p_T', \tag{4.8a}$$
$$D\frac{dp_T'}{dr} = \frac{1}{r}C_3(r\xi_r) - C_1p_T'. \tag{4.8b}$$
$$\rho(\omega^2 - \omega_A^2)\xi_\perp = \frac{\imath}{|\boldsymbol{B}|}C_A, \tag{4.8c}$$
$$\rho(\omega^2 - \omega_c^2)\xi_\parallel = \frac{\imath f_B}{|\boldsymbol{B}|}\frac{v_s^2}{v_s^2 + v_A^2}C_S, \tag{4.8d}$$
$$\nabla\cdot\boldsymbol{\xi} = -\frac{\omega^2 C_S}{\rho(v_s^2 + v_A^2)(\omega^2 - \omega_c^2)}, \tag{4.8e}$$

where,

$$D = \rho(\omega^2 - \omega_A^2)C_4, \tag{4.9a}$$
$$C_1 = \frac{2B_\varphi}{\mu_0 r}\left(\omega^4 B_\varphi - \frac{k_\varphi}{r}f_B C_4\right), \tag{4.9b}$$
$$C_2 = \omega^4 - \left(k_z^2 + \frac{k_\varphi^2}{r^2}\right)C_4, \tag{4.9c}$$
$$\begin{aligned} C_3 = {} & \rho D\left[\omega^2 - \omega_A^2 + \frac{2B_\varphi}{\mu_0\rho}\frac{d}{dr}\left(\frac{B_\varphi}{r}\right)\right] \\ & + 4\omega^4\frac{B_\varphi^4}{\mu_0^2 r^2} - \rho C_4\frac{4B_\varphi^2\omega_A^2}{\mu_0 r^2}, \end{aligned} \tag{4.9d}$$
$$C_4 = (v_s^2 + v_A^2)(\omega^2 - \omega_c^2), \tag{4.9e}$$
$$C_A = g_B p_T' - 2\frac{f_B B_\varphi B_z \xi_r}{\mu_0 r},\ C_S = p_T' - 2\frac{B_\varphi^2\xi_r}{\mu_0 r} \tag{4.9f}$$

and,

$$v_s^2 = \gamma\frac{p}{\rho}, \qquad v_A^2 = \frac{\boldsymbol{B}^2}{\mu_0\rho},$$
$$\omega_c^2 = \frac{v_s^2}{v_A^2 + v_s^2}\omega_A^2, \qquad \omega_A^2 = \frac{f_B^2}{\mu_0\rho},$$
$$f_B = \mathbf{k}\cdot\boldsymbol{B} = \frac{k_\varphi}{r}B_\varphi + k_z B_z, \qquad g_B = (\mathbf{k}\times\boldsymbol{B})_r = \frac{k_\varphi}{r}B_z - k_z B_\varphi.$$

Here, $\mathbf{k} = (0, k_\varphi/r, k_z)$ is the wavevector, C_A and C_S are the coupling functions, v_s is the sound speed, v_A is the Alfvén speed, ω_c is the cusp angular frequency and ω_A is the Alfvén angular frequency. Equation (4.8) was initially derived by Hain and Lust (1958) and later by Goedbloed (1971); Sakurai et al. (1991a). The first order coupled ODEs in Equation (4.8) can be reduced to a single second order ODE for ξ_r,

$$\frac{d}{dr}\left[\frac{D}{rC_2}\frac{d}{dr}(r\xi_r)\right] + \left[\frac{1}{D}\left(C_3 - \frac{C_1^2}{C_2}\right) - r\frac{d}{dr}\left(\frac{C_1}{rC_2}\right)\right]\xi_r = 0. \tag{4.10}$$

The assumption of axisymmetry ($k_\varphi = 0$) leads to,

$$f_B = k_z B_z, \qquad g_B = -k_z B_\varphi, \qquad C_A = -k_z B_\varphi\left(p_T' + 2\frac{B_z^2}{\mu_0 r}\xi_r\right). \tag{4.11}$$

Therefore the equations for the perpendicular and parallel components of displacement are given by,

$$\rho(\omega^2 - \omega_A^2)\xi_\perp = -\imath\frac{k_z B_\varphi}{|\boldsymbol{B}|}\left(p_T' + 2\frac{B_z^2}{\mu_0 r}\xi_r\right), \tag{4.12a}$$

$$\rho(\omega^2 - \omega_c^2)\xi_\parallel = \imath\frac{k_z B_z}{|\boldsymbol{B}|}\frac{v_s^2}{v_s^2 + v_A^2}\left(p_T' - 2\frac{B_\varphi^2}{\mu_0 r}\xi_r\right). \tag{4.12b}$$

Note that Equation (4.12) suggests that the solutions for the components of the Lagrangian displacement vector are coupled in the sense that elimination of one component, e.g. by setting it to be identical to zero, has direct implications to the remaining components. To see this, consider a solution for which $\xi_r = 0$. As a result, by Equation (4.10), p_T' must also be equal to zero and, as a consequence of Equation (4.12a) and Equation (4.12b), it follows immediately that $\xi_\perp$ and $\xi_\parallel$ must also be identically equal to zero. Setting $\xi_r = 0$ leads to the trivial solution. Alternatively, let us assume that $\xi_\perp = 0$. In this case, by Equation (4.12a), the following relation must hold,

$$p_T' = -2\frac{B_z^2}{\mu_0 r}\xi_r. \tag{4.13}$$

This in turn implies that,

$$\rho(\omega^2 - \omega_c^2)\xi_\parallel = -2\imath\frac{k_z B_z|\boldsymbol{B}|}{\mu_0 r}\frac{v_s^2}{v_s^2 + v_A^2}\xi_r, \tag{4.14}$$

which, in general, is non-zero. Now, if we assume $\xi_\parallel = 0$ then,

$$p_T' = 2\frac{B_\varphi^2}{\mu_0 r}\xi_r \tag{4.15}$$

which leads to,

$$\rho(\omega^2 - \omega_A^2)\xi_\perp = -2\imath\frac{k_z B_\varphi|\boldsymbol{B}|}{\mu_0 r}\xi_r. \tag{4.16}$$

In the case where $B_\varphi = 0$ then $\xi_\perp$ decouples from ξ_r and $\xi_\parallel$. At this point it is instructive to mention the interpretation of the three components of $\boldsymbol{\xi}$ in flux coordinates by Goossens et al. (2011). Goossens et al. (2011) suggest that $\xi_\perp$ is the dominant component for Alfvén waves and for low plasma-β the slow and fast magnetoacoustic waves $\xi_\parallel$ and ξ_r is the dominant component, respectively. A quick check, by setting $B_\varphi = 0$ in Equation (4.7), renders $\xi_\perp$ equivalent to ξ_φ. This illuminates the connection of $\xi_\perp$ with torsional Alfvén waves.

In Chapter 3 the Equation (4.10) was solved for weak internal and external magnetic twist, albeit with the density profile assumed piecewise constant. With the help of the conservation relations for the Alfvén continuum derived by Sakurai et al. (1991a), these solutions, which are valid for ideal MHD, can be used to produce a dispersion relation for MHD waves that undergo damping in the continuum. The solutions in Chapter 3 are reproduced here for convenience,

$$\xi_{ri}(s) = A_i \frac{s^{1/2}}{E^{1/4}} e^{-s/2} M(a, b; s)\,, \tag{4.17a}$$

$$p'_{Ti}(s) = A_i \frac{k_a D_i}{n_i^2 - k_z^2} e^{-s/2} \left[\frac{n_i + k_z}{k_z} s M(a, b; s) - 2M(a, b-1; s) \right], \tag{4.17b}$$

and,

$$\xi_{re}(r) = A_e K_\nu \left(k_{re} r\right), \tag{4.18a}$$

$$p'_{Te} = A_e \left(\frac{\mu_0(1-\nu)D_e - 2B_{\varphi A}^2 n_e^2}{\mu_0 r (k_z^2 - n_e^2)} K_\nu(k_{re} r) - \frac{D_e}{k_{re}} K_{\nu-1}(k_{re} r) \right). \tag{4.18b}$$

In the above equations $M(\cdot)$ is the Kummer function and $K(\cdot)$ is the modified Bessel function of the second kind (Abramowitz and Stegun, 2012). The solutions in Equation (4.17a) and Equation (4.17b) were initially derived by Erdélyi and Fedun (2007).

The parameters in Equation (4.17) and Equation (4.18) are,

$$a = 1 + \frac{k_{ri}^2}{4k_z^2 E^{1/2}}, \qquad b = 2, \tag{4.19}$$

$$k_a = k_z(1-\alpha^2)^{1/2}, \qquad \alpha^2 = \frac{4B_{\varphi A}^2\omega_{Ai}^2}{\mu_0 r_e^2 \rho_i(\omega^2-\omega_{Ai}^2)^2}, \tag{4.20}$$

$$s = k_a^2 E^{1/2} r^2, \qquad E = \frac{4B_{\varphi A}^4 n_i^2}{\mu_0^2 r_e^4 D_i^2 k_z^2 (1-\alpha^2)^2}, \tag{4.21}$$

$$k_r^2 = k_z^2\left(1-\frac{n^2}{k_z^2}\right), \qquad k_r^2 = \frac{(k_z^2 v_s^2-\omega^2)(k_z^2 v_A^2-\omega^2)}{(v_A^2+v_s^2)(k_z^2 v_T^2-\omega^2)}, \tag{4.22}$$

$$n^2 = k_z^2 \frac{\omega^4}{(\omega_s^2+\omega_A^2)(\omega^2-\omega_c^2)}, \qquad v_T^2 = \frac{v_A^2 v_s^2}{v_A^2+v_s^2}, \tag{4.23}$$

$$D_i = \rho_i(\omega^2-\omega_{Ai}^2), \qquad D_e = \rho_e(\omega^2-\omega_{Ae}^2). \tag{4.24}$$

and ν is,

$$\begin{aligned}\nu^2(\kappa;r) = 1 + 2\frac{r_e^{2\kappa}B_{\varphi A}^2}{\mu_0^2 D_e^2 r^{2\kappa}}\Bigg\{2\frac{r_e^{2\kappa}B_{\varphi A}^2 n_e^2 k_z^2}{r^{2\kappa}} + \mu_0\rho_e\left[\omega_{Ae}^2(n_e^2(3+\kappa)\right.\\ \left. - k_z^2(1-\kappa)) - (n_e^2+k_z^2)(1+\kappa)\omega^2\right]\Bigg\}.\end{aligned} \tag{4.25}$$

This function (Equation 4.25) in Chapter 3 is evaluated for $\kappa = 0$, resulting in an exact solution for constant twist outside the flux tube which is also a zero order approximation for the external solution when magnetic twist is proportional to $1/r$:

$$\begin{aligned}\nu^2(0;r) = 1 + 2\frac{B_{\varphi A}^2}{\mu_0^2 D_e^2}\left\{2B_{\varphi A}^2 n_e^2 k_z^2\right.\\ \left. + \mu_0\rho_e\left[\omega_{Ae}^2(3n_e^2-k_z^2) - \omega^2(n_e^2+k_z^2)\right]\right\}.\end{aligned} \tag{4.26}$$

Using $\nu = \nu(0;r)$, i.e. constant external magnetic twist, results in solutions, namely (4.18a) and (4.18b), that have approximately 5% root mean squared error when compared with the exact solution corresponding to $\nu = \nu(1;r)$, that corresponds to external magnetic twist $\sim 1/r$, for more details see Chapter 3.

Imposing continuity for the Lagrangian displacement in the radial direction and total pressure continuity across the flux tube,

$$\xi_{ri}|_{r=r_e} = \xi_{re}|_{r=r_e}, \tag{4.27a}$$

$$p'_{Ti} - \frac{B_{\varphi i}^2}{\mu_0 r}\xi_{ri}\bigg|_{r=r_e} = p'_{Te} - \frac{B_{\varphi e}^2}{\mu_0 r}\xi_{re}\bigg|_{r=r_e}, \tag{4.27b}$$

the following dispersion relation was derived,

$$\frac{r_e D_e}{k_{re}} \frac{K_{\nu-1}(k_{re} r_e)}{K_\nu(k_{re} r_e)} = \rho_i v_{A\varphi i}^2 \left[\frac{1}{k_{ri}^2}(n_i + k_z)^2 - \frac{1}{k_{re}^2}(n_e^2 + k_z^2) \right] + \frac{(1-\nu)D_e}{k_{re}^2} - 2\frac{D_i}{k_{ri}^2} \frac{M(a, b-1; s)}{M(a, b; s)}, \tag{4.28}$$

where $v_{A\varphi i}^2 = B_{\varphi A}^2/\mu_0\rho_i$ and $\omega_{A\varphi i}^2 = k_z^2 B_{\varphi A}^2/\mu_0\rho_i$.

4.2.1 Long Wavelength Limit

The long wavelength limit of Equation (4.28) is needed for the approximation of the location of the resonant point used in subsequent sections and is obtained as follows. Using results from Abramowitz and Stegun (2012) Equation (13.5.5) we have,

$$\lim_{\epsilon \to 0} \frac{M(a, b-1; s)}{M(a, b; s)} = 1. \tag{4.29}$$

Furthermore, rewriting $\nu^2(0; r)$ as,

$$\nu^2(0; r) = 1 + 2\frac{\rho_e B_{\varphi A}^2}{\mu_0 D_e^2} \left(\omega_{Ae}^2 \left(3\frac{n_e^2}{k_z^2} - 1 \right) - \omega^2 \left(\frac{n_e^2}{k_z^2} + 1 \right) \right) k_z^2 + 4\frac{B_{\varphi A}^4}{\mu_0^2 D_e^2} \frac{n_e^2}{k_z^2} k_z^4, \tag{4.30}$$

becomes apparent that $\nu = 1 + \mathcal{O}(\epsilon^2)$, where $\epsilon = r_e k_z$. Therefore, using Equation (9.6.8) and (9.6.9) in Abramowitz and Stegun (2012) we obtain that,

$$\lim_{\epsilon \to 0} \frac{K_0(k_{re} r_e)}{K_1(k_{re} r_e)} = 0. \tag{4.31}$$

Using Equations (4.29) and (4.31) in Equation (4.28) we have,

$$2(\omega^2 - \omega_{Ai}^2) = v_{A\varphi i}^2 \left[(n_i + k_z)^2 - \frac{k_{ri}^2}{k_{re}^2} \left(n_e^2 - k_z^2 \right) \right]. \tag{4.32}$$

Expanding the part in square brackets on the right hand side of this equation about $\epsilon = 0$ leads to,

$$(n_i + k_z)^2 - \frac{k_{ri}^2}{k_{re}^2} \left(n_e^2 - k_z^2 \right) = 2\frac{\omega}{(v_{Ai}^2 + v_{si}^2)^{1/2}} k_z + \mathcal{O}\left(\epsilon^2\right). \tag{4.33}$$

Using this approximation in Equation (4.32), the positive solution of the dispersion relation (Equation 4.28) in the long wavelength limit to first order is,

$$\omega = \frac{1}{2} \left[\frac{\omega_{A\varphi i}^2}{(\omega_{Ai}^2 + \omega_{si}^2)^{1/2}} + \left(\frac{\omega_{A\varphi i}^4}{\omega_{Ai}^2 + \omega_{si}^2} + 4\omega_{Ai}^2 \right)^{1/2} \right]. \tag{4.34}$$

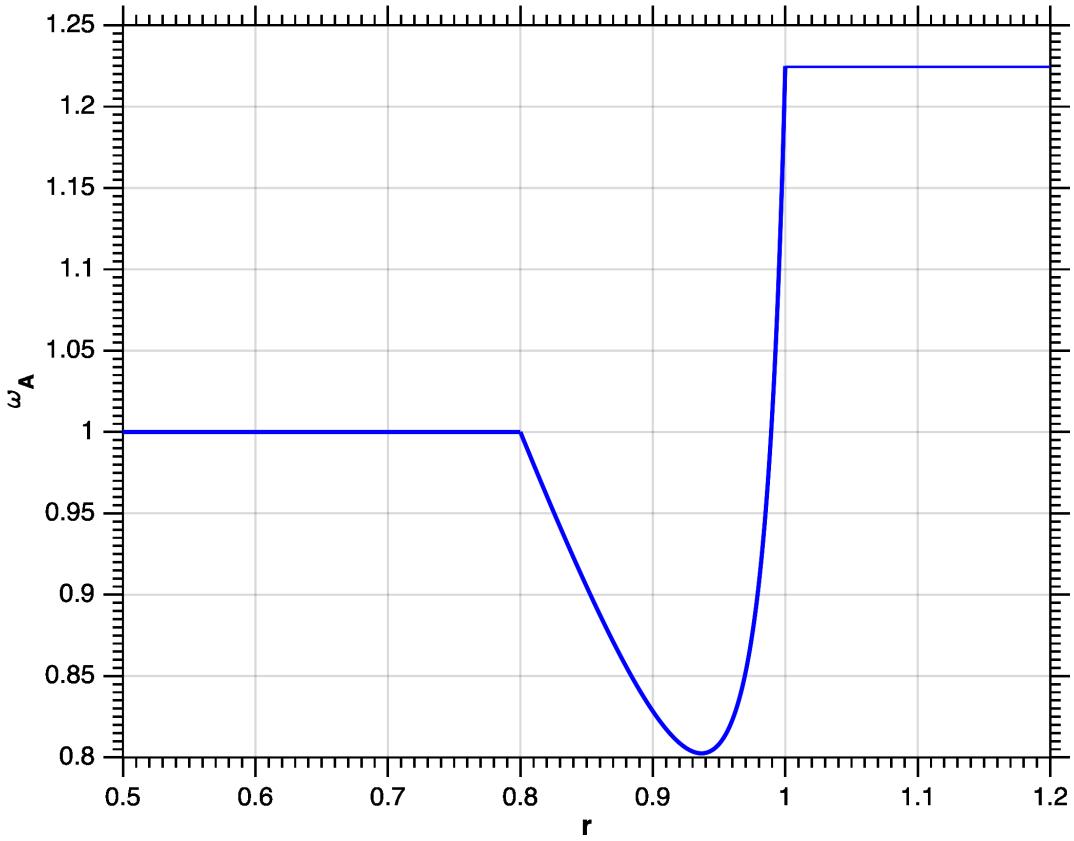

Figure 4.3: An example of Alfvén frequency variation across the resonant layer when $B_z = B_z(r)$ and $\rho = \rho(r)$, for $\chi = \rho_e/\rho_i = 0.1$, $\zeta = B_{ze}/B_{zi} = 0.35$ and $\ell/r_e = 0.2$. Here $r = 1$ is the tube boundary and ω_A is the normalised Alfvén frequency, the normalisation is with respect to the internal Alfvén frequency, ω_{Ai}.

For notational convenience Equation (4.34) can be rewritten as

$$\omega = \omega_{Ai} h, \tag{4.35}$$

$$h = \frac{1}{2}\left[\frac{q_i^2}{(1+d^2)^{1/2}} + \left(4 + \frac{q_i^4}{1+d^2}\right)^{1/2}\right] \tag{4.36}$$

where, $q_i = B_{\varphi A}/B_{zi}$ and $d = v_{si}/v_{Ai}$. This ω is used as an approximation to the resonance frequency, ω_0, in Section 4.4. Lastly, we should note that given this value for ω_0, although the variation of the Alfvén speed across the inhomogeneity in the flux tube is quadratic (see Figure 4.3), since $\omega_{Ai} < \omega_0 < \omega_{Ae}$, there will only be a single resonance point.

4.3 Alfvén Continuum

For an equilibrium with magnetic twist, such as the model used in this work, the total pressure perturbation is no longer a conserved quantity and therefore Equation (4.27a) and Equation (4.27b) require modification. Sakurai et al. (1991a) derived new conserved quantities for the Alfvén and slow continua. Specifically for the Alfvén continuum the conserved quantity is,

$$C_A = g_B p_T' - 2 f_B B_\varphi B_z \frac{\xi_r}{\mu_0 r}. \tag{4.37}$$

Using this conserved quantity they derived *jump conditions* for ξ_r and p_T', namely a prescription on how the radial component of the Lagrangian displacement and the total pressure perturbation can vary across the inhomogeneous layer connecting the internal with the external solutions. This prescription then implies, that the following conditions must be satisfied,

$$\xi_{ri}(r)|_{r=r_i} + [\![\xi_r(r)]\!] = \xi_{re}(r)|_{r=r_e} \tag{4.38}$$

and

$$p_{Ti}'(r)\big|_{r=r_i} + [\![p_T'(r)]\!] = p_{Te}'(r)\big|_{r=r_e}, \tag{4.39}$$

where $[\![\xi_r]\!]$ and $[\![p_T']\!]$ are the jump conditions across the resonant layer in the inhomogeneous section of the flux tube, in the radial displacement and total pressure perturbation (Sakurai et al., 1991a). The jump conditions are given by

$$[\![\xi_r]\!] = -\frac{\imath\pi}{|\Delta_A|}\frac{g_B}{\mu_0\rho^2 v_A^2} C_A, \tag{4.40}$$

and

$$[\![p_T']\!] = -\frac{\imath\pi}{|\Delta_A|}\frac{2TB_z}{\mu_0\rho^2 v_A^2 r} C_A, \tag{4.41}$$

where $T = f_B B_\varphi/\mu_0 = k_z B_z B_\varphi/\mu_0$ and,

$$\Delta_A = \frac{d}{dr}\left(\omega^2 - \omega_A^2(r)\right). \tag{4.42}$$

Taking into account that $k_\varphi = 0$, $B_\varphi \neq 0$ and Equation (4.11), the jump conditions, Equations (4.40) and (4.41), can be written as,

$$\begin{aligned}[\![\xi_r]\!] &= \frac{\imath\pi}{|\Delta_A|}\frac{k_z B_\varphi}{\mu_0\rho^2 v_A^2} C_A \\ &= -\frac{\imath\pi}{|\Delta_A|}\frac{k_z^2 B_\varphi^2}{\mu_0\rho^2 v_A^2}\bigg|_{r=r_A} \cdot \left\{p_T' + \frac{2B_z^2}{\mu_0}\frac{\xi_r}{r}\right\}\bigg|_{r=r_i},\end{aligned} \tag{4.43}$$

and,

$$\begin{aligned}[\![p_T']\!] &= -\frac{\imath\pi}{|\Delta_A|}\frac{2k_z B_\varphi B_z^2}{\mu_0^2\rho^2 v_A^2 r}C_A \\ &= \frac{2\imath\pi}{r|\Delta_A|}\left(\frac{k_z B_\varphi B_z}{\mu_0\rho v_A}\right)^2\Bigg|_{r=r_A}\cdot\left\{p_T' + 2\frac{B_z^2}{\mu_0}\frac{\xi_r}{r}\right\}\Bigg|_{r=r_i}.\end{aligned} \tag{4.44}$$

Given that $B_z = B_z(r)$ and $\rho = \rho(r)$ in the inhomogeneous layer (see Equations 4.4, Equation (4.5) and Figure 4.2) we have,

$$\begin{aligned}\Delta_A &= \omega_A(r)^2\Delta_{AF} \\ &= \omega_A(r)^2\left[\frac{1}{\rho}\frac{d\rho}{dr} - 2\frac{1}{B_z}\frac{dB_z}{dr}\right].\end{aligned} \tag{4.45}$$

Obviously when B_z is constant across the inhomogeneous layer,

$$\Delta_A = \omega_A^2(r)\frac{1}{\rho}\frac{d\rho}{dr}. \tag{4.46}$$

Substituting Equation (4.43), (4.44) and (4.45) into Equation (4.38) and Equation (4.39) we obtain the dispersion relation for axisymmetric MHD waves that undergo resonant absorption in the Alfvén continuum of frequencies due to the twist in the magnetic field:

$$\mathcal{D}_{AR}(\omega, k_z) + \imath\mathcal{D}_{AI}(\omega, k_z) = 0, \tag{4.47}$$

where,

$$\begin{aligned}\mathcal{D}_{AR} = {} & 2\frac{D_i}{k_{ri}^2}\frac{M(a,b-1;s_i)}{M(a,b;s_i)} - 2\rho_i n_i(n_i+k_z)\frac{v_{A\varphi i}^2}{k_{ri}^2} \\ & + \frac{r_i D_e}{k_{re}}\frac{K_{\nu-1}(k_{re}r_e)}{K_\nu(k_{re}r_e)} - \frac{r_i}{r_e k_{re}^2}\left\{(1-\nu)D_e - 2\rho_e n_e^2 v_{A\varphi e}^2\right\},\end{aligned} \tag{4.48}$$

and,

$$\begin{aligned}\mathcal{D}_{AI} = {} & \frac{\pi}{\rho|\Delta_{AF}|}\frac{v_{A\varphi}^2}{v_A^4}\Bigg|_{r=r_A} \\ & \left[\frac{2}{k_{ri}^2}\left(D_i\frac{M(a,b-1;s_i)}{M(a,b;s_i)} - n_i(n_i+k_z)\rho_i v_{A\varphi i}^2\right) + 2\rho_i v_{Ai}^2\right] \\ & \left[2\frac{B_z^2}{\mu_0 r}\Bigg|_{r_A} + \frac{1}{r_e k_{re}^2}\left\{(1-\nu)D_e - 2\rho_e n_e^2 v_{A\varphi e}^2\right\} - \frac{D_e}{k_{re}}\frac{K_{\nu-1}(k_{re}r_e)}{K_\nu(k_{re}r_e)}\right].\end{aligned} \tag{4.49}$$

In these equations we used the following definitions:

$$v_{A\varphi A}^2 = \frac{B_{\varphi A}^2}{\mu_0\rho_A}, \qquad v_{AA}^2(r_A) = \frac{B_{zA}^2}{\mu_0\rho_A}, \tag{4.50}$$

$$|\Delta_{AF}(r_A)| = \frac{1}{\ell}\left|\frac{\rho_e - \rho_i}{\rho_A} - 2\frac{B_{ze} - B_{zi}}{B_z(r_A)}\right|, \tag{4.51}$$

where $\rho_A = \rho(r_A)$, $v_{AA} = v_A(r_A)$ and $B_{zA} = B_z(r_A)$. To find the radius at the resonance point, namely the radius where $v_A(r) = v_0 (= \omega_0/k_z)$[1], we can express r_A as a convex combination of the radius r_i and the width of the inhomogeneous layer ℓ since r_A must be within the interval (r_i, r_e). Therefore we can write $r_A = r_i + w\ell$, where $w \in (0, 1)$. Now we have transformed the problem of solving for r_A to a problem where we have to solve for w, the convex combination parameter. Given this formulation for r_A and Equations (4.4) and (4.5) we can write $B_{zA} = B_z(r_A) = B_{zi} + w(B_{ze} - B_{zi})$ and $\rho_A = \rho(r_A) = \rho_i + w(\rho_e - \rho_i)$. Equipped with these definitions, the equation that we need to solve to find w becomes,

$$v_{AA}^2 = \frac{(B_{zi} + w(B_{ze} - B_{zi}))^2}{\mu_0(\rho_e + w(\rho_e - \rho_i))} = v_0^2 \tag{4.52}$$

Using the definitions $\chi = \rho_e/\rho_i$, $\zeta = B_{ze}/B_{zi}$ Equation (4.52), simplifies to

$$v_{Ai}^2 \frac{(1 + w(\zeta - 1))^2}{1 + w(\chi - 1)} = v_0^2. \tag{4.53}$$

This equation is solved for w in the next section.

4.4 Long Wavelength Limit - Alfvén Continuum

Taking the long wavelength limit, $\epsilon \ll 1$, of Equations (4.48) and (4.49) and using Equation (4.29), Equation (4.31) then, Equations (4.48) and (4.49) reduce to,

$$\mathcal{D}_{AR} = \frac{\omega^2 - \omega_{Ai}^2}{k_{ri}^2} - \frac{n_i^2}{k_{ri}^2} v_{A\varphi i}^2 + \chi \frac{n_e^2}{k_{re}^2} v_{A\varphi e}^2, \tag{4.54}$$

$$\begin{aligned} \mathcal{D}_{AI} = \frac{\pi}{r_e} \left[\frac{\pi}{\Delta_{AF}} \frac{v_{A\varphi}^2}{v_A^2} \bigg|_{r=r_A} \right] \left[1 - \frac{\rho_e}{\rho_A} \frac{n_e^2}{k_{re}^2} \frac{v_{A\varphi e}^2}{v_{AA}^2} \right] \\ \left[\frac{\omega^2 - \omega_{Ai}^2}{k_{ri}^2} - \frac{n_i^2}{k_{ri}^2} v_{A\varphi i}^2 + v_{Ai}^2 \right]. \end{aligned} \tag{4.55}$$

These equations can be solved if we allow a complex frequency $\omega = \omega_r + \imath\gamma_A$, and when $\gamma_A \ll \omega_r$ we can obtain that the damping rate, γ_A, in the Alfvén continuum frequencies (Goossens et al., 1992) to second order is given by,

$$\gamma_A = -\mathcal{D}_{AI}(\omega_0) \left(\frac{\partial \mathcal{D}_{AR}}{\partial \omega} \bigg|_{\omega=\omega_0} \right)^{-1}. \tag{4.56}$$

[1] For the definition of ω_0 see Equation (4.35).

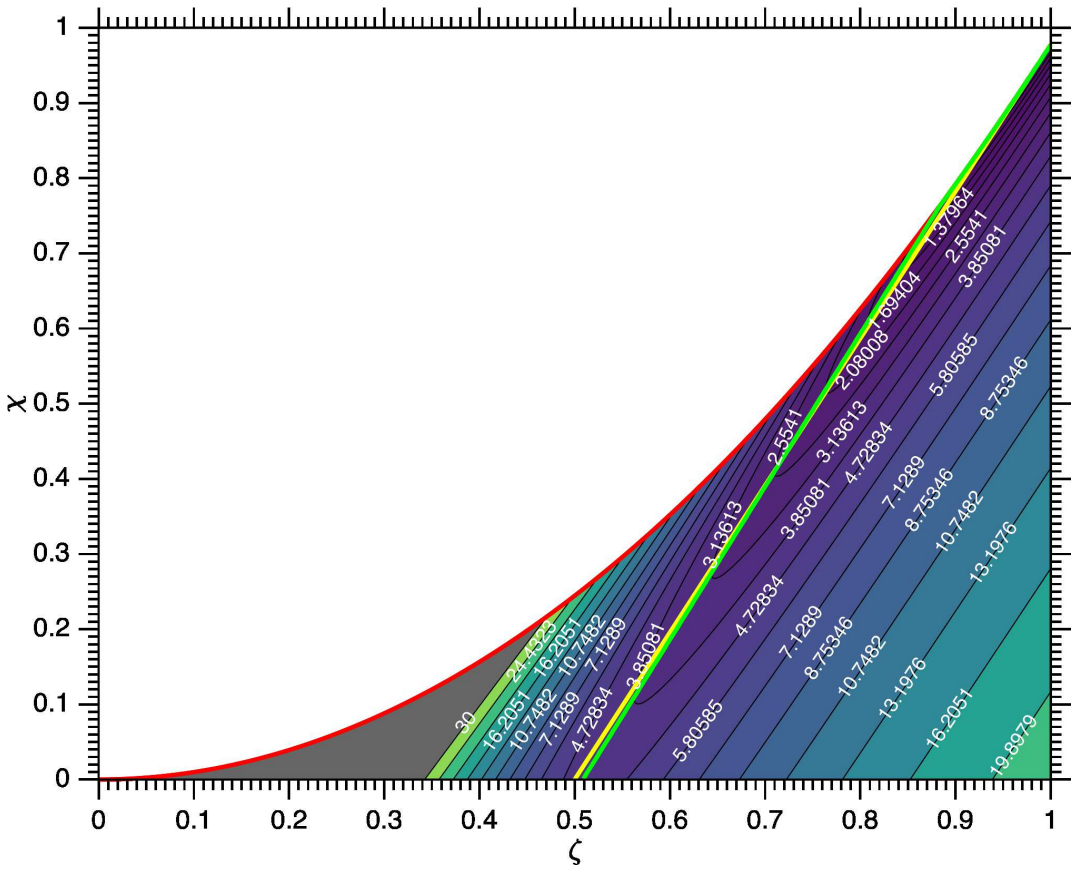

Figure 4.4: Contour map of the damping time τ_d (see Equation (4.66)) as a multiple of the period τ, plotted for density contrast in the interval $\chi \in (0, \zeta^2/h^2)$, and longitudinal magnetic field contrast in the interval $\zeta \in (0, 1)$. The remaining parameters in (4.66) are set as follows: $\ell/r_e = 0.1$ and $B_{\varphi A}/B_{zA} = 0.15$. The *red* line marks ζ^2/h^2 above which the resonance frequency is outside of the continuum. The gray region in this plot denotes damping times of 30 and above.

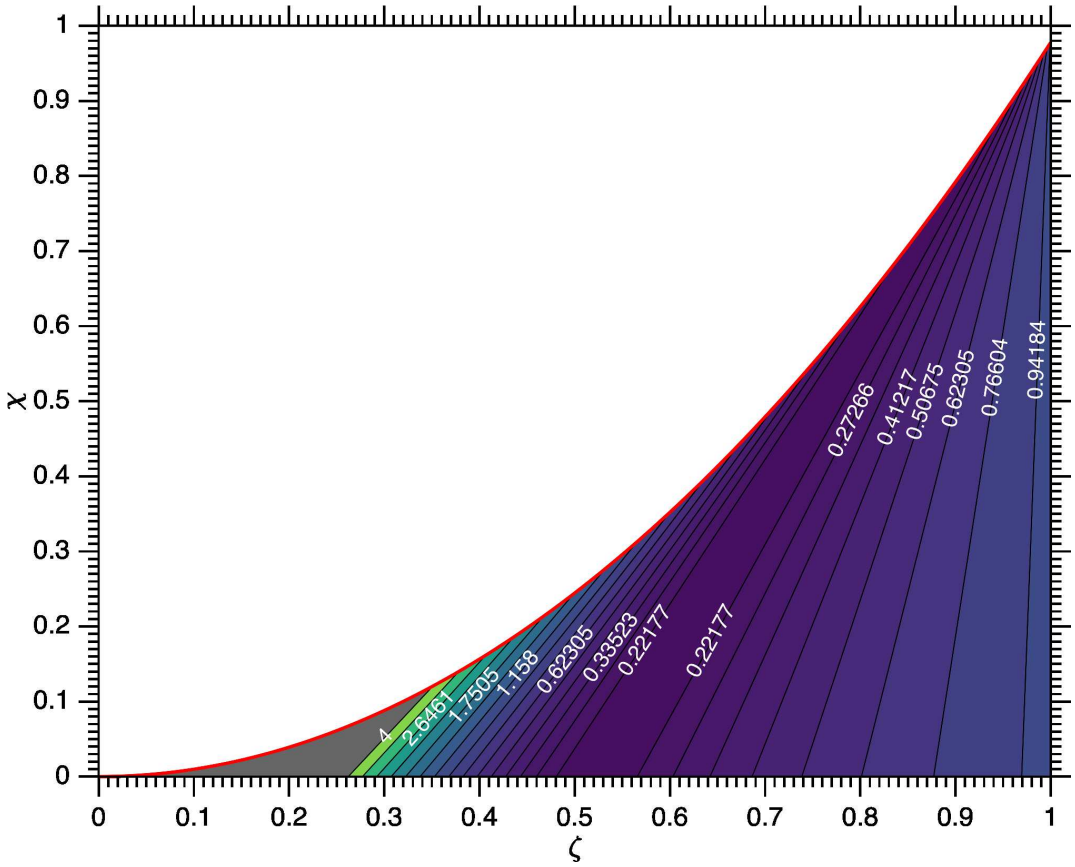

Figure 4.5: Contour map of the ratio $\tau_d(\chi, \zeta)$ versus $\tau_d(\chi, 1)$, see (4.69). The density contrast is allowed to vary in the interval $\chi \in (0, \zeta^2/h^2)$, and longitudinal magnetic field contrast in the interval $\zeta \in (0, 1)$. The *red* line is the same as in Figure 4.4, whilst values within the grey region correspond to ratios larger than 4.

This equation results in an expression that is difficult to interpret, and for this reason, given that we seek an expression for the damping rate in the long wavelength limit we expand it in a series about $\varepsilon = 0$ where $\varepsilon = r_e k_z$. This expansion results in,

$$\gamma_A = \omega_0 \frac{\pi}{Z} \frac{\ell}{r_e} \frac{\rho_A}{\rho_i} \frac{B_{\varphi A}^2}{B_{zA}^2} \left(1 + \frac{B_{\varphi A}^2}{B_{zA}^2}\right) \left(1 + \frac{B_{\varphi A}^2}{B_{zi}^2}\right) + \mathcal{O}\left(\varepsilon^2\right), \tag{4.57}$$

where

$$Z = \left| (\chi - 1) - 2 \frac{\rho_A}{\rho_i} \frac{B_{zi}}{B_{zA}} (\zeta - 1) \right|. \tag{4.58}$$

Now, in this chapter weak magnetic twist is assumed ($q = B_{\varphi A}/B_{zA} \ll 1$), therefore,

$$\frac{B_{\varphi A}^2}{B_{zA}^2} \left(1 + \frac{B_{\varphi A}^2}{B_{zA}^2}\right) \left(1 + \frac{B_{\varphi A}^2}{B_{zi}^2}\right) = \frac{B_{\varphi A}^2}{B_{zA}^2} + \mathcal{O}(q^4), \tag{4.59}$$

and so Equation (4.57) can be simplified to

$$\gamma_A = \omega_0 \frac{\pi}{Z} \frac{\ell}{r_e} \frac{\rho_A}{\rho_i} \frac{B_{\varphi A}^2}{B_{zA}^2}. \tag{4.60}$$

Here ω_0 is approximated by (4.34), i.e. $\omega_0 \approx \omega_{Ai} h$, and the radius at the resonance point, r_A, is obtained analogously to Equation (4.53), by solving,

$$\frac{(1 + w(\zeta - 1))^2}{1 + w(\chi - 1)} = h^2. \tag{4.61}$$

There are two cases to be considered. First, when $\zeta = 1$, that is $B_{zi} = B_{ze}$, and assuming $\chi \in (0, 1/h^2)$, the solution for w is

$$w = \frac{h^2 - 1}{h^2(1 - \chi)}, \tag{4.62}$$

when $1/h^2 < \chi < 1$ in this case the resonant point is outside of the continuum and there is no resonant absorption and in the limit $\chi \to 1$ the external and internal Alfvén speeds become equal and there are no propagating waves either. The second case is for values of $\zeta \in (0, 1)$ and $\chi \in (0, \zeta^2/h^2)$ for which the admissible solution is,

$$w = \frac{2(1 - \zeta) + h\left(4(\zeta - 1)(\zeta - \chi) + h^2(\chi - 1)^2\right)^{1/2} + h^2(\chi - 1)}{2\left(1 - \zeta\right)^2}. \tag{4.63}$$

When $\chi > \zeta^2/h^2$, similarly to the first case there is no resonant absorption since the resonance frequency (ω_0) is outside of the continuum. For $\zeta^2/h^2 < \chi < \zeta^2$ there are undamped propagating waves, however, when $\chi > \zeta^2$ the external Alfvén speed is smaller than the internal and no waves propagate. Lastly note, that in this investigation

we assume that $B_{zi} \geq B_{ze}$ and therefore $\rho_i = \rho_e$ has no admissible solution for w when $B_{zi} = B_{ze}$. Now, when B_z is assumed to be constant, i.e. $B_{zi} = B_{ze} = B_z$, using Equation (4.62), ρ_A/ρ_i, B_{zA}/B_{zi} and Z simplify to,

$$\frac{\rho_A}{\rho_i} = \frac{1}{h^2}, \qquad \frac{B_{zA}}{B_{zi}} = 1, \qquad Z = |1-\chi|, \tag{4.64}$$

resulting in γ_A (Equation (4.60))

$$\gamma_A = \frac{\omega_0}{h^2}\frac{\pi}{|1-\chi|}\frac{\ell}{r_e}\frac{B_{\varphi A}^2}{B_{zA}^2} = \frac{\omega_{Ai}}{h}\frac{\pi}{|1-\chi|}\frac{\ell}{r_e}\frac{B_{\varphi A}^2}{B_{zA}^2}. \tag{4.65}$$

To obtain the damping time normalised by the period of the wave, we use a typical wavelength $k_z = \pi/L$, where L is the characteristic length of the tube, the associated period is $\tau = 2L/hv_{Ai}$ (see Equation (4.35)) the damping time $(1/\gamma_A)$ for modes in the continuum as a multiple of the wave period is,

$$\tau_d = \frac{Z}{2\pi^2}\frac{r_e}{\ell}\frac{\rho_i}{\rho_A}\frac{B_{zA}^2}{B_{\varphi A}^2}\tau, \tag{4.66}$$

a contour map of this equation for $\zeta \in (0,1)$ and $\chi \in (0, \zeta^2/h^2)$, can be seen in Figure 4.4. When $B_{zi} = B_{ze}$ the damping time becomes,

$$\tau_d = h^2\frac{|1-\chi|}{2\pi^2}\frac{r_e}{\ell}\frac{B_{zA}^2}{B_{\varphi A}^2}\tau. \tag{4.67}$$

The long wavelength limit approximation of the damping rate γ_A in Equation (4.57), is accurate to $\approx 10^{-6}$ at $k_z r_e = 1$ when compared with the numerical solution of the dispersion relation in Equation (4.47). This accuracy is better than 10^{-6} for $k_z r_e < 0.1$ and is calculated using the maximum of the root mean squared error (RMSE),

$$\text{RMS Error} = \left(\frac{1}{N-1}\sum_{i=1}^{N}\left(\frac{\gamma_A - \hat{\gamma}_A}{\gamma_A}\right)^2\right)^{1/2}. \tag{4.68}$$

In this equation, γ_A is the numerically calculated damping rate, $\hat{\gamma}_A$ is the theoretical approximation in Equation (4.57) and N is the number of samples. For this error estimate we used 10^4 samples in the parameter space $(\chi, \zeta, \ell/r_e, B_\varphi/B_z)$, uniformly distributed[1].

Works investigating resonant absorption in the context of solar atmospheric conditions tend to consider solely a radial non-uniformity in either the magnetic field or

[1]Since the parameter space is not a hypercube, e.g. see Figure 4.5, we used rejection sampling for invalid parameter combinations until the desired number of samples was achieved.

density. However, accounting for radial variation in both the magnetic field and density can lead to significant variation in the estimated damping times. The ratio of Equation (4.66) over Equation (4.67) is,

$$\frac{\tau_d(\chi,\zeta)}{\tau_d(\chi,1)} = \frac{Z}{|1-\chi|}\frac{\rho_i}{\rho_A}\frac{1}{h^2} \tag{4.69}$$

and in Figure 4.5 a contour map is shown for $\zeta \in (0,1)$ and $\chi \in (0,\zeta^2/h^2)$.

It can be seen from Figure 4.4 that the behaviour of the damping rate with respect to changes in the density contrast is in some regions exactly the opposite to that for the kink mode (Goossens and Poedts, 1992, see for example). Namely, in a *roughly* triangular region in Figure 4.4 the damping rate is proportional to $\sim 1/\chi$, in contrast to the kink mode where the damping rate is proportional to $\sim \chi$. Similar behaviour has been been shown to exist in the leaky regime for sausage modes (Vasheghani Farahani et al., 2014). The factor in Equation (4.66) that determines this behaviour is $Z\rho_i/\rho_A$. We approximate the local minimum in the χ direction by evaluating the partial derivative of Z with respect to χ,

$$\frac{\partial Z}{\partial \chi} = \frac{-2\zeta + h^2(\chi-1)+2}{h\sqrt{4(\zeta-1)(\zeta-\chi)+h^2(\chi-1)^2}}, \tag{4.70}$$

which is subsequently equated to 0. From this we obtain a relation $\chi = (2/h^2)\zeta + b$ and b is identified by noting that at $\zeta = 1$, the maximum value for χ is $1/h^2$, thus the approximation is,

$$\chi = \frac{2}{h^2}\zeta - \frac{1}{h^2}. \tag{4.71}$$

As the remaining terms in Equation (4.66) do not vary with χ and ζ (note the ratio B_φ/B_z is held fixed) this approximation holds for all valid parameters. This approximation allows us to estimate in which regime a specific parameter combination is. Namely, for parameter combinations that are below the line described by Equation (4.71), for increasing density contrast ($\chi \downarrow$), damping will be slower ($\tau_d \uparrow$). For parameter combinations that result in points above this line, increasing the density contrast ($\chi \downarrow$) results in decreasing damping time ($\tau_d \downarrow$), namely waves will decay faster. This is illustrated in Figure 4.4 as a yellow line (4.71) and the exact inflection points are marked with a green line.

Given the form of Equation (4.66), and especially that of Equation (4.67), a comparison with previous results for the kink mode is in order, particularly the expression for

the damping rate obtained by Goossens et al. (1992) and later by Ruderman and Roberts (2002). In Ruderman and Roberts (2002), and Equation (73) in that work, using the notation in this work, reads as follows,

$$\tau_d = \frac{2}{\pi}\frac{r_e}{\ell}\frac{1-\chi}{1+\chi}\tau. \tag{4.72}$$

The relative magnitude of the damping time shown in Equation (4.72) and Equation (4.67) is,

$$\frac{\tau_{d,Axisymmetric}}{\tau_{d,Kink}} = \frac{h^2}{4\pi}\frac{(1-\chi)^2}{1+\chi}\frac{B_{zA}^2}{B_{\varphi A}^2}. \tag{4.73}$$

It is evident that there is a region in the parameter space of $(\chi, B_\varphi/B_z)$ for which $\tau_{d,Axisymmetric}$ is smaller when compared with $\tau_{d,Kink}$, however, this comparison is given here just as a reference and caution should be exercised in its interpretation since the damping, $\tau_{d,Kink}$ in Ruderman and Roberts (2002) was calculated for the kink mode without magnetic twist. It is possible that magnetic twist amplifies dissipation in the kink mode, and therefore still, dissipation for the kink mode may be larger than that of axisymmetric modes.

4.4.1 Numerical Solution of Dispersion Relation in the Alfvén Continuum

Equation (4.47) has been solved numerically, using ω_0 obtained in Equation (4.34) as an initial point in the solver. Additionally, by means of investigating whether another solution exists, the dispersion relation is solved again with a random ω_0 in the range (v_{Ai}, v_{Ae}). The solutions and their associated damping times can be seen in Figure 4.6. It is interesting that there exists another solution in the long wavelength limit that could not be obtained in the analysis in Section 4.4. However, given that for this solution $\tau_d \ll \tau$, it is unlikely that this mode will be observed. The phase speed of these solutions suggests that the waves corresponding to these solutions have a character that is closer to the sausage mode in a flux tube with no magnetic twist. This implies that the characteristic expansion and contraction of the sausage mode is heavily suppressed by magnetic twist. This mode could potentially be important for heating in the chromosphere due to its relatively short range.

Now, it has been shown that the singularity about the resonance point at r_A is logarithmic for ξ_r $(ln(|r-r_A|))$ and $1/(r-r_A)$ for $\xi_\perp$, so the dynamics will be governed

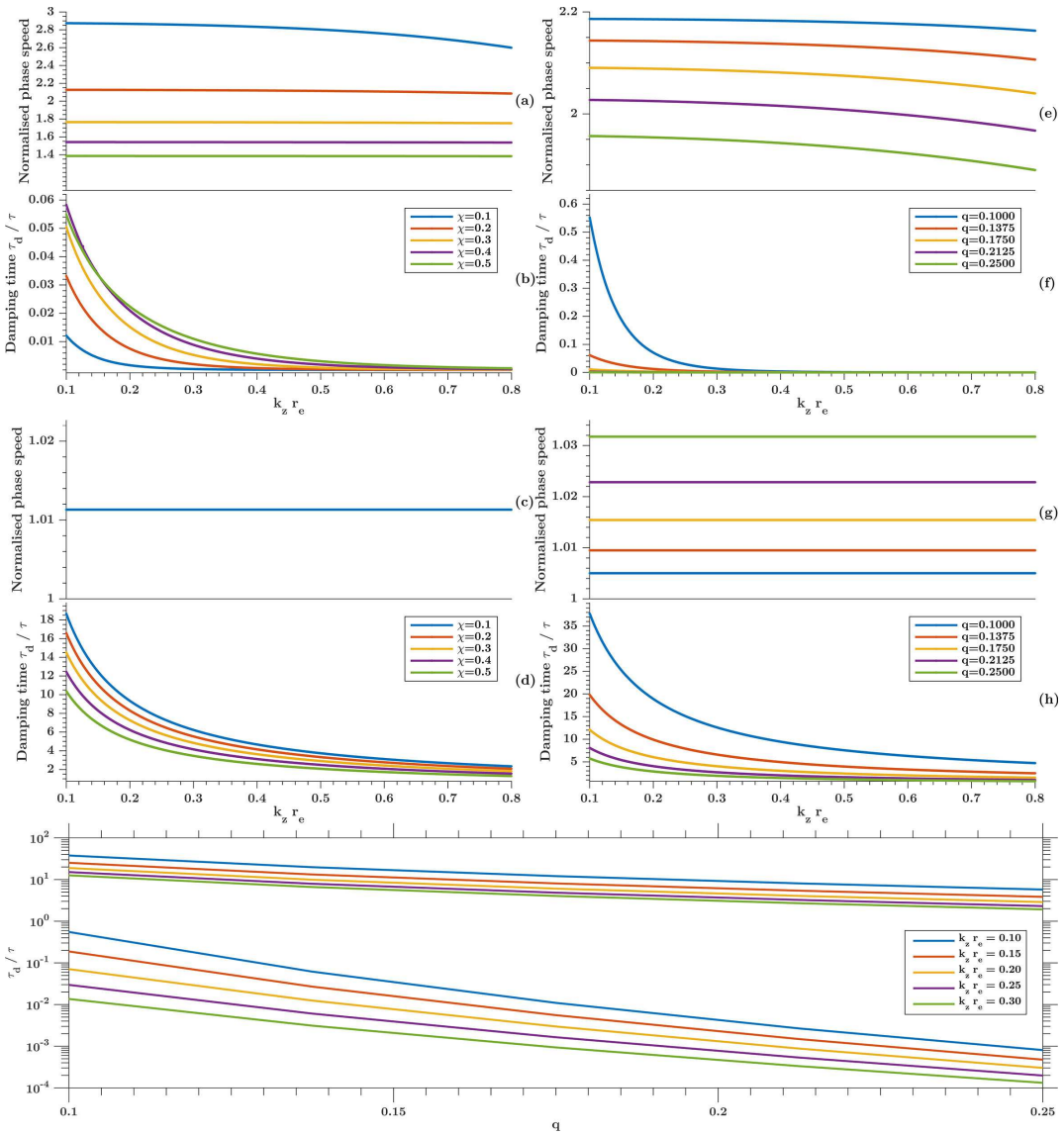

Figure 4.6: Numerical solutions of the dispersion equation Equation (4.47) for $\chi = \{0.1, 0.2, 0.3, 0.4, 0.5\}$, $q = 0.15$, $\zeta = 1$ and $\ell/r_e = 0.1$ for panels **(a)** to **(d)** ($\chi = \rho_e/\rho_i, \zeta = B_{ze}/B_{zi}, q = B_{\varphi A}/B_{zA}$) and $\chi = 0.2$, $q = \{0.1, 0.1375, 0.175, 0.2125, 0.25\}$, $\zeta = 1$ and $\ell/r_e = 0.1$ for panels **(e)** to **(h)**. The panels **(a)**, **(c)**, **(e)** and **(g)** depict the normalised phase velocity and the panels **(b)**, **(d)**, **(f)** and **(h)** the corresponding normalised damping times. The bottom panel shows a logarithmic plot of the damping time versus magnetic twist for different values of $k_z r_e$. Note that the phase speed in panel **(c)** has some variation for the different values of χ, however, this variation is on the order of 10^{-6} and is not shown as this is near the accuracy of the numerical solutions. All solutions have been obtained numerically by solving Equation (4.47).

by $\xi_\perp$ since $\xi_r/\xi_\perp \to 0$ as $r \to r_A$ and therefore $\xi_\perp \gg \xi_{re}$ in the neighbourhood of the resonant point (Poedts et al., 1989; Sakurai et al., 1991a). Also the ξ_r component provides its energy to the resonant layer (Goossens et al., 2011) and therefore the characteristic expansion and contraction of axisymmetric modes will be reduced. These facts, along with the proximity of the solution corresponding to the long wavelength limit approximation to Section 4.4 to the internal Afvén speed suggest that these waves would appear in observations to have properties similar to Alfvén waves. Given that pure Alfvén waves require $\nabla \cdot \boldsymbol{\xi}$ to be identically zero, and, a driving mechanism that is solely torsional, we argue that observed *Alfvén* waves are much more likely to be axisymmetric waves, as these do not have these strict requirements. In Figure 4.6 panels **(a)** through **(d)** show solutions for different values of χ while panels **(e)** through **(h)** solutions are shown when q is allowed to vary. The damping time for the solution for which we have an analytical approximation (see panels **(c)**) and **(d)**) increases ($\tau_d \uparrow$) for increasing density contrast ($\chi \downarrow$) while the other solution exhibits the opposite behaviour (see panels **(a)** and **(b)**) namely $\tau_d \downarrow$ for $\chi \downarrow$. However, the damping time for both solutions decreases ($\tau_d \downarrow$) for increasing magnetic twist $q \uparrow$. The bottom panel of Figure 4.6 shows a different view of the damping times as a function of the magnetic twist (q) shown in panels (f) and (h) at $k_z r_e = \{0.1, 0.15, 0.2, 0.25, 0.3\}$. From this view it can be seen that the solutions in (e) are much more sensitive to variations in the magnetic twist when compared with the solutions in panel (g). This sensitivity, in combination with the fact that for extremely small twist the sausage cut-off is reintroduced (Giagkiozis et al., 2015), means that this mode will be observable for a very small interval of magnetic twist. The mode shown in panels (c) and (d) does not present this difficulty, and therefore it is to be expected that observation of this mode is more likely. In both cases the solution corresponding to the analytic approximation remains very close to the internal Alfvén speed which is equal to 1 in Figure 4.6. Since ω_0 from Equation (4.35) depends on q, B_{zA} and the internal sound speed, these modes will appear to have a strong Alfvén character for virtually all valid parameter combinations. Lastly, k_r can be likened to the wavenumber in the radial direction, and, since in the long wavelength limit k_r is proportional to k_z, as k_z increases, the wavelength in the radial direction decreases and couples with the thin inhomogeneous layer more closely and therefore more energy per wavelength is absorbed and thus the damping

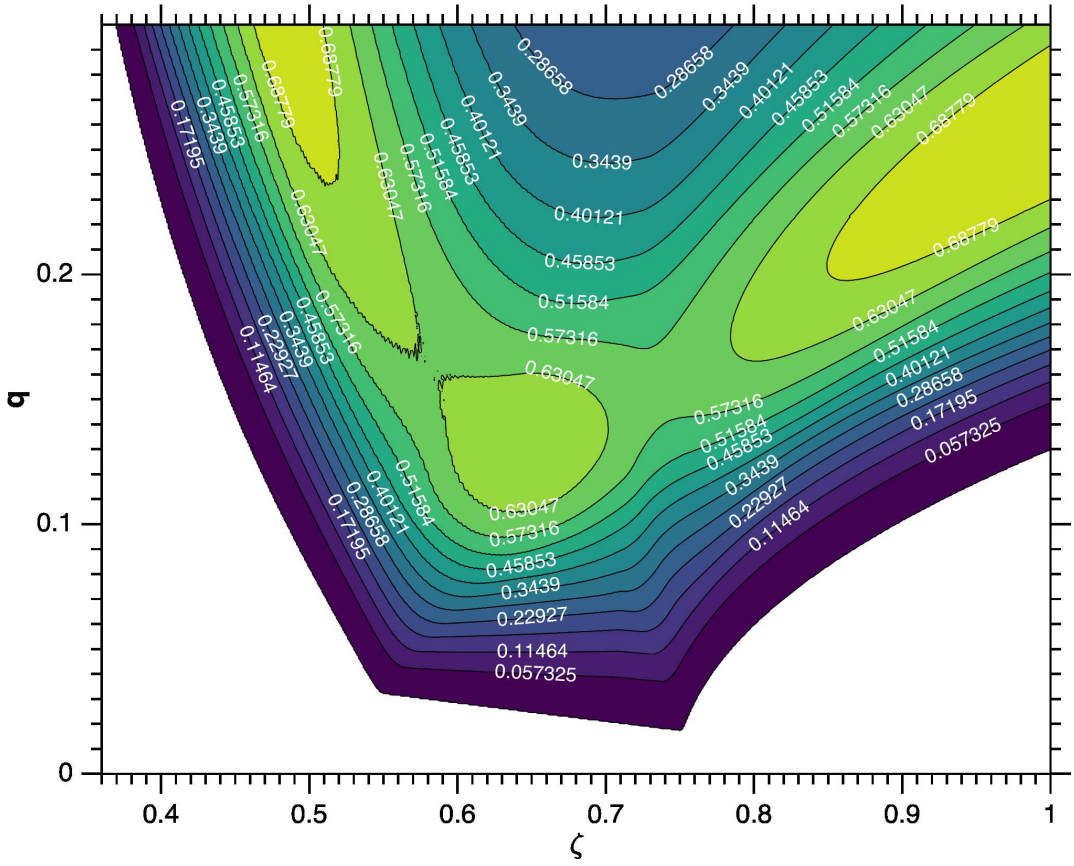

Figure 4.7: Contour map of the estimated probability (see Equation 4.74) that an axisymmetric mode can be observed to have a normalised damping time $\bar{\tau}_d$ in the range $(1, 3)$, for a given combination of (ζ, q), i.e. magnetic field contrast and twist respectively. The free parameters are $\zeta \in (0.35, 1)$ and $q = B_{\varphi A}/B_{zA} \in (0, 0.3)$ and the integration parameters are $\chi \in (0.5, 1)$ and $\ell/r_e \in (0.1, 0.5)$. The white region represents 0 probability.

time is reduced (see Figure 4.6).

4.5 Connection to Observations

Reports of observations of axisymmetric modes (sausage modes) are increasing in frequency in the recent literature. For example quasi-periodic pulsations in solar flares are believed to be associated with the kink and sausage mode (see for example Van Doorsselaere et al., 2011; Nakariakov and Zimovets, 2011; Nakariakov, 2012; De Moortel and Nakariakov, 2012; Kolotkov et al., 2015). Even more interestingly some of these pulsations appear to have periods in the interval $(15, 100)$ seconds which could be consistent with the results in the present investigation if the length-scale of

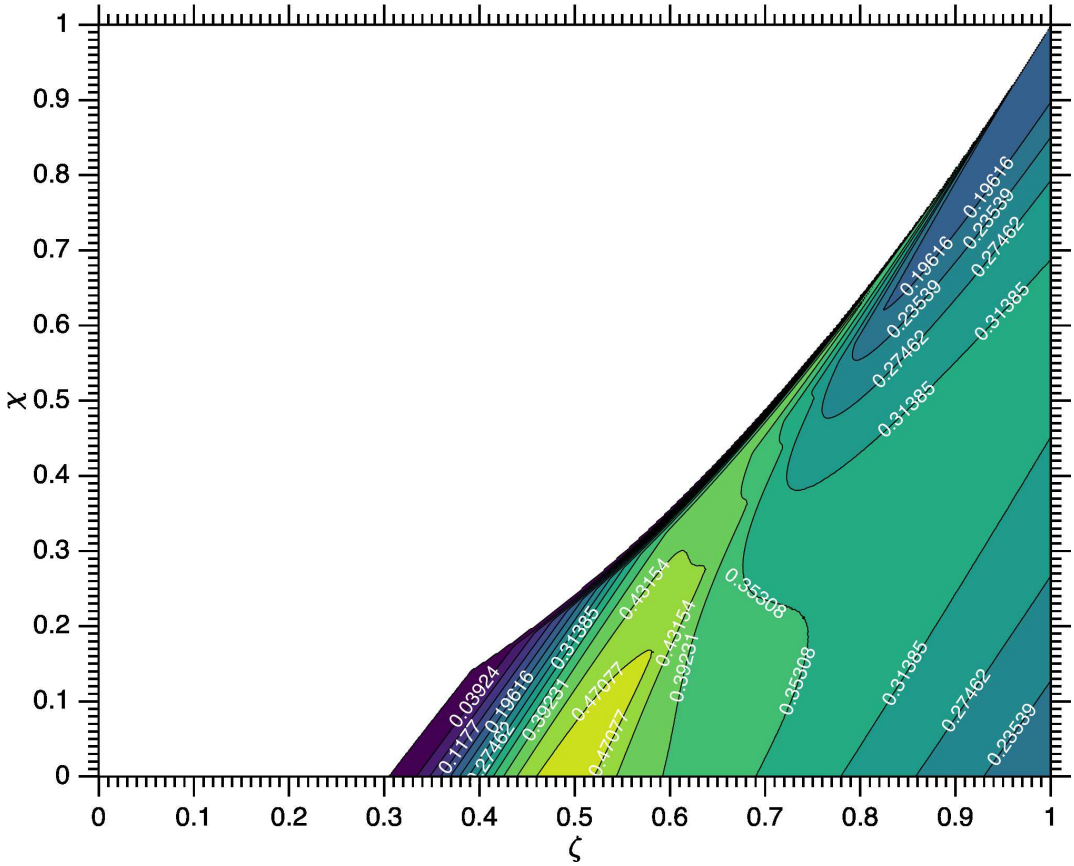

Figure 4.8: Contour map of the estimated probability for an axisymmetric mode to be observed to have a normalised damping time $\bar{\tau}_d$ in the range $(1, 3)$ for a point in (ζ, χ), i.e. magnetic field and density contrast respectively. The free parameters are $\zeta \in (0, 1)$ and $\chi \in (0, 1)$ and the integration parameters are $q = B_{\varphi A}/B_{zA} \in (0, 0.3)$ and $\ell/r_e \in (0.1, 0.5)$. Similarly to Figure 4.7 the white region in this map represents an estimated probability of 0 of observing resonantly absorbed axisymmetric modes for the particular set of parameter combinations.

these pulsations is on the same order as the length-scale of coronal flux tubes $\approx 100Mm$. Furthermore the results by Morton et al. (2012) suggest that axisymmetric modes are ubiquitous and that they appear to be coexistent with kink modes. This coexistence further supports the argument by Arregui et al. (2015); Arregui and Soler (2015); Arregui (2015) that Bayesian analysis is an essential tool for the identification of the *likely* wave modes present in observations as well as a more systematic way for the appropriate model selection. The uncertainty in determining the parameters for the kink mode led Verwichte et al. (2013) to perform a statistical analysis as a way to narrow the range of their values. This departure from *certainty* and convergence towards probabilistic inference models for solar observations is, in my view, long overdue.

Despite this increase in interest in axisymmetric modes, the relation that approximates their expected damping rate, see Equation (4.66), requires knowledge of four parameters: the density and magnetic field contrast, the relative magnetic twist and the ratio of the thickness of the inhomogeneous layer versus the tube radius, i.e. $(\chi, \zeta, q = B_{\varphi A}/B_{zA}, \ell/r_e)$. In contrast to the large body of observational evidence for the kink mode, observations of sausage waves are relatively scarce. This makes impossible an analysis similar to Verwichte et al. (2013) for these modes. Therefore, a different approach is adopted, a probabilistic approach which is related to the use of Bayesian inference suggested by Arregui et al. (2015).

As a first step towards improving this situation we provide a way to estimate the probability that an observed sausage wave has a damping rate within a specified range, given that, one or more of the four parameters in Equation (4.57) are known. The assumptions required for the validity of this estimate are the following:

- The four parameters in Equation (4.57) are independent, i.e. no parameter is a function of the others.
- The likelihood of any combination in the parameter space is the same. That is to say that there exists no preferred combination of parameters.

These assumptions are difficult to prove, especially given that there are no statistical analyses of the properties of sausage waves and reliable estimates of all four parameters. Since it is not known if there is, in fact, a set of preferred parameters, these assumptions are required for an unbiased estimate. Acknowledging these uncertainties, a first

attempt is made in identifying the probability predicted by the model presented in this chapter that a wave with the characteristics described in this investigation is resonantly damped in the long wavelength limit with a damping rate given by Equation (4.66) for a given parameter combination.

The aforementioned probability can be estimated as follows: first, the parameters for which reasonably good estimates are available are identified. These parameters are refered to as *free* parameters denoted by f. The remaining parameters are refered to as *integration* parameters and are denoted by i. Subsequently, a domain is defined for the integration parameters. Then the probability of the damping rate being within the open interval (a, b) is given by,

$$P(a, b; f_1, \ldots, f_n) = \frac{\int_C di_1 \ldots di_{4-n} w(i_1, \ldots, i_{4-n}) I_{\bar{\tau}_d > a, \bar{\tau}_d < b}[\cdot]}{\int_C di_1 \ldots di_{4-n} w(i_1, \ldots, i_{4-n}) I_1[\cdot]}, \tag{4.74}$$

$$I_{\bar{\tau}_d > a, \bar{\tau}_d < b}[\cdot] = I_{\bar{\tau}_d > a, \bar{\tau}_d < b}[\bar{\tau}_d(i_1, \ldots, i_{4-n}; f_1, \ldots, f_n)], \tag{4.75}$$

$$I_1[\cdot] = I_1[\bar{\tau}_d(i_1, \ldots, i_{4-n}; f_1, \ldots, f_n)], \tag{4.76}$$

where C is the domain of integration defined as the set of all elements in the integration parameter space that are valid according to the analysis in this chapter, and, $\bar{\tau}_d = \tau_d/\tau$. The function $I(\cdot)$ is an indicator function and $n = \{1, 2, 3\}$, i.e. an estimate for at least one parameter is necessary. When the indicator function is subscripted with 1 it simply returns one when the parameter combination is valid, namely the integral in the denominator of Equation (4.74) simply returns the area where $\bar{\tau}_d$ is defined. The indicator function in the numerator is defined as,

$$I_{\bar{\tau}_d > a, \bar{\tau}_d < b}[\bar{\tau}_d(i_1, \ldots, i_{4-n}; f_1, \ldots, f_n)] = \begin{cases} 1 & a < \bar{\tau}_d < b, \\ 0 & \text{otherwise.} \end{cases} \tag{4.77}$$

This function returns 1 when the normalised damping rate ($\bar{\tau}_d$) is within the open interval (a, b), and therefore the numerator of Equation (4.74) returns the area in C for with the normalised damping rate is within the interval (a, b). The function $w(i_1, i_2)$ is a non-negative weighting function, and, its integral over C is equal to 1. As we have assumed that every combination in the integration parameter space (i_1, i_2) is equally likely, this function is simply a constant and simplifies out from the integrals. The effect of this function is similar to the prior information in Bayesian inference. Therefore, if relevant information of a specific preference in parameter space is present in the solar atmosphere, this can be taken into account by appropriately modifying $w(\cdot)$.

For the contour maps shown in Figure 4.7 and Figure 4.8 it is assumed that the free parameters in Equation (4.74) are (ζ, q) and (ζ, χ) respectively. For this case Equation (4.74) becomes

$$P(a, b; f_1, f_2) = \frac{\int_C di_1 di_2 w(i_1, i_2) I_{\bar{\tau}_d > a, \bar{\tau}_d < b} \left[\bar{\tau}_d(i_1, i_2; f_1, f_2)\right]}{\int_C di_1 di_2 w(i_1, i_2) I_1 \left[\bar{\tau}_d(i_1, i_2; f_1, f_2)\right]}. \tag{4.78}$$

The rationale for selecting the limits for the integration parameters in Figure 4.7 is based on the reported values for the parameters $(\chi, \ell/r_e)$ and normalised damping rate, in Aschwanden et al. (2003) for the kink mode. These authors used 11 cases of observed damping kink oscillations and their estimates for these parameters are as follows: $\chi \approx 0.1$, $\ell/r_e \in (0.1, 0.5)$ and the observed normalised damping rates were in the interval $(1, 3)$. The parameter q has been selected in an interval that ensures that the magnetic twist is small. As can be seen in both Figure 4.7 and Figure 4.8 the probability for the resonantly absorbed axisymmetric modes for a wide range in parameters is significantly high. As seen in Figure 4.7, normalised damping times in the interval $(1, 3)$ are possible even for extremely small magnetic twist (≈ 0.02).

In the case where more information is available Monte Carlo simulation can be used to estimate the probability density function (PDF) of the normalised damping time. This is illustrated with two examples. First, estimates from Morton et al. (2012) are used where the magnetic field is assumed to be constant inside and outside the flux tube but this assumption is unlikely to be identically satisfied so we allow a small variation in ζ in the interval $\zeta \in (0.95, 1)$. The density contrast is taken to be in the interval $(10^{-2}, 10^{-1})$. Since Morton et al. (2012) do not provide an estimate for the width of the inhomogeneous layer we allow it to vary uniformly between $(0.1, 0.5)$, an interval that is in line with estimates by Goossens et al. (2002) and Aschwanden et al. (2003). In both examples it is assumed that the magnetic twist is within the interval $(0.1, 0.2)$. Using these intervals and assuming a uniform distribution Equation (4.66) is sampled 10^6 times. The estimated PDF for this set of parameters is the blue curve in Figure 4.9. The blue vertical line is the expectation value which is equal to $E[\tau_d/\tau] = 7.49$.

In the second example the used parameter estimates are from Van Doorsselaere et al. (2011). We assume a H plasma where, $\rho = N m_p$, $p = N k_B T$ where N is the number density, m_p the proton mass and k_B is the Boltzmann constant. With the plasma-β equal to $\beta = 2\mu_0 p/B^2$ and the assumption that $\beta_e \ll \beta_i$ (Van Doorsselaere et al., 2011)

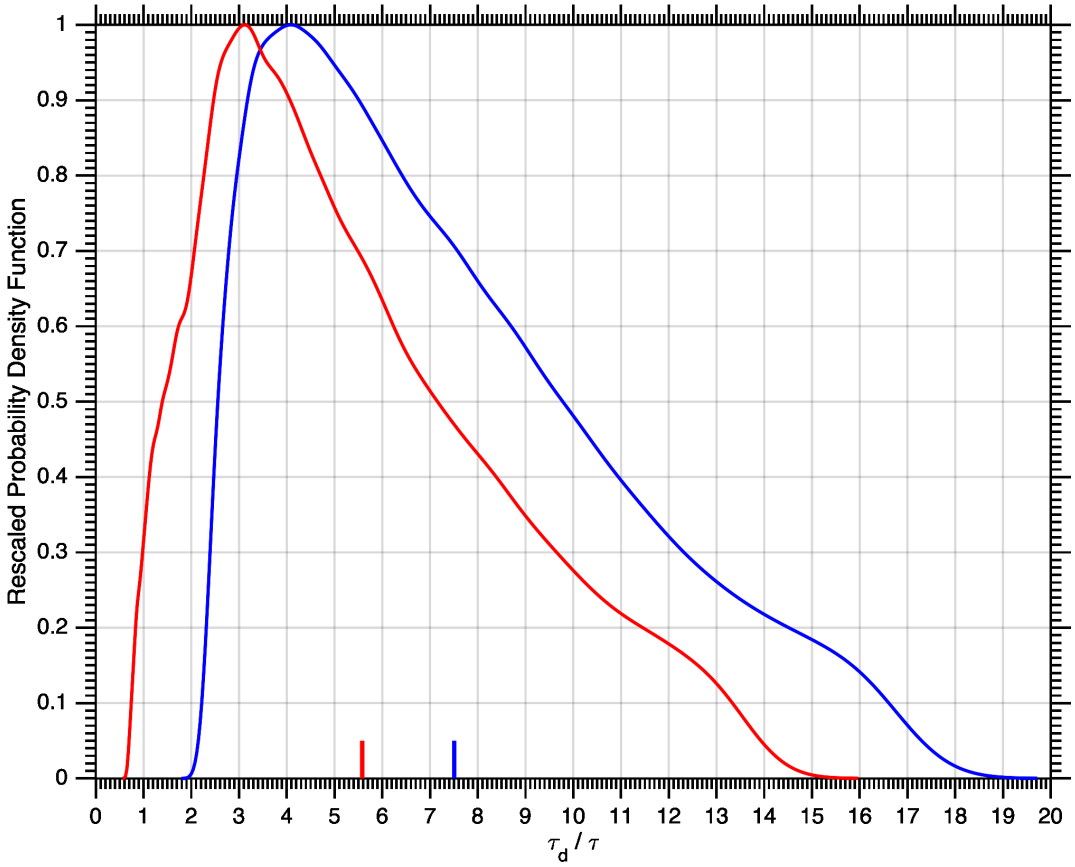

Figure 4.9: Rescaled probability density functions (PDF) of the normalised damping time using parameter estimates from Morton et al. (2012) (**blue**) and Van Doorsselaere et al. (2011) (**red**). For illustration purposes the scaling in both PDFs is such that their maximum is equal to 1. The support for the *blue* PDF is $(1.79, 19.72)$ and the expected value for the damping time is $E[\tau_d/\tau] = 7.49$. Similarly the support for the *red* PDF is $(0.56, 15.97)$ with an expected value for the damping time $E[\tau_d/\tau] = 5.58$. The intervals used for the parameters ($\chi = \rho_e/\rho_i, \zeta = B_{ze}/B_{zi}, q = B_{\varphi A}/B_{zA}$) and the associated assumptions are detailed in Section 4.5.

results in

$$\frac{\beta_i}{\beta_e} = \frac{\zeta^2}{\chi}\frac{T_i}{T_e} \gg 1. \tag{4.79}$$

Assuming a lower limit for $\beta_i/\beta_e \geq 100$ and a hot flux tube, $T_i/T_e = 10$, we can restrict ζ and χ to

$$\frac{1}{200} \leq \chi \leq \frac{\beta_e}{\beta_i}\frac{T_i}{T_e}, \tag{4.80}$$

$$\left(\chi\frac{T_e}{T_i}\frac{\beta_i}{\beta_e}\right)^{1/2} \leq \zeta \leq 1. \tag{4.81}$$

The lower limit for χ is considered as a minimum contrast in Van Doorsselaere et al. (2011) to avoid the sausage cut-off. However, in the presence of very weak magnetic twist this cut-off is removed, and therefore we don't need to assume extreme values for the density contrast. The upper limit for χ and lower limit for ζ are taken so that Equation (4.79) is satisfied. The resulting PDF can be seen in Figure 4.9. It is interesting that the expected value for the damping time in this case is 5.58 which is very close to observed damping ($\tau_d/\tau = 6$) of a mode that is believed to be a fast sausage mode (Kolotkov et al., 2015). It is apparent from Figure 4.9 that the PDFs cannot be approximated well using a normal distribution, and therefore their use for obtaining estimates of the damping time from results like Equation (4.66) in this work, and, similar equations (e.g. Goossens et al., 1992; Ruderman and Roberts, 2002) can be misleading. In contrast, Monte Carlo simulation and non-parametric density estimation can be quite useful tools for exploring this type of problems.

4.6 Summary

Theoretically, it has been known for some time, that, in the presence of weak magnetic twist, axisymmetric modes will be resonantly damped (see for example Goossens et al., 1992). In this chapter a dispersion relation for resonantly damped axisymmetric modes was calculated, for the first time, in the spectrum of the Alfvén continuum. An approximation of the damping time in the long wavelength limit was also derived. It has been shown that the damping time can be comparable to that observed for the kink mode in the case that there is no magnetic twist. Furthermore, the resulting equation (see Equations 4.47 and 4.57) was solved analytically and, i) the validity of this approximation was confirmed, and, ii) an additional solution that decays much faster in comparison

was identified. The resulting approximation in the long wavelength limit shows that the damping time is proportional to the magnetic twist and inversely proportional to the density contrast. It is interesting to note that Vasheghani Farahani et al. (2014) who investigated the damping of fast sausage modes in the leaky regime found a similar relation between the damping time and the density contrast. However, in that work a very large density contrast is required to allow observation of the sausage mode. This is not the case for one of the results of this chapter, which even for modest density contrasts (see Figures 4.7 and 4.8) the damping time is within one to three periods of the wave.

Chapter 5

Intensity Vortices in the Solar Photosphere

Vortices in the solar photosphere are fundamentally important as these coherent flows have the potential to form coherent magnetic field structures in the solar atmosphere, e.g. twisted magnetic flux tubes. These flows have traditionally been identified by tracking magnetic bright points using primarily visual inspection. This approach has the shortcoming that it introduces bias into the statistical analyses. In this chapter the process of vortex identification is fully automated using an established method from hydrodynamics for the study of eddies in turbulent flows. For the first time, this is applied to detect inter-granular photospheric intensity vortices. Using this approach, the expected lifetime of intensity vortices is shown to be much shorter ($\approx$ 17s) compared with previously observed magnetic bright point swirls. These results suggest that at any time there are 1.4×10^6 such small-scale intensity vortices covering about 2.8% of the total surface of the solar photosphere.

5.1 Introduction

Traditionally photospheric intensity flow fields have been traced using local correlation tracking of (magnetic) bright points and the revealed vortex flows have been identified by eye. This manual approach has two major shortcomings, i) it introduces observational bias into the statistical analysis and ii) a large number of vortex flow fields are most likely missed simply due to the sheer scale of the task, which also has adverse effects on the variance of the statistical analysis. Small-scale vortices in the quiet Sun regions are widely accepted to form due to turbulent convection (e.g. Shelyag et al.,

2011; Kitiashvili et al., 2012a; Shelyag et al., 2012). Solar photospheric vortex flows have drawn the attention of researchers as they have the potential to excite a wide range of MHD waves, e.g. slow and fast magneto-acoustic as well as Alfvén waves (Fedun et al., 2011). Vortex flows also appear to have a prominent role in both direct and alternating current models of solar atmospheric heating. In direct current models, neighbouring magnetic flux tubes (or strands) can become magnetically twisted under the influence of photospheric vortices. This, in turn, implies that current sheets may develop at the interface between such strands allowing the possibility of magnetic reconnection (Parker, 1972, 1983a,b; Klimchuk, 2015). In alternating current models, photospheric vortices can be seen as MHD wave drivers that can excite large scale solar tornadoes (Wedemeyer-Böhm et al., 2012; Wedemeyer et al., 2013; Amari et al., 2015). These tornadoes have an estimated net positive Poynting flux of 440W m^{-2} that is more than adequate to heat the quiet solar atmosphere whose energy flux requirement is estimated to be approximately 300W m^{-2} (Withbroe and Noyes, 1977). Unfortunately, despite the increasing interest in these coherent flows in the solar photosphere, the number of observations reported in the literature is still based on small sample sizes, with reports often associated with only a few detected events (see for example Steiner et al., 2010; Palacios et al., 2012; Park et al., 2016), or tens of observations (e.g. Bonet et al., 2008, 2010; Vargas Domínguez et al., 2011). The effect of such small a sample size in the variance of the statistical results is significant and there is the potential that there is a systematic bias introduced due to the manual nature of the process. Both of these are detrimental to the reliability of the reported results.

In this chapter a fully automated method to identify vortex flows is presented. The centre of circulation and their flow boundary is identified using a method that is based on local correlation tracking (Fisher and Welsch, 2008) applied to photospheric intensity observations, combined with an established method for identifying vortices used in the study of turbulence (Graftieaux et al., 2001). Subsequently, characteristic vortex parameters are estimated, such as lifetime diameter, mean perpendicular velocity and area.

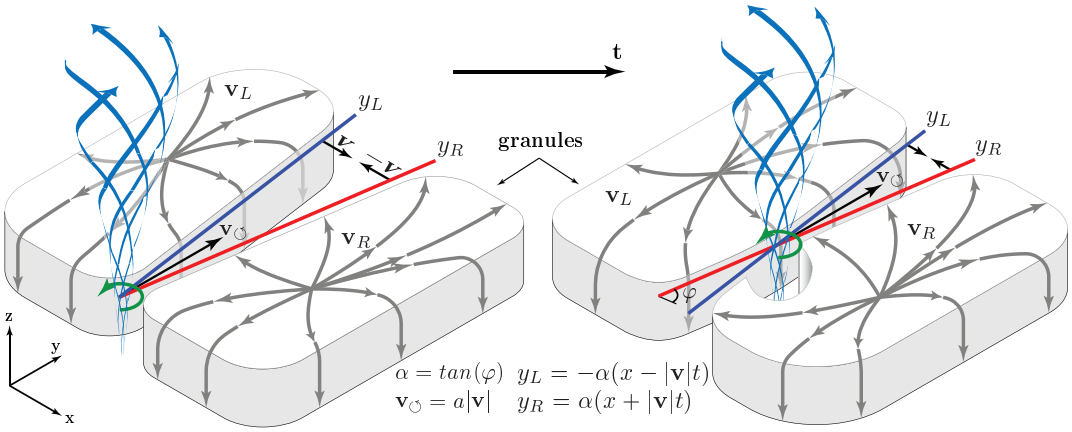

Figure 5.1: The proposed physical mechanism modelling the high velocity of vortex centres. The line segments y_L and y_R, shown in blue and red color, respectively, represent the edges of two neighbouring granules. In this instance, the two edges are moving towards each other with speed $|\mathbf{v}|$. The streamlines in the plane outline the velocity field near the edges of the granules, with $\mathbf{v}_L$ and $\mathbf{v}_R$ denoting the velocity field in the left and right granule, respectively. The velocity of the vortex centre is labelled $\mathbf{v}_\circlearrowleft$. The blue streamlines in the z-direction depict magnetic field lines above the vortex centre. The black arrow shows the evolution.

5.2 Observations and Vortex Identification Process

5.2.1 Observations

The observations investigated here were carried out between 08:07:24–09:05:46 UT on the 21st June 2012, with the CRisp Imaging SpectroPolarimeter (CRISP) at the Swedish 1-m Solar Telescope (SST: Scharmer et al., 2003, 2008) at La Palma. The image resolution of the CRISP observations is 0.059″per pixel. A quiet Sun region very close to disk centre was observed with an effective Field-Of-View (FOV) of 55×55 arcsec, centred on solar-x=−3.1″ and solar-y=69.9″. The required accuracy of the pointing of the CRISP FOV, in heliocentric coordinates, was achieved through co-alignment of bright-points observed with the CRISP wideband images, together with co-temporal continuum images in 170.0nm from the Solar Dynamics Observatory / Atmospheric Imaging Assembly (SDO/AIA: Lemen et al., 2012). The sequential spectral scans comprise a full-Stokes IQUV scan at −0.0048nm from the Fe I 630.2nm line core. The spectro-polarimetric sequences have a post-reduction mean cadence of 8.25s. After acquisition, the data was processed with the Multi-Object Multi-Frame Blind Deconvolution (MOMFBD) algorithm (van Noort et al., 2005; van Noort and Rouppe van der Voort, 2008; de la Cruz Rodríguez et al., 2015).

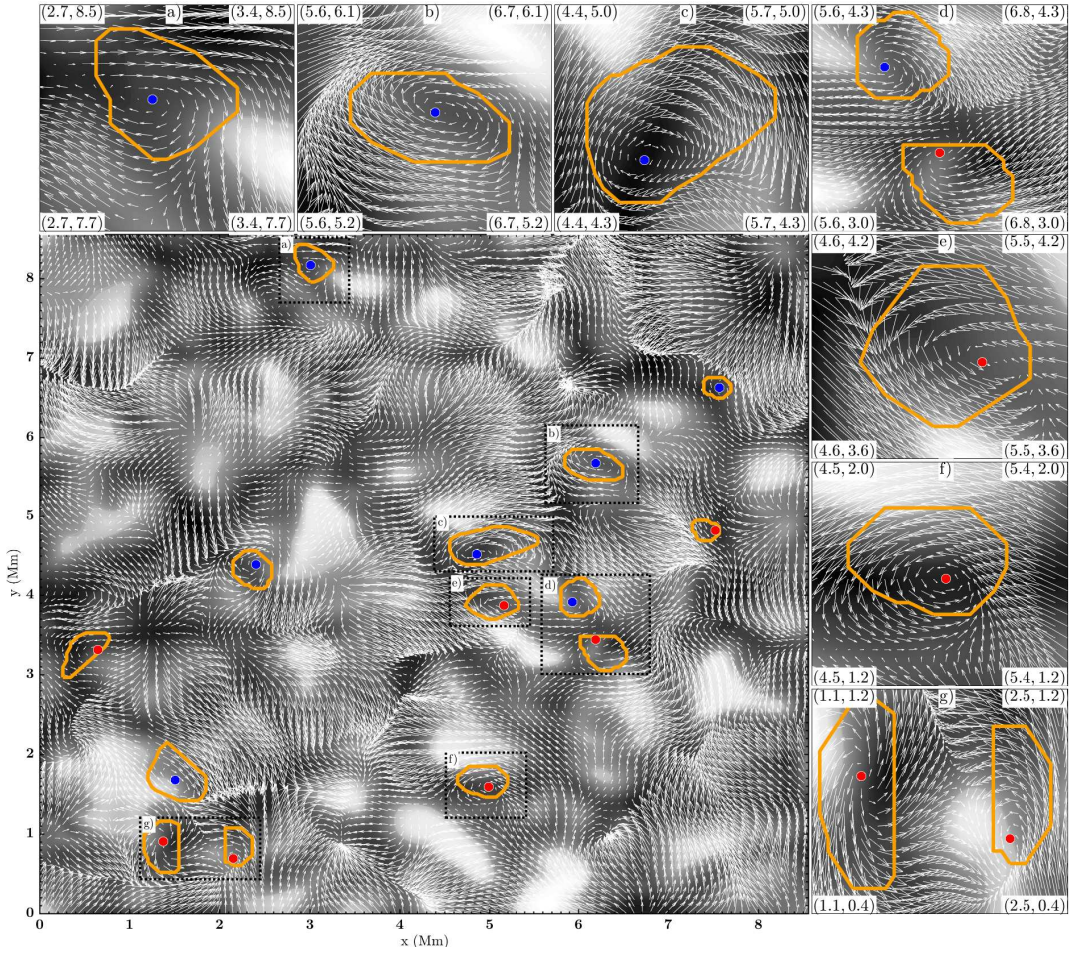

Figure 5.2: A snapshot of the estimated velocity field based on the Fe I continuum (intensity shown in grey-scale) using local correlation tracking (LCT), illustrating the identified vortices and their boundaries. The circles denote the vortex centre, with red referring to counter clockwise vortices (positive) and blue clockwise vortices (negative). The orange border line denotes the vortex boundary.

5.2.2 Vortex Identification Process

The automated vortex identification methodology presented here is split into four stages: i) pre-processing, ii) velocity field estimation, iii) vortex identification and, iv) vortex lifetime estimation. The intensity maps obtained from observations have varying intensity at different times that appears to be due to atmospheric effects. This intensity variation is a few standard deviations from the mean and the effect is global, i.e. affects almost equally the entire image and disappears in subsequent frames. To counter these effects image histogram equalization (e.g. Pizer et al., 1987) is used in the following way:

- First, the expected distribution of intensities is estimated by means of averaging the histogram distributions across all frames. The rationale for this is that the Sun is not expected to change its power emission spectrum, in the mean, during the time of the observation.

- Once the expected intensity distribution has been obtained, histogram equalization is applied to all frames using that distribution as a reference.

This procedure is fast and efficiently removes inter-frame *flickering*, and, improves the numerical stability of the LCT method.

The pre-processing stage removes rapid intensity fluctuations, while preserving the relative counts as much as possible. Subsequently, we remove the mild *seeing* effects in our observations using a Gaussian filter. Although it is well known that atmospheric seeing is a non-linear effect (see e.g. November and Simon, 1988), given that the seeing conditions were good, this simple averaging method produced similar results to destreching algorithms and is computationally more efficient. To avoid the reduction of the temporal resolution a moving-average Gaussian filter is employed with a 3dB attenuation at quarter the Nyquist frequency $1/(8T)$ where T is the cadence. The velocity field estimation is performed using fast local correlation tracking (FLCT) (Fisher and Welsch, 2008). This filtering was empirically determined to result in a small reduction in the identified number of vortices from the data, therefore the subquently presented results are to be interpreted as a lower bound of the number of vortices present in the observational data used.

For the vortex identification, a proven and established method is implemented that has its roots in the study of turbulence in fluid dynamics. Once the velocity field estimates are found, the same approach as Graftieaux et al. (2001) is used to identify the vortex centres and boundaries. Graftieaux et al. (2001) defined two functions Γ_1 and Γ_2, for the identification of the vortex centres and boundaries, respectively. The function Γ_1 used in this chapter is,

$$\Gamma_1(\mathbf{x}_p) = \frac{1}{|S|} \sum_S \frac{((\mathbf{x}_m - \mathbf{x}_p) \times \mathbf{v}_m) \cdot \mathbf{1}_z}{||\mathbf{x}_m - \mathbf{x}_p||_2 \cdot ||\mathbf{v}_m||_2}. \tag{5.1}$$

Here, $S = \{\mathbf{x}_m : ||\mathbf{x}_m - \mathbf{x}_p||_2 \leq R\}$ is a disk of radius R about the point $\mathbf{x}_p$, $||\cdot||_2$ is the Euclidean norm, $\mathbf{1}_z$ is a unit vector normal to the plane and $|S|$ is the cardinality of S. Γ_1 defines a scalar field and its magnitude achieves a maximum at unity. Graftieaux et al. (2001) shows that this function achieves this maximum when $\mathbf{x}_p$ is at the centre of an axisymmetric vortex. However, given that ideal axisymmetric vortices are quite uncommon, the threshold for classifying a point in S as a potential vortex centre is reduced to 0.9, and, the local maximum of these points is classified as the vortex centre. For the identification of the vortex boundary, we use the discrete version of Γ_2, defined as,

$$\Gamma_2(\mathbf{x}_p) = \frac{1}{N} \sum_S \frac{((\mathbf{x}_m - \mathbf{x}_p) \times (\mathbf{v}_m - \bar{\mathbf{v}}_p)) \cdot \mathbf{1}_z}{||\mathbf{x}_m - \mathbf{x}_p||_2 \cdot ||\mathbf{v}_m - \bar{\mathbf{v}}_p||_2}, \tag{5.2}$$

where $\bar{\mathbf{v}}_p$ is the mean velocity in the neighbourhood of the point $\mathbf{x}_p$. It is shown by Graftieaux et al. (2001) that in the inner core of a vortex the magnitude of Γ_2 is larger than $2/\pi$. Flows with values of $\Gamma_2 < 2/\pi$ are dominated by strain and when $\Gamma_2 = 2/\pi$ we have a pure shear. The velocity vectors required by Equations (5.1) and (5.2) were estimated using local correlation tracking (FLCT by Fisher and Welsch (2008)).

Let us now calculate the vortex centres and their boundaries at every time instance, however, simultaneously the lifespan of these vortices also needs to be estimated. For this purpose we assume that the vortex centre can move at approximately the sound speed of the photosphere, about $10\,\mathrm{km\,s^{-1}}$ (Nordlund et al., 2009). If the speed of the vortex centres is comparable to the sound speed, this would suggest that the maximum distance a centre could traverse from one frame to the next would be 82.5km, which is almost 2 pixels at the spatial resolution of observational data. However, at present the vortex formation mechanism has not been clearly established and if such flows in

the photosphere are formed as shown in Figure 5.1, the speed of their centre may be much larger than the sound speed. The edges of the granules are represented as line segments (red and blue line segments in Figure 5.1). These are defined to be the points where the vertical component of the velocity transits from being mostly positive, as is on granules, to being negative, as is the case in the inter-granular lanes. Due to the dynamic nature of the granulation pattern on the photosphere, their edges are in constant relative motion with respect to the edges of neighbouring granules. This relative motion, in combination with the converging flows from neighbouring granules at an angle, produces effectively counter streaming (or shear) flows at the line where the two flows meet. This effect can drive vortex flows whose centres can move ($\mathbf{v}_{\circlearrowleft}$) at much larger speed compared with the relative speed that generated them (see Figure 5.1). Therefore, using a conservative estimate it is assumed that vortices that are within a 4 pixel radius in two consecutive times, are in fact the same vortex. An alternative vortex formation mechanism for flux tubes whose footpoints are relatively stationary compared with the timescale of downdrafts within the tubes is suggested by Williams and Taroyan (2018).

5.3 Results and Statistical Analysis

A representative example of the results obtained from the vortex identification process is shown in Figure 5.2. The grey-scale denotes intensity, normalised in the range 0 to 1 corresponding to black and white, respectively. Over-plotted is the LCT estimate of the *surface* velocity field. The red-filled circles mark counter-clockwise vortex flows (positive), blue circles correspond to clockwise flows (negative) and the orange line delimits the vortex flow boundary.

Figure 5.3 and Figure 5.4 show statistical results based on a sample size of $N = 26,988$ vortices. As the only source of information that is used here is based on LCT applied to intensity observations, the identified vortex flows are referred to as *intensity vortices*. This is to acknowledge line-of-sight integration effects and temperature variations that, from a practical standpoint, lead to the estimated velocity field being a weighted average of the plasma motions at different heights within the spectral line formation height (Nordlund et al., 2009).

The results suggest that the expected lifetime of such vortices is independent of

orientation (see a) and b) in Figure 5.3). In fact, no statistically significant deviations in the distributions of positively or negatively oriented vortices have been found, for any of the measured parameters, i.e. lifetime, space and time density, diameter, area or perpendicular speed (see Figure 5.3 and 5.4). What is intriguing however, is that for the majority of vortices (approximately 85%) their expected lifetimes are less or equal to three times the cadence (24.75s). This is much shorter when compared with similar features identified by tracking magnetic bright points (BPs) (e.g. Bonet et al., 2008). The apparent discrepancy could be attributed to errors in LCT, where very short lived structures are the result of errors in the identified velocity field. Notwithstanding this limitation, LCT velocity maps have been shown to be a good first order approximation to the velocity field (Verma et al., 2013; Louis et al., 2015). Nevertheless, it is unlikely that the identified vortex lifetimes are due to an LCT discrepancies. This is based on our experience with LCT and the fact that we could not find a study that suggests that LCT introduces, in a statistically meaningful way, some form of bias that would collectively distort vortices sufficiently to reduce their lifetimes. If this intuition is correct, observations with improved imaging equipment (both cadence and spatial resolution) should reveal vortices with even smaller lifetimes in the solar photosphere.

Assuming an expected lifetime, for both positive and negative vortices, of $\tau = 0.29$ min (see **a)-b)** in Figure 5.3) and the space and time density of vortices $d = 0.84\ \mathrm{Mm}^{-2}\,\mathrm{min}^{-1}$ (see **e)** in Figure 5.3), it is estimated that there will be $\tau \cdot d = 0.244\ \mathrm{Mm}^{-2}$ vortices at any time. In turn, this implies that there are continuously 1.48×10^6 vortices over the whole photosphere. Under the assumption that the expected lifetime, as well as, space and time density in other regions of the photosphere are similar to our observations. If intensity vortices are indeed closely correlated with the actual velocity field, then based on the simulation results reported by Kitiashvili et al. (2012a,b) it is anticipated that their expected size will decrease with the advent of higher spatial resolution observations. A prime example of near future expected capability is the Daniel K. Inouye Solar Telescope (DKIST) whose visible broadband imager is planned to have spatial resolution of 16km to 25km per pixel, at 430.4nm and 656.3nm, respectively, and cadence of 3.2s (Berger and ATST Science Team, 2013).

Figure 5.4, panels **e)** and **f)** show the distribution of the average perpendicular speed within the vortex boundary. This is calculated by projecting the velocity vector

	d ($\mathrm{Mm}^{-2}\,\mathrm{min}^{-1}$)	τ (min)	$\tau \cdot d$ (Mm^{-2})	$E(\#)$ on Photosphere	Sample size
Current chapter	0.84	0.29	0.244	1.48×10^6	26,988
(Bonet et al., 2008)	1.8×10^{-3}	5.1	0.92×10^{-2}	0.55×10^5	138
(Bonet et al., 2010)	3.1×10^{-3}	7.1	2.2×10^{-2}	1.3×10^5	42
(Vargas Domínguez et al., 2011)	1.6×10^{-3}	15	2.4×10^{-2}	1.46×10^5	144
(Wedemeyer-Böhm et al., 2012)	(1.4×10^{-4})	(12.7)	(1.8×10^{-3})	(1.1×10^4)	(14)

Table 5.1: Summary statistics of space and time density (d), expected lifetime (τ), number of vortices per Mm^2 ($\tau \cdot d$) and expected number of vortices on the solar photosphere ($E(\#)$). In the last column the number of vortices on which the statistical analysis is based on is provided. The values in the last row in the table are in parentheses since they do not correspond to observations in the photosphere, however, these are included for reference.

at every point within the vortex to a vector perpendicular to the ray emanating from the vortex centre. Finally, panel **g)** in Figure 5.4 provides an estimate of the percent of the area of the photosphere covered by intensity vortices at any time.

5.4 Summary

There is an abundance of small-scale intensity vortices in the quiet Sun and their typical lifetimes are approximately 17 seconds. It is estimated that at any given time, the expected number of vortices in the photosphere is 1.4×10^6 and that they occupy 2.8% of the photosphere at any time. Although the area of these vortices may appear small in the photosphere, even if only a tenth of these vortex flows reaches the lower corona they may occupy more than 17% of its total area due to magnetic expansion.

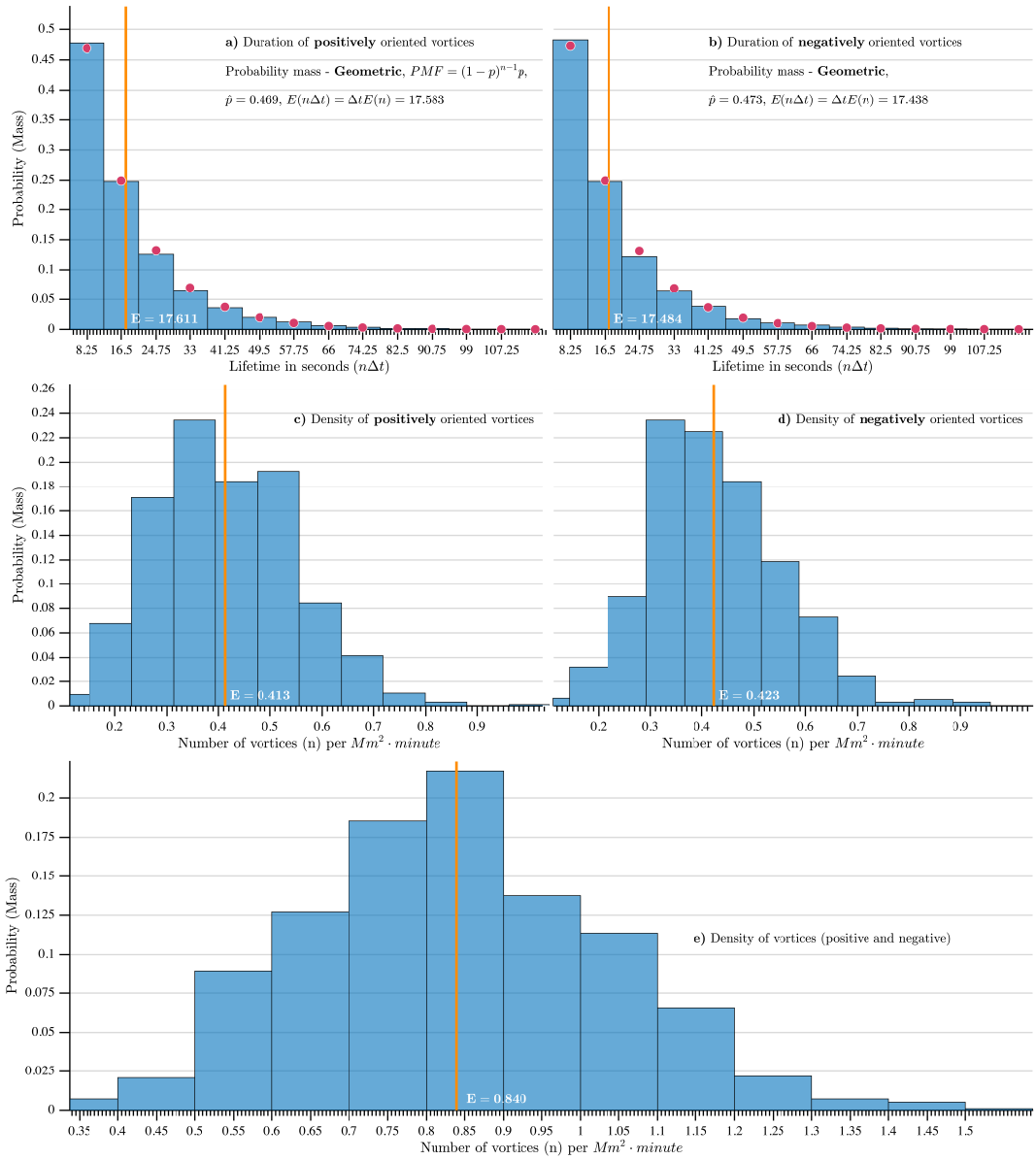

Figure 5.3: Estimates of (**a** and **b**) vortex lifetime mass function, and (**c**,**d** and **e**) the number of vortices per $Mm^2 \cdot minute$. The red circles denote the best fit of a parametric mass density function (PMF). In this case, the Geometric distribution was a best fit for the lifetimes of the vortices. The orange line, and the white font E on its right, is the expected value calculated from the empirical distribution of the data. Values with a *hat* indicate best fit parameter estimates for the particular distribution, and, $E(\cdot)$ is the expected value.

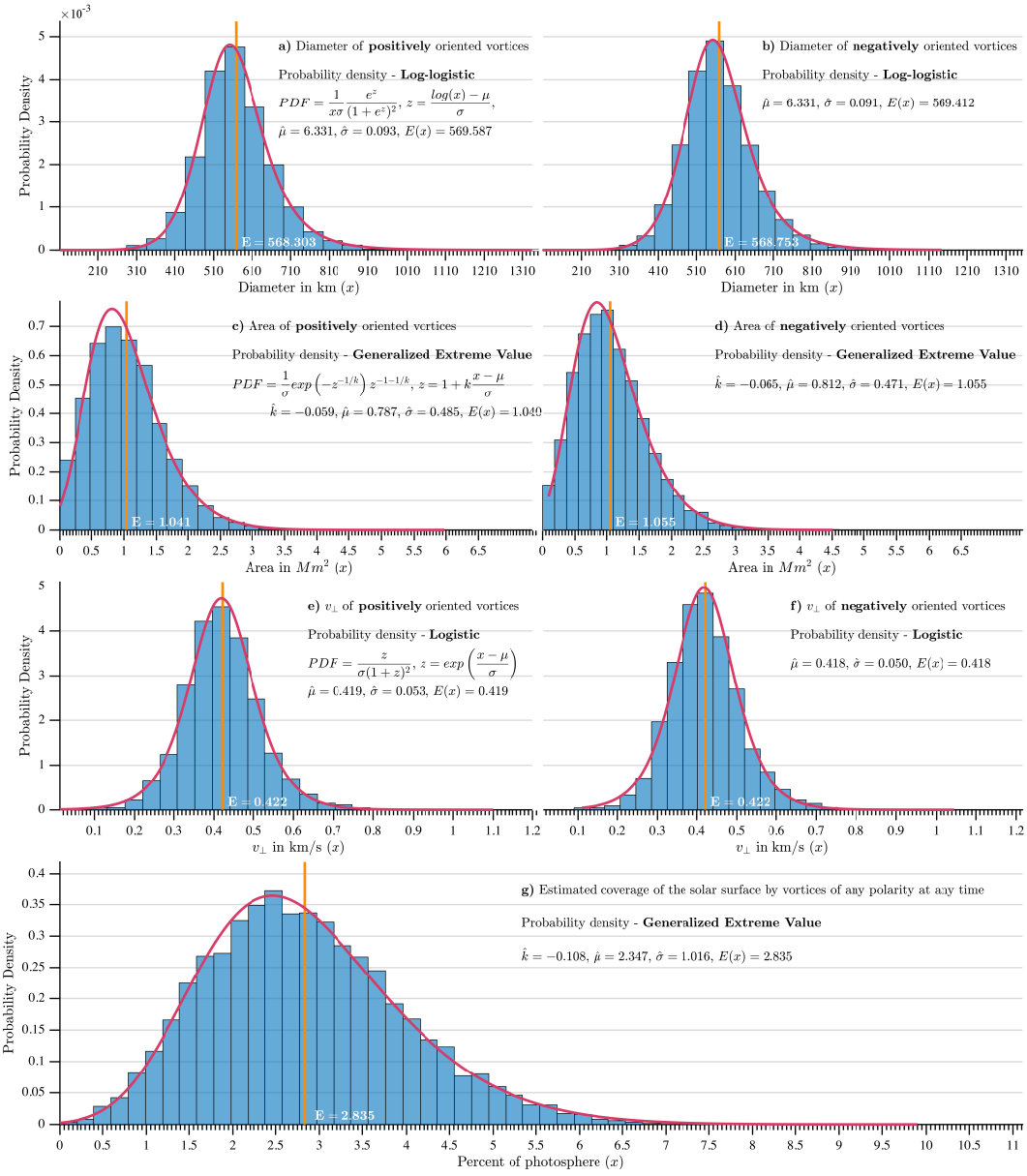

Figure 5.4: Empirical and parametric estimates of the probability density function (PDF) for (**a** and **b**) the vortex diameter, which is calculated using the average of the minor and major axis of a best fit ellipse for every vortex, (**c** and **d**) the area of vortices (in Mm^2), (**e** and **f**) the magnitude of the perpendicular velocity ($|v_\perp|$) and lastly (**g**) an estimate of the percentage of the total photosphere covered with intensity vortices. The notation in this figure follows Figure 5.3.

Chapter 6

Conclusions and Further Research

6.1 Intensity Vortices

Vortex flows in the solar atmosphere may contribute significantly to the energy flux requirements for heating the quiet Sun atmosphere. However, for that connection to be established strong evidence is required: i) vortex flows motions are ubiquitous in the solar atmosphere, ii) that these motions appear at different heights, e.g. photosphere, chromosphere and corona. The results from Chapter 5 provide evidence supporting the first of these requirements. However, at this point it is unclear if these vortices extend to higher layers of the solar atmosphere (i.e. choromosphere and above). If in fact some of the vortices identified in Chapter 5 do extend above the photosphere, the proportion that does so is an important quantity to be measured.

To illustrate the importance of these questions consider the following conjecture that is based on the similarities in scale and location of vortex flows identified in Chapter 3 with small-scale whirlpools (or swirls) reported by Bonet et al. (2008, 2010) and Vargas Domínguez et al. (2011). The conjecture is that these are, in fact, the same flow features in the quiet Sun. If that is indeed the case, then remarkably the number of vortices in the photosphere would be an order of magnitude larger than previous estimates. Now, consider that if these are related with previously identified magnetic tornadoes by Wedemeyer-Böhm et al. (2012) (another open question), then the estimated number of these tornadoes will also be up for revision by as much as an order of magnitude. If intensity vortices prove to be the root cause of solar tornadoes (Amari et al., 2015), then this would suggest that 10% of the photospheric vortices reach the lower corona

forming magnetic tornadoes. This has the extraordinary implication that at least 17% of the area of the lower corona is constantly supplied with a positive Poynting flux of $440\mathrm{W\,m^{-2}}$, as opposed to 1.2% implied from Wedemeyer-Böhm et al. (2012). The assumptions in this revised estimate are that the photospheric vortices that do extend up to the lower corona have a mean radius of 1.5Mm, their *corrected* expected number is 1.48×10^5 vortices at every time, i.e. 10% of our intensity vortices on the photosphere, instead of 1.1×10^4 (see Table 5.1) and that the average net positive Poynting flux in each magnetic tornado is $440\mathrm{W\,m^{-2}}$. Furthermore, based on a Monte Carlo simulation emulating the positions of intensity vortices, it is found, subject to the assumptions above, that within 5 vortex periods (approximately 88s) at least 60% of the area of the lower corona will have been swept by tornadoes and within 10 periods (176s) this increases to more than 84%. This means that if, i) there is an effective enough dissipative layer in the lower corona to the energy flux supplied by magnetic tornadoes, and ii) intensity vortices are the cause of magnetic tornadoes, then the coronal heating problem in the quiet Sun may be near its resolution.

The automated identification approach used in Chapter 5 illustrates another important point. We must transcend small scale analyses that focus on single, or a very small number of events. Using the methods elaborated upon in Chapter 5 a significantly larger number of vortices was identified when compared with previous observational studies. This is evidence consolidating the fact that small-scale vortices are prevalent in the solar photosphere. Most interestingly, an overwhelming majority of these vortices have lifetimes that are often much shorter than previously believed, which suggests that these flows are highly dynamic in nature.

Due to the episodic nature of the formation of these small-scale vortices, any magnetic field through them will be supplied with a broadband impulse comprised of both torsional and radial components which will generate propagating MHD waves an argument that is especially relevant to the axisymmetric waves studied in Chapter 3 and Chapter 4 due to symmetry considerations. The presence of a magnetic field in vortices is consistent if we recall that their location is in the inter-granular lanes where the magnetic field concentrations are highest. Both observational and numerical simulations (e.g. Fedun et al., 2011) support the idea that MHD waves with a broad frequency range can be generated by vortex flows. However this is to be expected on more fun-

damental grounds due to a particular duality in frequency space. Localisation in time, leads to spread (broadening) in the frequency domain and vice versa. In physical terms this implies that the rapidity of vortex formation alongside with deviation from axi-symmetry offer a wave driver that results in waves of different frequencies, albeit with different amplitudes. Regarding energy transport to the upper layers of the atmosphere, numerical simulations suggest that vortex driven MHD waves (Amari et al., 2015) are a prime candidate.

The most compelling differences compared with previous reports (e.g. Bonet et al., 2008, 2010; Vargas Domínguez et al., 2011) are in the expected lifetime and, space and time density. Table 5.1 shows summary statistics comparing the main results in Chapter 5 with previous studies that are based on more than 3-4 observed vortices. In my view, there are at least two explanations for this mismatch. First, vortex flows and any type of feature tracking in observations, is time consuming and error prone when performed manually. This increases the likelihood of bias and increases the variance of the analyses. In addition, lifetime estimates relie on the accuracy of LCT for the surface velocity field identification, which, although has been shown to have reasonable correlation with the true velocity field (Louis et al., 2015), is only a first approximation to small-scale motions in inter-granular lanes. Notwithstanding this uncertainty, given that the chosen automated technique is straightforward to implement, the results can be cross-validated by other studies, which, in my view, is extremely important.

6.2 Axisymmetric MHD Modes and Resonant Absorption

The abundance of twisted magnetic fields that is reinforced by the results in Chapter 5 motivated the work performed in Chapter 3 and Chapter 4. In Chapter 3 it was shown that for weak magnetic twist in a straight flux tube model axisymmetric modes (sausage) exhibit a more elaborate character due to being coupled to axisymmetric Alfvén waves. This coupling leads to similarities in the Doppler signatures of the studied axisymmetric modes and *pure* Alfvén waves as described in a stright flux tube model with no magnetic twist. Importantly, for coronal conditions, the fast sausage body waves remain trapped for all wavelengths when the magnetic twist strength is above a certain threshold. This most interesting result may be surprising to theorists as, in the straight magnetic flux tube with constant magnetic field model, there exists a

cutoff in the long wavelength limit for sausage modes. This result means that this mode, in conditions that are closer to the physical reality in the solar atmosphere, are allowed to propagate. Furthermore, given that there exists a $\pi/2$ phase difference between the radial and torsional velocity perturbations these waves can easily be mistaken for pure Alfvén waves.

In particular, observations of Alfvén waves rely on the apparent absence of intensity (i.e. density) perturbations in conjunction with torsional motion observed by alternating Doppler shifts, see for example (Jess et al., 2009). The results of Chapter 3 suggest that there exists at least one more alternative interpretation for waves with the aforementioned characteristics. Namely, the observed waves by Jess et al. (2009) could potentially be surface sausage waves (see right panel of Figure 3.4), since the localized character of the density perturbation also implies localized intensity perturbations that can be well below the instrument resolution. Furthermore, given the presence of torsional motion (see right panel of Figure 3.4) the sausage mode will have a Doppler signature similar to that of an Alfvén wave. The Doppler signature in combination with the fact that surface waves can have a phase velocity very close to the Alfvén speed (see SAW in Figure 3.6) suggests that Jess et al. (2009) potentially observed a sausage mode in the presence of magnetic twist. This line of reasoning is further supported by the evidence in Wedemeyer-Böhm et al. (2012) and Morton et al. (2013), where the authors show that vortical motions are ubiquitous in the photosphere. However, the excitation of the decoupled Alfvén wave requires vortical motion that is divergence free, see for example Ruderman et al. (1997), while the vortical motions observed in Morton et al. (2013) are not free of divergence. These vortical motions, and those investigated in Chapter 5, are a natural mechanism for the excitation of the axisymmetric modes studied in Chapter 3. A numerical study, based on the parameters identified in Chapter 5, to investigate the *sweetspot* of driver frequencies and the amount of propagated power in the higher layers of the atmosphere would be an excellent candidate for future research as it supply us with quantitative results for power propagation for this mode.

The fact that axisymmetric modes will be resonantly damped was known theoretically for quite some time, e.g. (see for example Goossens et al., 1992). However, perhaps due to the prevalence of the straight magnetic flux tube with constant mag-

netic field which predicted the sausage cutoff, no studies derived a dispersion relation for axisymmetric modes. Given that this cutoff is very sensitive, that is to say it is removed even for very weak twist (see Chapter 3), the study of axisymmetric modes in the presence of weak magnetic twist became most pertinent. In Chapter 4 a complex dispersion relation was derived for these modes in the spectrum of the Alfvén continuum. This relation along with the resulting approximation in the long wavelength limit, show that the damping time is proportional to the magnetic twist and inversely proportional to the density contrast.

Of the two solutions uncovered in Chapter 4, only the one with a phase velocity close the internal Alfvén speed has, for some parameter combinations, damping times that would allow observation. The other solution is found to be damped on time scales $\approx 10^{-2} - 10^{-1}$ of the wave period as seen in Figure 4.6, which means that its observation would be extremely challenging. On the other hand although the predicted damping times for the solution whose phase speed is close to the Alfvén speed are large enough to allow observation. Also, the fact that its phase speed is so close the internal Alfvén speed along with the dominance of the $\xi_\perp$ component in the wave dynamics means that the character of this wave will be predominantly Alfvénic (Goossens et al., 2011). Because of this, it is argued that it is possible that resonantly damped sausage waves have already been observed, albeit in the guise of Aflvén waves, see for example Jess et al. (2009).

Lastly, the damping time was estimated for the parameters presented by Morton et al. (2012) and Van Doorsselaere et al. (2011) and interestingly the predicted damping time is very close to the observed damping in quasi-periodic pulsations by Kolotkov et al. (2015) that are believed to be fast sausage waves. Subject to certain assumptions, axisymmetric modes appear to be quite important conduits for energy transfer in the solar atmosphere. Perhaps even more important than pure Alfvén waves, given that the excitation mechanism for sausage modes in weakly twisted magnetic flux tubes appears to be more readily available in comparison to the required purely torsional drivers for Alfvén waves, see (Giagkiozis et al., 2015) and Chapter 3.

Concluding Remarks

It is most interesting that an aleged quote by A. Einstein is pertinent to this day and especially to solar physics and observations: "As far as the laws of mathematics refer to reality, they are not certain; and as far as they are certain, they do not refer to reality." This, I find, to be a most accurate description and as I mention in 4.5, we ought to take an approach closer to the one illustrated most excellently by Arregui et al. (2015). That is, we should move towards a probabilistic or statistical approach in interpreting observations.

Appendix A

Axisymmetric Modes

A.1 Dimensionless Dispersion Equation

For completeness we give here the dimensionless version of the dispersion equation Equation (4.28). The following equation is now a function of v_F and $\mathcal{K}$, instead of ω and k_z. One of the benefits of solving Equation (A.1) instead of Equation (4.28) directly is that the former is, usually, numerically more stable. Another benefit is that the study of different plasma conditions is made simpler since it is straightforward to alter the ordering of the characteristic speeds (v_{si}, v_{Ai} etc).

$$\frac{\rho_e}{\rho_i}\frac{\mathcal{K}(v_F^2-v_{AE}^2)}{k_{rE}^2}\frac{K_{\nu-1}(k_{rE}\mathcal{K})}{K_\nu(k_{rE}\mathcal{K})} = \left[\frac{v_{A\Phi I}^2}{k_{rI}^2}(1+N_I)^2 - \frac{\rho_e}{\rho_i}\frac{v_{A\Phi E}^2}{k_{rE}^2}(1+N_E^2)\right] + \frac{\rho_e}{\rho_i}\frac{(1-\nu)(v_F^2-v_{AE}^2)}{M_E^2} - 2\frac{(v_F^2-1)}{k_{rI}^2}\frac{M(a,b-1;s)}{M(a,b;s)}, \tag{A.1}$$

where,

$$a = 1+\frac{k_{rI}^2\left[\mathcal{K}^2(v_F^2-1)^2-4v_{A\Phi I}^2\right]}{8v_{A\Phi I}^2N_I(v_F^2-1)}, \qquad b=2, \qquad s=2\frac{v_{A\Phi I}^2N_I}{(v_F^2-1)},$$

$$v_{ph}=\frac{\omega}{k_z}, \quad v_F=\frac{v_{ph}}{v_{Ai}}, \quad v_{SI}=\frac{v_{si}}{v_{Ai}}, \quad v_{SE}=\frac{v_{se}}{v_{Ai}}, \quad v_{AI}=1,$$
$$v_{AE}=\frac{v_{Ae}}{v_{Ai}}, \quad n_i^2=k_z^2N_I^2, \quad n_e^2=k_z^2N_E^2, \quad k_{ri}^2=k_z^2k_{rI}^2, \quad k_{re}^2=k_z^2k_{rE}^2$$
$$v_{TI}=\frac{v_{Ti}}{v_{Ai}}, \quad v_{TE}=\frac{v_{Te}}{v_{Ai}}, \quad \mathcal{K}=k_zr_a, \quad v_{A\Phi I}=\frac{v_{A\varphi i}}{v_{Ai}}, \quad v_{A\Phi E}=\frac{v_{A\varphi e}}{v_{Ai}},$$

and

$$N_I^2=\frac{v_F^4}{v_F^2+v_{SI}^2(v_F^2-1)}, \qquad N_E^2=\frac{v_F^4}{v_F^2v_{AE}^2+v_{SE}^2(v_F^2-1)},$$
$$k_{rI}^2=\frac{(v_{SI}^2-v_F^2)(1-v_F^2)}{(1+v_{SI}^2)(v_{TI}^2-v_F^2)}, \qquad k_{rE}^2=\frac{(v_{SE}^2-v_F^2)(v_{AE}^2-v_F^2)}{(v_{AE}^2+v_{SE}^2)(v_{TE}^2-v_F^2)},$$

$$v_{Ti}^2 = \frac{v_{Ai}^2 v_{si}^2}{v_{Ai}^2 + v_{si}^2}, \qquad v_{TI}^2 = \frac{v_{SI}^2}{1 + v_{SI}^2}, \qquad v_{Te}^2 = \frac{v_{Ae}^2 v_{se}^2}{v_{Ae}^2 + v_{se}^2}, \qquad v_{TE}^2 = \frac{v_{AE}^2 v_{SE}^2}{v_{AE}^2 + v_{SE}^2},$$

$$\nu^2 = 1 + 2\frac{v_{A\Phi E}^2}{(v_F^2 - v_{AE}^2)^2}\left[2v_{A\Phi I}^2 N_E^2 + (v_{AE}^2(3N_E^2 - 1) - v_F^2(N_E^2 + 1))\right].$$

Also the plasma-β inside and outside the flux-tube can be calculated using: $\beta_i = (2/\gamma)v_{SI}^2$ and $\beta_e = (2\rho_e B_{z_i}^2/\gamma\rho_i B_{z_e}^2)v_{SE}^2$ respectively.

A.2 Estimation of the Root Mean Square Error

We argue that the exact solution for constant twist outside the magnetic flux tube is a good approximation to the solution corresponding to the case where the twist is $\propto 1/r$. However, as we state in the text, we only obtain the zeroth-order term in the perturbation series which corresponds to constant twist. To justify this statement we estimate the root mean squared error (RMSE) also referred to as standard error, defined as follows,

$$RMSE = \lim_{L\to\infty}\left(\frac{1}{L-1}\int_{r_a}^{L}\left(\hat{\xi_{re}}(r) - \xi_{re}(r)\right)^2 dr\right)^{\frac{1}{2}}.$$

In this context, $\hat{\xi_{re}}(r)$ is the solution to the case with constant magnetic twist, i.e. $\kappa = 0$ in Equation (3.23), while $\xi_{re}(r)$ is a numerical solution to Equation (3.23) with $\kappa = 1$, namely magnetic twist proportional to $1/r$. The RMSE is expected to vary for different parameters, i.e. $\mathcal{K}, v_F$ and $B_{\varphi i}/B_{zi}$, and for this reason we discretize $\mathcal{K}$ and v_F using a 100×100 grid and also use the following value for $B_{\varphi i}/B_{zi} = 0.2$, since for all values of $B_{\varphi i}/B_{zi} < 0.2$ the RMSE is consistently smaller. Subsequently we average the resulting root mean square errors which we then quote in the corresponding figure caption. Note, that $\hat{\xi_{re}}(r)$ and $\xi_{re}(r)$ are normalized, therefore a value for the mean RMSE of, e.g. 0.01, means that the standard error is 1% on average, when comparing $\hat{\xi_{re}}(r)$ with $\xi_{re}(r)$.

A.3 Characteristic Speeds Ordering Considerations

The ordering of characteristic speeds depends on 6 variables: B_{zi}, B_{ze}, T_i, T_e, n_i, n_e, where n_i and n_e are the number densities inside and outside the flux tube respectively.

Starting from and assuming the magnetic twist is small,

$$v_{Ai} = \frac{B_{zi}}{\sqrt{\mu_0 \rho_i}}, \qquad v_{Ai} = \frac{B_{zi}}{\sqrt{\mu_0 \rho_i}}, \qquad v_{si} = \sqrt{\gamma \frac{p_i}{\rho_i}}, \qquad v_{se} = \sqrt{\gamma \frac{p_e}{\rho_e}},$$
$$\beta_i = \frac{2\mu_0 p_i}{B_{zi}^2}, \qquad \beta_e = \frac{2\mu_0 p_e}{B_{ze}^2}, \qquad \rho = n m_p, \qquad p = n k_B T.$$

Taking logs of the speeds and using the following definitions:

$$v_{Ai}^\star = \ln(v_{Ai}) + \frac{1}{2}\ln(\mu_0 m_p), \qquad v_{Ae}^\star = \ln(v_{Ae}) + \frac{1}{2}\ln(\mu_0 m_p),$$
$$v_{si}^\star = \ln(v_{si}) - \frac{1}{2}\ln\left(\gamma \frac{k_B}{m_p}\right), \qquad v_{se}^\star = \ln(v_{se}) - \frac{1}{2}\ln\left(\gamma \frac{k_B}{m_p}\right),$$
$$b_i^\star = \frac{1}{2}\left(\ln(\beta_i) - \ln(2k_B\mu_0)\right), \qquad b_e^\star = \frac{1}{2}\left(\ln(\beta_e) - \ln(2k_B\mu_0)\right),$$

and

$$B_{zi}^\star = \ln(B_{zi}), \qquad B_{ze}^\star = \ln(B_{ze}), \quad T_i^\star = (1/2)\ln(T_i), \quad T_e^\star = (1/2)\ln(T_e),$$
$$n_i^\star = (1/2)\ln(n_i), \quad n_e^\star = (1/2)\ln(n_e),$$

the speeds and plasma-β parameters can be written as follows,

$$\begin{pmatrix} 1 & 0 & 0 & 0 & -1 & 0 \\ 0 & 1 & 0 & 0 & 0 & -1 \\ 0 & 0 & 1 & 0 & 0 & 0 \\ 0 & 0 & 0 & 1 & 0 & 0 \\ -1 & 0 & 1 & 0 & 1 & 0 \\ 0 & -1 & 0 & 1 & 0 & 1 \end{pmatrix} \begin{pmatrix} B_{zi}^\star \\ B_{ze}^\star \\ T_i^\star \\ T_e^\star \\ n_i^\star \\ n_e^\star \end{pmatrix} = \begin{pmatrix} v_{Ai}^\star \\ v_{Ae}^\star \\ v_{si}^\star \\ v_{se}^\star \\ b_i^\star \\ b_e^\star \end{pmatrix}.$$

Now notice that the above matrix is rank 4 which means that the dimension of the null-space is 2, with basis vectors: $y_1 = (1, 0, 0, 0, 1, 0)$, and, $y_2 = (0, 1, 0, 0, 0, 1)$. This means in practice that for a given set of parameters resulting in a specific speed ordering β_i and β_e are uniquely defined but there is a 2 dimensional subspace involving $B_{zi}^\star$, $B_{ze}^\star$, $n_i^\star$, $n_e^\star$, that is, all linear combinations of y_1 and y_2. Also notice that the sound speeds, $v_{si}^\star$ and $v_{se}^\star$, depend only on the internal and external temperature, $T_i^\star$ and $T_e^\star$ respectively. Additionally the null-space of the matrix (see the basis vectors y_1 and y_2) suggests that the densities, $n_i^\star$ and $n_e^\star$, are secondary variables to the magnetic field strength, $B_{zi}^\star$ and $B_{ze}^\star$.

A.4 Perturbed quantities in terms of ξ_r and p'_T

Given, ξ_r and p'_T in Equation (4.17a),Equation (4.17b) or Equation (4.18a),Equation (4.18b) the remaining perturbed quantities for the sausage mode ($k_\varphi = 0$) are (Erdélyi and Fedun, 2010),

$$
\begin{aligned}
\xi_{ri}(s) &= A_{i1}\frac{s^{1/2}}{E^{1/4}}e^{-s/2}M(a,b;s)\,,\\
p'_{Ti}(s) &= A_{i1}\frac{k_a D_i}{n_i^2-k_z^2}e^{-s/2}\left[\frac{n_i+k_z}{k_z}sM(a,b;s)-2M(a,b-1;s)\right],\\
\xi_{re}(r) &= A_{e1}K_\nu\left(k_{re}r\right),\\
p'_{Te} &= A_{e1}\left(\frac{\mu_0(1-\nu)D_e-2r_a^2S_e^2n_e^2}{\mu_0 r(k_z^2-n_e^2)}K_\nu(k_{re}r)-\frac{D_e}{k_{re}}K_{\nu-1}(k_{re}r)\right),\\
\xi_\varphi &= \frac{ik_z}{\rho(\omega^2-\omega_A^2)}\frac{B_zB_\varphi}{\mu_0\rho}\left[\frac{n^2}{\omega^2}\left(\frac{2B_\varphi^2}{\mu_0 r}\xi_r-p'_T\right)-2\frac{\rho}{r}\xi_r\right],\\
\xi_z &= \frac{ik_z}{\rho\omega^2(\omega^2-\omega_A^2)}\left[(\omega^2-n^2v_A^2)p'_T+2\frac{B_\varphi^2}{\mu_0 r}v_A^2n^2\xi_r\right],\\
B'_r &= ik_zB_z\xi_r,\\
B'_\varphi &= \frac{k_z^2B_\varphi}{D}\left(p'_T+2\frac{B_z^2}{\mu_0 r}\xi_r\right)-\frac{d}{dr}(B_\varphi\xi_r),\\
B'_z &= -\frac{1}{r}\frac{d}{dr}(rB_z\xi_r).
\end{aligned}
$$

References

Milton Abramowitz and Irene A Stegun. *Handbook of mathematical functions: with formulas, graphs, and mathematical tables*. Courier Dover Publications, New York, 2012.

Hannes Alfvén. Existence of electromagnetic-hydrodynamic waves. *Nature*, 150(3805): 405–406, 1942.

T. Amari, J.-F. Luciani, and J.-J. Aly. Small-scale dynamo magnetism as the driver for heating the solar atmosphere. Nature, 522:188–191, June 2015. doi: 10.1038/nature14478.

J. Andries, M. Goossens, J. V. Hollweg, I. Arregui, and T. Van Doorsselaere. Coronal loop oscillations. calculation of resonantly damped mhd quasi-mode kink oscillations of longitudinally stratified loops. A&A, 430:1109–1118, feb 2005. doi: 10.1051/0004-6361:20041832.

P. Antolin, T. J. Okamoto, B. De Pontieu, H. Uitenbroek, T. Van Doorsselaere, and T. Yokoyama. Resonant Absorption of Transverse Oscillations and Associated Heating in a Solar Prominence. II. Numerical Aspects. ApJ, 809:72, August 2015. doi: 10.1088/0004-637X/809/1/72.

I. Arregui. Wave heating of the solar atmosphere. *Philosophical Transactions of the Royal Society of London Series A*, 373:40261, April 2015. doi: 10.1098/rsta.2014.0261.

I. Arregui and R. Soler. Model comparison for the density structure along solar prominence threads. A&A, 578:A130, June 2015. doi: 10.1051/0004-6361/201525720.

I. Arregui, R. Oliver, and J. L. Ballester. Prominence Oscillations. *Living Reviews in Solar Physics*, 9:2, April 2012. doi: 10.12942/lrsp-2012-2.

I. Arregui, R. Soler, and A. Asensio Ramos. Model Comparison for the Density Structure across Solar Coronal Waveguides. ApJ, 811:104, October 2015. doi: 10.1088/0004-637X/811/2/104.

M. J. Aschwanden, L. Fletcher, C. J. Schrijver, and D. Alexander. Coronal Loop Oscillations Observed with the Transition Region and Coronal Explorer. ApJ, 520: 880–894, August 1999. doi: 10.1086/307502.

M. J. Aschwanden, R. W. Nightingale, J. Andries, M. Goossens, and T. Van Doorsselaere. Observational Tests of Damping by Resonant Absorption in Coronal Loop Oscillations. ApJ, 598:1375–1386, December 2003. doi: 10.1086/379104.

Markus J Aschwanden. *Physics of the Solar Corona: An Introduction with Problems and Solutions*. Springer, 2005.

Carl M Bender and Steven A Orszag. *Advanced mathematical methods for scientists and engineers I: Asymptotic methods and perturbation theory*, volume 1. Springer, New York, 1999.

K. Bennett, B. Roberts, and U. Narain. Waves in twisted magnetic flux tubes. *solphys*, 185:41–59, mar 1999. doi: 10.1023/A:1005141432432.

T. Berger and ATST Science Team. The ATST Instrumentation suite: capabilities, synergies, and science goals. In *AAS/Solar Physics Division Meeting*, volume 44 of *AAS/Solar Physics Division Meeting*, page 400.02, July 2013.

T. J. Bogdan, M. Carlsson, V. H. Hansteen, A. McMurry, C. S. Rosenthal, M. Johnson, S. Petty-Powell, E. J. Zita, R. F. Stein, S. W. McIntosh, and Å. Nordlund. Waves in the magnetized solar atmosphere. ii. waves from localized sources in magnetic flux concentrations. *apj*, 599:626–660, dec 2003. doi: 10.1086/378512.

J. A. Bonet, I. Márquez, J. Sánchez Almeida, I. Cabello, and V. Domingo. Convectively Driven Vortex Flows in the Sun. ApJ, 687:L131–L134, November 2008. doi: 10.1086/593329.

J. A. Bonet, I. Márquez, J. Sánchez Almeida, J. Palacios, V. Martínez Pillet, S. K. Solanki, J. C. del Toro Iniesta, V. Domingo, T. Berkefeld, W. Schmidt, A. Gandorfer, P. Barthol, and M. Knölker. SUNRISE/IMaX Observations of Convectively Driven Vortex Flows in the Sun. ApJ, 723:L139–L143, November 2010. doi: 10.1088/2041-8205/723/2/L139.

D. S. Brown, R. W. Nightingale, D. Alexander, C. J. Schrijver, T. R. Metcalf, R. A. Shine, A. M. Title, and C. J. Wolfson. Observations of rotating sunspots from trace. *solphys*, 216:79–108, sep 2003. doi: 10.1023/A:1026138413791.

A. De Groof and M. Goossens. Randomly driven fast waves in coronal loops. II. with coupling to Alfvén waves. A&A, 356:724–734, April 2000.

A. De Groof and M. Goossens. Fast and Alfvén waves driven by azimuthal footpoint motions. II. Random driver. A&A, 386:691–698, May 2002. doi: 10.1051/0004-6361:20020204.

A. De Groof, K. Paes, and M. Goossens. Fast and Alfvén waves driven by azimuthal footpoint motions. I. Periodic driver. A&A, 386:681–690, May 2002. doi: 10.1051/0004-6361:20020203.

J. de la Cruz Rodríguez, M. G. Löfdahl, P. Sütterlin, T. Hillberg, and L. Rouppe van der Voort. CRISPRED: A data pipeline for the CRISP imaging spectropolarimeter. A&A, 573:A40, January 2015. doi: 10.1051/0004-6361/201424319.

I. De Moortel and V. M. Nakariakov. Magnetohydrodynamic waves and coronal seismology: an overview of recent results. *Philosophical Transactions of the Royal Society of London Series A*, 370:3193–3216, July 2012. doi: 10.1098/rsta.2011.0640.

B. De Pontieu, S. McIntosh, V. H. Hansteen, M. Carlsson, C. J. Schrijver, T. D. Tarbell, A. M. Title, R. A. Shine, Y. Suematsu, S. Tsuneta, Y. Katsukawa, K. Ichimoto, T. Shimizu, and S. Nagata. A tale of two spicules: The impact of spicules on the magnetic chromosphere. *pasj*, 59:655, nov 2007. doi: 10.1093/pasj/59.sp3.S655.

B. De Pontieu, M. Carlsson, L. H. M. Rouppe van der Voort, R. J. Rutten, V. H. Hansteen, and H. Watanabe. Ubiquitous torsional motions in type ii spicules. *apjl*, 752:L12, jun 2012. doi: 10.1088/2041-8205/752/1/L12.

P. M. Edwin and B. Roberts. Wave propagation in a magnetic cylinder. *solphys*, 88:179–191, oct 1983. doi: 10.1007/BF00196186.

R. Erdélyi and V. Fedun. Sausage mhd waves in incompressible flux tubes with twisted magnetic fields. *solphys*, 238:41–59, oct 2006. doi: 10.1007/s11207-006-0217-z.

R. Erdélyi and V. Fedun. Linear mhd sausage waves in compressible magnetically twisted flux tubes.
solphys, 246:101–118, nov 2007. doi: 10.1007/s11207-007-9022-6.

R. Erdélyi and V. Fedun. Magneto-acoustic waves in compressible magnetically twisted flux tubes.
solphys, 263:63–85, may 2010. doi: 10.1007/s11207-010-9534-3.

R. Erdélyi and R. J. Morton. Magnetohydrodynamic waves in a compressible magnetic flux tube with elliptical cross-section. A&A, 494:295–309, jan 2009. doi: 10.1051/0004-6361:200810318.

V. Fedun, S. Shelyag, G. Verth, M. Mathioudakis, and R. Erdélyi. MHD waves generated by high-frequency photospheric vortex motions. *Annales Geophysicae*, 29: 1029–1035, June 2011. doi: 10.5194/angeo-29-1029-2011.

George H Fisher and Brian T Welsch. Flct: A fast, efficient method for performing local correlation tracking. In *Subsurface and Atmospheric Influences on Solar Activity*, volume 383, page 373, 2008.

G. A. Gary. Plasma beta above a solar active region: Rethinking the paradigm.
solphys, 203:71–86, oct 2001. doi: 10.1023/A:1012722021820.

C. L. Gerrard, T. D. Arber, and A. W. Hood. The triggering of mhd instabilities through photospheric footpoint motions. A&A, 387(2):687–699, may 2002. doi: 10.1051/0004-6361:20020491.

I. Giagkiozis, V. Fedun, R. Erdelyi, and G. Verth. Axisymmetric modes in magnetic flux tubes with internal and external magnetic twist. ApJ, 810(1):53, sep 2015. doi: 10.1088/0004-637X/810/1/53.

I Giagkiozis, M Goossens, G Verth, V Fedun, and T Van Doorsselaere. Resonant absorption of axisymmetric modes in twisted magnetic flux tubes. *Astrophysical Journal*, 823(2):71, 2016. doi: 10.3847/0004-637X/823/2/71.

Johan Peter Goedbloed and Stefaan Poedts. *Principles of magnetohydrodynamics: With applications to laboratory and astrophysical plasmas*. Cambridge university press, 2004.

JP Goedbloed. Stabilization of magnetohydrodynamic instabilities by force-free magnetic fields: Ii. linear pinch. *Physica*, 53(4):501–534, 1971.

M. Goossens and S. Poedts. Linear resistive magnetohydrodynamic computations of resonant absorption of acoustic oscillations in sunspots. ApJ, 384:348–360, January 1992. doi: 10.1086/170878.

M. Goossens, J. V. Hollweg, and T. Sakurai. Resonant behaviour of mhd waves on magnetic flux tubes. iii - effect of equilibrium flow.
solphys, 138:233–255, apr 1992. doi: 10.1007/BF00151914.

M. Goossens, J. Andries, and M. J. Aschwanden. Coronal loop oscillations. an interpretation in terms of resonant absorption of quasi-mode kink oscillations. A&A, 394: L39–L42, nov 2002. doi: 10.1051/0004-6361:20021378.

M. Goossens, J. Terradas, J. Andries, I. Arregui, and J. L. Ballester. On the nature of kink MHD waves in magnetic flux tubes. A&A, 503:213–223, August 2009. doi: 10.1051/0004-6361/200912399.

M. Goossens, R. Erdélyi, and M. S. Ruderman. Resonant mhd waves in the solar atmosphere. Space Sci. Rev., 158:289–338, jul 2011. doi: 10.1007/s11214-010-9702-7.

L. Graftieaux, M. Michard, and N. Grosjean. Combining PIV, POD and vortex identification algorithms for the study of unsteady turbulent swirling flows. *Measurement Science and Technology*, 12(9):1422–1429, September 2001. doi: 10.1088/0957-0233/12/9/307.

S. D. T. Grant, D. B. Jess, M. G. Moreels, R. J. Morton, D. J. Christian, I. Giagkiozis, G. Verth, V. Fedun, P. H. Keys, T. Van Doorsselaere, and R. Erdélyi. Wave Damping Observed in Upwardly Propagating Sausage-mode Oscillations Contained within a Magnetic Pore. ApJ, 806:132, June 2015. doi: 10.1088/0004-637X/806/1/132.

Hermance J Hagenaar, Carolus J Schrijver, et al. The distribution of cell sizes of the solar chromospheric network. *The Astrophysical Journal*, 481(2):988, 1997.

K Hain and RZ Lust. Normal mode equations of cylindrical plasma. *Naturforsch*, 13: 936, 1958.

V. Hansteen, B. De Pontieu, M. Carlsson, J. Lemen, A. Title, P. Boerner, N. Hurlburt, T. D. Tarbell, J. P. Wuelser, T. M. D. Pereira, E. E. De Luca, L. Golub, S. McKillop, K. Reeves, S. Saar, P. Testa, H. Tian, C. Kankelborg, S. Jaeggli, L. Kleint, and J. Martínez-Sykora. The unresolved fine structure resolved: IRIS observations of the solar transition region. *Science*, 346:1255757, October 2014. doi: 10.1126/science.1255757.

VH Hansteen, M Carlsson, A Fossum, E Marthinussen, MJ van Noort, and TE Berger. Solar magnetic elements at 0 resolution-ii. dynamical evolution. *Astronomy & Astrophysics*, 435(1):327–337, 2005.

J. V. Hollweg. Resonance absorption of solar p-modes by sunspots. ApJ, 335:1005–1014, December 1988. doi: 10.1086/166987.

J. V. Hollweg and G. Yang. Resonance absorption of compressible magnetohydrodynamic waves at thin 'surfaces'. J. Geophys. Res., 93:5423–5436, June 1988. doi: 10.1029/JA093iA06p05423.

A. W. Hood, V. Archontis, K. Galsgaard, and F. Moreno-Insertis. The emergence of toroidal flux tubes from beneath the solar photosphere. A&A, 503:999–1011, sep 2009. doi: 10.1051/0004-6361/200912189.

J. A. Ionson. Resonant absorption of Alfvenic surface waves and the heating of solar coronal loops. ApJ, 226:650–673, December 1978. doi: 10.1086/156648.

J. A. Ionson. Coronal heating by resonant (A.C.) and nonresonant (D.C.) mechanisms. A&A, 146:199–203, May 1985.

John David Jackson. *Classical Electrodynamics*. AAPT, 1999.

D. B. Jess, M. Mathioudakis, R. Erdélyi, P. J. Crockett, F. P. Keenan, and D. J. Christian. Alfvén waves in the lower solar atmosphere. *Science*, 323:1582–, mar 2009. doi: 10.1126/science.1168680.

D. B. Jess, R. J. Morton, G. Verth, V. Fedun, S. D. T. Grant, and I. Giagkiozis. Multiwavelength Studies of MHD Waves in the Solar Chromosphere - An Overview of Recent Results. Space Sci. Rev., March 2015. doi: 10.1007/s11214-015-0141-3.

BB Kadomtsev. Hydromagnetic stability of a plasma. *Reviews of Plasma Physics*, 2: 153–199, 1966.

K. Karami and K. Bahari. The effect of twisted magnetic field on the resonant absorption of mhd waves in coronal loops.
solphys, 263:87–103, may 2010. doi: 10.1007/s11207-010-9537-0.

Maria D Kazachenko, Richard C Canfield, Dana W Longcope, Jiong Qiu, Angela DesJardins, and Richard W Nightingale. Sunspot rotation, flare energetics, and flux rope helicity: the eruptive flare on 2005 may 13. *The Astrophysical Journal*, 704(2): 1146, 2009.

R. Keppens, T. J. Bogdan, and M. Goossens. Multiple scattering and resonant absorption of p-modes by fibril sunspots. ApJ, 436:372–389, November 1994. doi: 10.1086/174912.

I. N. Kitiashvili, A. G. Kosovichev, N. N. Mansour, S. K. Lele, and A. A. Wray. Vortex tubes of turbulent solar convection. Phys. Scr, 86(1):018403, July 2012a. doi: 10.1088/0031-8949/86/01/018403.

I. N. Kitiashvili, A. G. Kosovichev, N. N. Mansour, and A. A. Wray. Dynamics of Magnetized Vortex Tubes in the Solar Chromosphere. ApJ, 751:L21, May 2012b. doi: 10.1088/2041-8205/751/1/L21.

J. A. Klimchuk. Key aspects of coronal heating. *Philosophical Transactions of the Royal Society of London Series A*, 373:20140256–20140256, April 2015. doi: 10.1098/rsta.2014.0256.

D. Y. Kolotkov, V. M. Nakariakov, E. G. Kupriyanova, H. Ratcliffe, and K. Shibasaki. Multi-mode quasi-periodic pulsations in a solar flare. A&A, 574:A53, February 2015. doi: 10.1051/0004-6361/201424988.

M. D. Kruskal, J. L. Johnson, M. B. Gottlieb, and L. M. Goldman. Hydromagnetic instability in a stellarator. *Physics of Fluids*, 1:421–429, sep 1958. doi: 10.1063/1.1724359.

J. R. Lemen, A. M. Title, D. J. Akin, P. F. Boerner, C. Chou, J. F. Drake, D. W. Duncan, C. G. Edwards, F. M. Friedlaender, G. F. Heyman, N. E. Hurlburt, N. L. Katz, G. D. Kushner, M. Levay, R. W. Lindgren, D. P. Mathur, E. L. McFeaters, S. Mitchell, R. A. Rehse, C. J. Schrijver, L. A. Springer, R. A. Stern, T. D. Tarbell, J.-P. Wuelser, C. J. Wolfson, C. Yanari, J. A. Bookbinder, P. N. Cheimets, D. Caldwell, E. E. Deluca, R. Gates, L. Golub, S. Park, W. A. Podgorski, R. I. Bush, P. H. Scherrer, M. A. Gummin, P. Smith, G. Auker, P. Jerram, P. Pool, R. Soufli, D. L. Windt, S. Beardsley, M. Clapp, J. Lang, and N. Waltham. The Atmospheric Imaging Assembly (AIA) on the Solar Dynamics Observatory (SDO). Sol. Phys., 275:17–40, January 2012. doi: 10.1007/s11207-011-9776-8.

R. E. Louis, B. Ravindra, M. K. Georgoulis, and M. Küker. Analysing the Effects of Apodizing Windows on Local Correlation Tracking Using Nirvana Simulations of Convection. Sol. Phys., 290:1135–1146, April 2015. doi: 10.1007/s11207-015-0659-2.

M. L. Luoni, P. Démoulin, C. H. Mandrini, and L. van Driel-Gesztelyi. Twisted flux tube emergence evidenced in longitudinal magnetograms: Magnetic tongues. *solphys*, 270:45–74, may 2011. doi: 10.1007/s11207-011-9731-8.

S. W. McIntosh, B. de Pontieu, M. Carlsson, V. Hansteen, P. Boerner, and M. Goossens. Alfvénic waves with sufficient energy to power the quiet solar corona and fast solar wind. Nature, 475:477–480, July 2011. doi: 10.1038/nature10235.

R. J. Morton, G. Verth, D. B. Jess, D. Kuridze, M. S. Ruderman, M. Mathioudakis, and R. Erdélyi. Observations of ubiquitous compressive waves in the sun's chromosphere. *Nature Communications*, 3:1315, dec 2012. doi: 10.1038/ncomms2324.

R. J. Morton, G. Verth, V. Fedun, S. Shelyag, and R. Erdélyi. Evidence for the photospheric excitation of incompressible chromospheric waves. *apj*, 768:17, may 2013. doi: 10.1088/0004-637X/768/1/17.

M. J. Murray and A. W. Hood. Emerging flux tubes from the solar interior into the atmosphere: effects of non-constant twist. A&A, 479:567–577, feb 2008. doi: 10.1051/0004-6361:20078852.

V. Nakariakov. Slow magnetoacoustic waves in the solar corona. In *39th COSPAR Scientific Assembly*, volume 39 of *COSPAR Meeting*, page 1330, July 2012.

V. M. Nakariakov and I. V. Zimovets. Slow Magnetoacoustic Waves in Two-ribbon Flares. ApJ, 730:L27, April 2011. doi: 10.1088/2041-8205/730/2/L27.

V. M. Nakariakov, L. Ofman, E. E. Deluca, B. Roberts, and J. M. Davila. TRACE observation of damped coronal loop oscillations: Implications for coronal heating. *Science*, 285(5429):862–864, August 1999. doi: 10.1126/science.285.5429.862.

Å. Nordlund, R. F. Stein, and M. Asplund. Solar Surface Convection. *Living Reviews in Solar Physics*, 6, April 2009. doi: 10.12942/lrsp-2009-2.

L. J. November and G. W. Simon. Precise proper-motion measurement of solar granulation. ApJ, 333:427–442, October 1988. doi: 10.1086/166758.

T. J. Okamoto, P. Antolin, B. De Pontieu, H. Uitenbroek, T. Van Doorsselaere, and T. Yokoyama. Resonant Absorption of Transverse Oscillations and Associated Heating in a Solar Prominence. I. Observational Aspects. ApJ, 809:71, August 2015. doi: 10.1088/0004-637X/809/1/71.

J. Palacios, L. A. Balmaceda, S. V. Domínguez, I. Cabello, and V. Domingo. Observations of Vortex Motion in the Solar Photosphere Using Hinode-SP Data. In T. Sekii, T. Watanabe, and T. Sakurai, editors, *Hinode-3: The 3rd Hinode Science Meeting*, volume 454 of *Astronomical Society of the Pacific Conference Series*, page 51, August 2012.

S.-H. Park, G. Tsiropoula, I. Kontogiannis, K. Tziotziou, E. Scullion, and J. G. Doyle. First simultaneous SST/CRISP and IRIS observations of a small-scale quiet Sun vortex. A&A, 586:A25, February 2016. doi: 10.1051/0004-6361/201527440.

E. N. Parker. Topological Dissipation and the Small-Scale Fields in Turbulent Gases. ApJ, 174:499, June 1972. doi: 10.1086/151512.

E. N. Parker. Magnetic neutral sheets in evolving fields. I - General theory. ApJ, 264: 635–647, January 1983a. doi: 10.1086/160636.

E. N. Parker. Magnetic Neutral Sheets in Evolving Fields - Part Two - Formation of the Solar Corona. ApJ, 264:642, January 1983b. doi: 10.1086/160637.

Stephen M Pizer, E Philip Amburn, John D Austin, Robert Cromartie, Ari Geselowitz, Trey Greer, Bart ter Haar Romeny, John B Zimmerman, and Karel Zuiderveld. Adaptive histogram equalization and its variations. *Computer vision, graphics, and image processing*, 39(3):355–368, 1987.

S. Poedts, M. Goossens, and W. Kerner. Numerical simulation of coronal heating by resonant absorption of Alfven waves. Sol. Phys., 123:83–115, March 1989. doi: 10.1007/BF00150014.

S. Poedts, M. Goossens, and W. Kerner. On the efficiency of coronal loop heating by resonant absorption. ApJ, 360:279–287, September 1990. doi: 10.1086/169118.

Eric Priest. *Magnetohydrodynamics of the Sun*. Cambridge University Press, 2014.

Th Roudier and R Muller. Structure of the solar granulation. *Solar Physics*, 107(1): 11–26, 1986.

M. S. Ruderman. The resonant damping of oscillations of coronal loops with elliptic cross-sections. A&A, 409:287–297, oct 2003. doi: 10.1051/0004-6361:20031079.

M. S. Ruderman and R. Erdélyi. Transverse oscillations of coronal loops. Space Sci. Rev., 149:199–228, dec 2009. doi: 10.1007/s11214-009-9535-4.

M. S. Ruderman and B. Roberts. The damping of coronal loop oscillations. *apj*, 577:475–486, sep 2002. doi: 10.1086/342130.

M. S. Ruderman, D. Berghmans, M. Goossens, and S. Poedts. Direct excitation of resonant torsional alfven waves by footpoint motions. A&A, 320:305–318, apr 1997.

T. Sakurai, M. Goossens, and J. V. Hollweg. Resonant behaviour of MHD waves on magnetic flux tubes. I - Connection formulae at the resonant surfaces. Sol. Phys., 133:227–245, June 1991a. doi: 10.1007/BF00149888.

T. Sakurai, M. Goossens, and J. V. Hollweg. Resonant Behaviour of Magnetohydrodynamic Waves on Magnetic Flux Tubes II. Absorption of Sound Waves by Sunspots. Sol. Phys., 133:247–262, June 1991b. doi: 10.1007/BF00149889.

G. B. Scharmer, K. Bjelksjo, T. K. Korhonen, B. Lindberg, and B. Petterson. The 1-meter Swedish solar telescope. In S. L. Keil and S. V. Avakyan, editors, *Innovative Telescopes and Instrumentation for Solar Astrophysics*, volume 4853 of Proc. SPIE, pages 341–350, February 2003.

G. B. Scharmer, G. Narayan, T. Hillberg, J. de la Cruz Rodriguez, M. G. Löfdahl, D. Kiselman, P. Sütterlin, M. van Noort, and A. Lagg. Crisp spectropolarimetric imaging of penumbral fine structure. ApJ, 689:L69, dec 2008. doi: 10.1086/595744.

D. H. Sekse, L. Rouppe van der Voort, B. De Pontieu, and E. Scullion. Interplay of three kinds of motion in the disk counterpart of type ii spicules: Upflow, transversal, and torsional motions. ApJ, 769:44, may 2013. doi: 10.1088/0004-637X/769/1/44.

V.D. Shafranov. On the stability of a cylindrical gaseous conductor in a magnetic field. *Journal of Nuclear Energy*, 5(1):86–91, 1957. doi: http://dx.doi.org/10.1016/0891-3919(57)90015-3.

S. Shelyag, P. Keys, M. Mathioudakis, and F. P. Keenan. Vorticity in the solar photosphere. A&A, 526:A5, February 2011. doi: 10.1051/0004-6361/201015645.

S. Shelyag, V. Fedun, R. Erdélyi, F. P. Keenan, and M. Mathioudakis. Vortices in the Solar Photosphere. In T. R. Rimmele, A. Tritschler, F. Wöger, M. Collados Vera, H. Socas-Navarro, R. Schlichenmaier, M. Carlsson, T. Berger, A. Cadavid, P. R. Gilbert, P. R. Goode, and M. Knölker, editors, *Second ATST-EAST Meeting: Magnetic Fields from the Photosphere to the Corona.*, volume 463 of *Astronomical Society of the Pacific Conference Series*, page 107, December 2012.

S. Shelyag, P. S. Cally, A. Reid, and M. Mathioudakis. Alfvén Waves in Simulations of Solar Photospheric Vortices. ApJ, 776:L4, October 2013. doi: 10.1088/2041-8205/776/1/L4.

RA Shine, GW Simon, and NE Hurlburt. Supergranule and mesogranule evolution. *Solar Physics*, 193(1):313–331, 2000.

H. C. Spruit. Propagation speeds and acoustic damping of waves in magnetic flux tubes. Sol. Phys., 75(1-2):3–17, January 1982. doi: 10.1007/BF00153456.

O. Steiner, M. Franz, N. Bello González, C. Nutto, R. Rezaei, V. Martínez Pillet, J. A. Bonet Navarro, J. C. del Toro Iniesta, V. Domingo, S. K. Solanki, M. Knölker, W. Schmidt, P. Barthol, and A. Gandorfer. Detection of Vortex Tubes in Solar Granulation from Observations with SUNRISE. ApJ, 723:L180–L184, November 2010. doi: 10.1088/2041-8205/723/2/L180.

Michael Stix. *The Sun: an introduction*. Springer Science & Business Media, 2012.

J. Terradas. Excitation of Standing Kink Oscillations in Coronal Loops. Space Sci. Rev., 149:255–282, December 2009. doi: 10.1007/s11214-009-9560-3.

J. Terradas and M. Goossens. Transverse kink oscillations in the presence of twist. A&A, 548:A112, dec 2012. doi: 10.1051/0004-6361/201219934.

J. Terradas, I. Arregui, R. Oliver, and J. L. Ballester. Transverse Oscillations of Flowing Prominence Threads Observed with Hinode. ApJ, 678:L153–L156, May 2008. doi: 10.1086/588728.

J. Terradas, M. Goossens, and G. Verth. Selective spatial damping of propagating kink waves due to resonant absorption. A&A, 524:A23, December 2010. doi: 10.1051/0004-6361/201014845.

W. J. Tirry and M. Goossens. Quasi-modes as dissipative magnetohydrodynamic eigenmodes: Results for one-dimensional equilibrium states.
apj, 471:501, nov 1996. doi: 10.1086/177986.

T. Török, B. Kliem, and V. S. Titov. Ideal kink instability of a magnetic loop equilibrium. A&A, 413:L27–L30, jan 2004. doi: 10.1051/0004-6361:20031691.

R. Trampedach, R. F. Stein, J. Christensen-Dalsgaard, Å. Nordlund, and M. Asplund. Improvements to stellar structure models, based on a grid of 3d convection simulations - ii. calibrating the mixing-length formulation.
mnras, 445:4366–4384, dec 2014. doi: 10.1093/mnras/stu2084.

T. Van Doorsselaere, A. Debosscher, J. Andries, and S. Poedts. The effect of curvature on quasi-modes in coronal loops. 575:448, dec 2004.

T. Van Doorsselaere, E. Verwichte, and J. Terradas. The effect of loop curvature on coronal loop kink oscillations. Space Sci. Rev., 149:299–324, dec 2009. doi: 10.1007/s11214-009-9530-9.

T. Van Doorsselaere, A. De Groof, J. Zender, D. Berghmans, and M. Goossens. LYRA Observations of Two Oscillation Modes in a Single Flare. ApJ, 740:90, October 2011. doi: 10.1088/0004-637X/740/2/90.

M. van Noort, L. Rouppe van der Voort, and M. G. Löfdahl. Solar Image Restoration By Use Of Multi-frame Blind De-convolution With Multiple Objects And Phase Diversity. Sol. Phys., 228:191–215, May 2005. doi: 10.1007/s11207-005-5782-z.

M. J. van Noort and L. H. M. Rouppe van der Voort. Stokes imaging polarimetry using image restoration at the Swedish 1-m solar telescope. A&A, 489:429–440, October 2008. doi: 10.1051/0004-6361:200809959.

S. Vargas Domínguez, J. Palacios, L. Balmaceda, I. Cabello, and V. Domingo. Spatial distribution and statistical properties of small-scale convective vortex-like motions in a quiet-Sun region. MNRAS, 416:148–154, September 2011. doi: 10.1111/j.1365-2966.2011.19048.x.

S. Vasheghani Farahani, C. Hornsey, T. Van Doorsselaere, and M. Goossens. Frequency and Damping Rate of Fast Sausage Waves. ApJ, 781:92, February 2014. doi: 10.1088/0004-637X/781/2/92.

M. Verma, M. Steffen, and C. Denker. Evaluating local correlation tracking using CO5BOLD simulations of solar granulation. A&A, 555:A136, July 2013. doi: 10.1051/0004-6361/201321628.

J. E. Vernazza, E. H. Avrett, and R. Loeser. Structure of the solar chromosphere. iii - models of the euv brightness components of the quiet-sun.
apjs, 45:635–725, apr 1981. doi: 10.1086/190731.

Gary Verth, J Terradas, and M Goossens. Observational evidence of resonantly damped propagating kink waves in the solar corona. *The Astrophysical Journal Letters*, 718 (2):L102, 2010.

E. Verwichte, T. Van Doorsselaere, R. S. White, and P. Antolin. Statistical seismology of transverse waves in the solar corona. A&A, 552:A138, April 2013. doi: 10.1051/0004-6361/201220456.

G. Vigeesh, V. Fedun, S. S. Hasan, and R. Erdélyi. Three-dimensional simulations of magnetohydrodynamic waves in magnetized solar atmosphere. *apj*, 755:18, aug 2012. doi: 10.1088/0004-637X/755/1/18.

S. Wedemeyer, E. Scullion, L. Rouppe van der Voort, A. Bosnjak, and P. Antolin. Are Giant Tornadoes the Legs of Solar Prominences? ApJ, 774:123, September 2013. doi: 10.1088/0004-637X/774/2/123.

Sven Wedemeyer-Böhm, Eamon Scullion, Oskar Steiner, Luc Rouppe van der Voort, Jaime de La Cruz Rodriguez, Viktor Fedun, and Robert Erdélyi. Magnetic tornadoes as energy channels into the solar corona. *Nature*, 486(7404):505–508, 2012.

Thomas Williams and Youra Taroyan. Formation of a dense flux rope by a siphon flow. *The Astrophysical Journal*, 852(2):77, 2018.

G. L. Withbroe and R. W. Noyes. Mass and energy flow in the solar chromosphere and corona. ARA&A, 15:363–387, 1977. doi: 10.1146/annurev.aa.15.090177.002051.

X. L. Yan and Z. Q. Qu. Rapid rotation of a sunspot associated with flares. A&A, 468: 1083–1088, jun 2007. doi: 10.1051/0004-6361:20077064.